ABSTRACT

PION INELASTIC SCATTERING
AND THE
PION-NUCLEUS EFFECTIVE INTERACTION

By

James Arthur Carr

This work examines pion inelastic scattering with the primary purpose of gaining a better understanding of the properties of the pion-nucleus interaction. The main conclusion of the work is that an effective interaction which incorporates the most obvious theoretical corrections to the impulse approximation does a good job of explaining pion elastic and inelastic scattering from zero to 200 MeV without significant adjustments to the strength parameters of the force.

Watson's multiple scattering theory is used to develop a theoretical interaction starting from the free pion-nucleon interaction. Elastic scattering was used to calibrate the isoscalar central interaction. It was found that the impulse approximation did poorly at low energy, while the multiple scattering corrections gave good agreement with all of the data after a few minor adjustments in the force.

The distorted wave approximation for the inelastic transition matrix elements are evaluated for both natural and unnatural parity excitations. The isoscalar natural parity transitions are used to test the reaction theory, and it is found that the effective interaction calibrated by elastic scattering produces good agreement with the inelastic data. Thus the medium corrections required to obtain the correct optical potential are just as important when calculating

inelastic cross sections. It is also noted that low energy inelastic scattering is much more sensitive to the choice of the distorting potential than is inelastic scattering in the resonance region.

Calculations are also shown for other inelastic and charge exchange reactions. It appears that the isovector central interaction is reasonable, but the importance of medium corrections cannot be determined. The unnatural parity transitions are also reasonably described by the theoretical estimate of the spin-orbit interaction, but not enough systematic data exists to reach a firm conclusion.

In summary, it is seen that a consistent explanation of pion inelastic scattering is possible. In some cases more complete experimental information is needed to properly test the theory. Other areas where more theoretical work is needed have also been identified.

PION INELASTIC SCATTERING

AND THE

PION-NUCLEUS EFFECTIVE INTERACTION

By

James Arthur Carr

A DISSERTATION

Submitted to
Michigan State University
in partial fulfillment of the requirements
for the degree of

DOCTOR OF PHILOSOPHY

Department of Physics

1981

ACKNOWLEDGMENTS

I would like to thank Prof. Hugh McManus for suggesting this problem, and for his patience and guidance throughout my graduate career. Our many discussions did much to develop my physical intuition and I shall always treasure the opportunity I had to work with him.

Thanks is also due to Dr. Karen Stricker, whose work on elastic scattering was an indispensible prerequisite to this project, Prof. Dan Olaf Riska for many useful discussions, and Prof. Fred Petrovich for invaluable insights and a very productive collaboration in the last year of this work. I would also like to thank the Cyclotron faculty, computer staff and Nuclear Beer Group for providing a stimulating work environment, and many experimental groups for supplying their data in advance of publication.

Finally, special thanks to some people who mean a great deal to me. Joe Finck and I spent many years studying, teaching physics and partying together -- those years were some of the best of my life. (They were certainly unforgettable.) My parents and grandparents have always supported and encouraged me -- I cannot thank them enough. Kathleen McGleish, now my wife, gave me her unwavering love and helped me through the long trying days and years it took to finish this. She has made my life full and complete. Words cannot express my gratitude. Last but not least, a big thank you to my mother-in-law, Kelley, for the considerable effort involved in typing all of these equations!

TABLE OF CONTENTS

LIST OF FIGURES

LIST OF TABLES

CHAPTER 1

INTRODUCTION

This work arose from the need to develop a theory which would enhance the use of pions as effective probes of nuclear structure. Experimental facilities have improved greatly in recent years, leading to a need for a quantitative description of pion inelastic scattering. The energy resolution and beam intensity of early pion experiments limited studies to isolated strong states of easily manufactured targets. The advent of the large meson factories (LAMPF in Los Alamos, TRIUMF in Vancouver, SIN in Switzerland), which were designed to produce useful beams of pions from high currents of intermediate energy protons, led to the study of a wider range of reactions and the discovery of some previously unknown states. The theory of pion-nucleus scattering followed a similar pattern, as sophisticated theories became necessary to explain the more precise experimental results.

The pion was predicted to exist in 1935 [Yuk 35], and after its discovery around 1947 it was soon applied to nuclear physics experiments. One of the earliest experiments measured the angular distribution of 62 MeV π^+ and π^- scattered from ^{12}C [Byf 52] in a cloud chamber. The development of scattering theory [Wat 53, Gel 53] found applications in photomeson production [Fra 53], nucleon-nuclear pion production [Kov 55] and the Kisslinger model [Kis 55] for pion scattering. The Kisslinger model was invented to explain the original data of Byfield *et al.*, and later data [Sap 56, Bak 58] were found to require [Bak 58a] this form of the potential.

Another surge of activity followed the experiment of Binon et al. [Bin 70] which measured pion scattering from 120 to 280 MeV at CERN. Two calculations of the inelastic transitions were soon published, one with collective [Edw 71] and the other with microscopic [Lee 71] models for the transition density. These assumed the Distorted Wave Born Approximation (DWBA) [Sat 64, Aus 70] and used the impulse approximation (IA) [Ker 59] for the pion-nucleus interaction. This thesis continues the development begun at that time, but with greater emphasis on the impact of recent improvements in the pion interaction on such calculations.

Once accurate data began accumulating, particularly for pionic atoms and low energy scattering, the need for higher order corrections to the Kisslinger theory became clear. The most important of these was the so-called Lorentz-Lorenz Ericson-Ericson (LLEE) effect [Eri 66]. A number of others, including phenomenological absorption terms, are outlined in the review article of Hufner [Huf 75]. Several more recent review articles [Bro 79, Tho 80, Eis 80] are useful background to the work in this thesis.

It should be emphasized that the point of view here focuses on a coordinate space potential. Many others are possible. A momentum space potential is used by Lee [Lee 74, Lee 77]. The delta-hole model [Hir 79, Ose 79, Ose 79a] is widely used in a microscopic description of pion scattering. Although neglected here, these other models are important to the understanding and interpretation of the optical model results in terms of the fundamental pion-nucleon interaction.

The experimental situation is characterized by the same diversity. Data exists for all pion reactions for some beam energy and target combination: pion angular distributions for specific final states via

elastic and inelastic scattering, single and double charge exchange reactions; inclusive measurements such as absorption, reaction, quasi-elastic and total cross sections; excitation functions and angular distributions for other quasi-elastic reactions involving nucleon knock-out which result in specific final states. As data accumulates for a systematic collection of targets and beam energies, an important role of the theory is to build a coherent picture out of the many pieces.

The purpose of this thesis is to examine the inelastic scattering data with the goal of understanding the properties of the effective pion-nucleus interaction. The starting point is a theoretical potential, developed elsewhere [Str 79, Str 79a], which incorporates various corrections to the IA result for the pion-nucleon interaction. The elastic scattering data are used to identify deficiencies in this theoretical potential and fix the strength of the isoscalar interaction. Comparison with the fit to a four-parameter potential allows the identification of general properties of this effective potential. These results are then used to calculate the inelastic cross sections, testing the interaction strength. This approach can then be extended to study isovector and spin-flip transitions, which are not determined by the elastic scattering.

This thesis divides naturally into two parts: the development of the equations and forces to be tested is done in the next two chapters, while the applications to inelastic scattering are given in the following three chapters.

Chapter 2 reviews the multiple scattering formulation of the pion-nucleus optical potential. Two forms of the potential are used, one related to the simple four-parameter Kisslinger potential, the other containing all of the kinematic and other corrections used [Str 79a] to

explain the elastic scattering. Each of these is fit to the elastic scattering data to define a phenomenological effective parameter set to complement the theoretical values. Chapter 3 reviews the derivation of the DWBA and works out the specific equations needed for these calculations.

Chapter 4 is the focal point of this work. Here the collective model is used to test the properties of the interaction and the effects of the various changes introduced to improve the fit to elastic scattering. In addition, the effects of different choices for the distorting potential are examined independently of the interaction that induces the inelastic transition. Chapter 5 introduces the microscopic model of the transition density, and also examines the spin-orbit interaction for S=1 transitions produced with pions. Chapter 6 introduces single charge exchange reactions, and gives some results as a means of examining the isovector part of the pion-nucleus interaction.

These results are summarized in Chapter 7, where the general properties of the effective interaction are used to give perspective to the discussion. There is much data, each with some systematic error, so it is only with a consistent approach that one can form these results into a unified whole.

The notation used here is listed in Table 1-1. Most of it is conventional, with the main exception being the ordering of the arguments in the symbol for a Clebsch-Gordon coefficient. The angular momentum algebra follows Brink and Satchler [Bri 75].

Table 1-1

Definitions of Symbols Used in This Work

Kinematic Variables

$\vec{k}$,	3-momentum and total energy of pion
$\vec{p}$, E	3-momentum and total energy of struck particle
primes	indicate variables for final state
subscript cm	pion-nucleon center of momentum system
subscript 2cm	pion-two nucleon center of momentum system
subscript ACM	pion-nucleus center of momentum system
no subscript	ACM unless otherwise noted
μ	pion rest mass
M	nucleon rest mass
M_N	rest mass of nucleus $\simeq$ AM
$\bar{\omega}$	reduced total energy in projectile-target center of momentum system

Others

ϕ	plane wave
Ψ	total scattered wavefunction = $\phi + \chi$
χ	scattered wave, also used for the "distorted" wave = wave scattered by optical potential only
$f_{\pi N}$	pion-nucleon scattering amplitude
$t_{\pi N}$	pion-nucleon t-matrix
$\underline{A}$	antisymmetrization operator
A	number of nucleons = Z+N
$\rho(r)$	isoscalar ground state density normalized to A nucleons ($= \rho_n + \rho_p$)
$\delta\rho(r)$	isovector ground state density normalized to Z-N nucleons ($= \rho_p - \rho_n$)
ε_π	pion charge

Angular Momentum

$\langle \ell m\ LM \vert JM_J \rangle$	same as $\langle \ell L\ m\ M \vert JM_J \rangle$ defined in Brink and Satchler
X(abc, def, ghi)	$= \begin{Bmatrix} a & b & c \\ d & e & f \\ g & h & i \end{Bmatrix}$ = 9-J symbol
$\hat{J}$	$= \sqrt{2J+1}$

CHAPTER 2

THE PION-NUCLEUS INTERACTION

The pion-nucleus interaction is a many body problem and there are a number of approaches to its solution, some of which are described in the previous chapter. Our approach is to reduce the problem to that of the interaction of a single particle with a potential which describes the average properties of the actual pion-nucleus interaction. This potential is derived using multiple scattering theory, which says that the pion-nucleus potential can be related to measured and calculated properties of the pion-nucleon interaction. The derivation used here follows that used by Stricker [Str 79a] and Brown [Bro 79], with an emphasis on those parts which are critical to the interpretation of inelastic scattering.

The first section outlines the multiple scattering theory as applied here. The remaining sections break into two distinct parts. In Sections 2.2 and 2.3 the first-order potential is obtained from the pion-nucleon scattering amplitude, and then compared with elastic scattering data. In Sections 2.4 and 2.5 the second-order terms are introduced and then compared with the data. In each case a purely theoretical potential will be presented, and then a potential fitted to the data will be obtained. This will give us the flexibility to compare phenomenological potentials with theoretical ones at various stages in the distorted waves analysis of inelastic scattering. Section 2.6 will summarize these results.

2.1 MULTIPLE SCATTERING THEORY

The purpose of this section is to develop a working basis for the calculations and discussions which follow. The theory here is

based on the work of Watson [Wat 53] and Kerman, McManus and Thaler [Ker 59], among others. The starting point for the description of a wave Ψ scattered by a Hamiltonian $H = K_o + V$, where K_o is the kinetic energy and V the interaction with the scatterer, is the scattering amplitude

$$f_{ab} = - \frac{\bar{m}}{2\pi \hbar^2} \left\langle \phi_b \middle| V \Psi_a \right\rangle \quad . \tag{2-1}$$

The scattering amplitude is just the projection of the scattered wave onto the plane wave ϕ in the outgoing channel. The scattering cross section is then

$$\frac{d\sigma}{d\Omega} = \left| f_{ab} \right|^2 \quad . \tag{2-2}$$

It is convenient to describe this process entirely in terms of operators. We write

$$\Psi = \phi + \chi = \phi + GV \Psi \tag{2-3}$$

where χ is the scattered part of Ψ and $G = (E - K_o + i\varepsilon)^{-1}$ is the Greens function for outgoing scattered waves. If we define $\Psi = \Omega\phi$ we get an operator equation

$$\Omega = 1 + GV \Omega \tag{2-4}$$

to replace the equation for the scattered waves [equation (2-3)]. The transition matrix is defined by

$$T = V \Omega \tag{2-5}$$

so that $V\Psi = T\phi$ and the definition of the scattering amplitude becomes

$$f_{ab} = - \frac{\bar{m}}{2\pi \hbar^2} \left\langle \phi_b \middle| T\phi_a \right\rangle = - \frac{\bar{m}}{2\pi \hbar^2} T_{ab} \quad . \tag{2-6}$$

Since $T = V\Omega$, equation (2-4) gives us an integral equation for T,

$$T = V + VGT \tag{2-7}$$

which is known as the Lippmann-Schwinger [Lip 50] equation, and is the starting point for the derivation. Before we continue, however, it will be necessary to examine the wave equation for the pion.

Since the pion is so light, it must be treated relativistically although the massive nucleus can be treated non-relativistically throughout. Then the Hamiltonian for the system is

$$H = \left(k^2 + \mu^2\right)^{1/2} + M_N + \frac{P^2}{2M_N} + V \tag{2-8}$$

where k, μ, P, M_N are the momentum and mass of the pion and nucleus, respectively. The Schrodinger equation for this system, $H\Psi = E_T\Psi$, was shown by Goldberger and Watson [Gol 64] to be equivalent to a Klein-Gordon-like equation

$$(k^2 + \mu^2)\Psi = \left(E_T - V - M_N - \frac{P^2}{2M_N}\right)\Psi \quad . \tag{2-9}$$

This can be simplified to

$$\left(\nabla^2 + k_o^2 - 2\bar{\omega}\, V + \frac{\bar{\omega}}{\omega} V^2\right)\Psi = 0 \tag{2-10}$$

where $\bar{\omega} = \omega E/(\omega + E)$ is the reduced energy and $k_o^2 = \omega^2 - \mu^2$. If we separate out the electromagnetic potential and drop the smaller terms we are left with

$$\left(\nabla^2 + k_o^2 - 2\bar{\omega}\, V_\pi - 2\bar{\omega}\, V_{EM} + \frac{\bar{\omega}}{\omega} V_{EM}^2\right)\Psi = 0 \quad . \tag{2-11}$$

Returning to the Lippmann-Schwinger equation, it will be convenient to work with the equivalent equation

$$2\bar{\omega}\ T = 2\bar{\omega}\ \ V_\pi + 2\bar{\omega}\ V_\pi G\ 2\bar{\omega}\ T \tag{2-12}$$

where $G = (-k^2 + k_o^2 + i\varepsilon)^{-1}$ with momenta defined in the π-nucleus system. The remainder of this section will show how this equation can be rearranged so that all the important (large) terms can be integrated over the target, thus reducing this to an equivalent one-body equation. Kerman, McManus and Thaler [Ker 59] showed that it is particularly convenient to use antisymmetrized intermediate states. We can do this by introducing $\underset{\sim}{A}$, an operator that projects onto totally antisymmetric target states, into equation (2-12) as is also done in [Mac 73]. This is possible since $\underset{\sim}{A}$ commutes with G and V and since we will only take matrix elements of T between correctly symmetrized nuclear states. Then our starting equation is

$$T = V + VG\left|\underset{\sim}{A}2\bar{\omega}\right|T \tag{2-13}$$

For convenience, the factor of $\underset{\sim}{A}2\bar{\omega}$ will be suppressed from here on except when it is important for a particular result.

The first step is to define an auxillary potential matrix by

$$U = V + VGQ_oU \tag{2-14}$$

where $Q_o = 1 - P_o = 1 - |0\rangle\langle 0|$ projects off of the ground state. It is the assumption of what follows that this subseries converges rapidly since the matrix elements connecting the initial (ground) state to excited states should be smaller than the diagonal matrix elements.

This allows us to rewrite equation (2-13) by using $V = U(1 + GQ_oU)^{-1}$ so that

$$\begin{aligned} T &= U(1 + GQ_oU - GQ_oU)(1 + GQ_oU)^{-1}(1 + GT) \\ &= U(1 + GT) - UGQ_oU(1 + GQ_oU)^{-1}(1 + GT) \\ &= U(1 + GT) - UGQ_oT \\ &= U + UG(1 - Q_o)T \end{aligned} \tag{2-15}$$

which gives us the integral equation

$$T = U + UGP_oT \tag{2-16}$$

for T in terms of U.

Returning to equation (2-14), we now use that $V = \sum v$, where v is the interaction with one nucleon, and the sum runs over all N target particles. Because of the operator $\underset{\sim}{A}$ in the definition, all of these nucleons are equivalent and we can write

$$U = Nv + Nv\ GQ_o(\underset{\sim}{A}\, 2\bar{\omega})U \quad . \tag{2-17}$$

We now define an effective two-body operator τ by

$$\tau = v + vGQ_o\tau \quad . \tag{2-18}$$

If we use $v = \tau(1 + GQ_o\tau)^{-1}$ in equation (2-17) we get

$$\begin{aligned} U &= N\tau(1 + GQ_o\tau)^{-1}(1 + GQ_oU) \\ &= N\tau(1 + GQ_oU) - N\tau\ GQ_o\ v(1 + GT) \\ &= N\tau(1 + GQ_oU) - N\tau\ GQ_oU/N \\ &= N\tau + (N - 1)\tau\ GQ_oU \quad . \end{aligned} \tag{2-19}$$

If we define

$$U = \frac{N}{N-1} U'$$

and

$$U' = (N-1)\,\tau + (N-1)\,\tau\, GQ_o U' \tag{2-20}$$

we get the multiple scattering series for U.

It remains to relate the effective operator τ to the free pion-nucleon t-matrix. The latter is defined by

$$t_{\pi N} = v + vg\, 2\bar{\omega}_{cm}\, t_{\pi N} \tag{2-21}$$

where $g = (-k^2 + k_o^2 + i\varepsilon)^{-1}$ with momenta defined in the π-nucleon system. Again, by writing $v = t_{\pi N}(1 + g\, t_{\pi N})^{-1}$ and substituting into equation (2-18) we obtain

$$\tau = t_{\pi N} + t_{\pi N}(GQ_o\ \underline{A} 2\bar{\omega} - g\, 2\bar{\omega}_{cm}) \tag{2-22}$$

using the same algebraic technique as in equation (2-15). The Impulse Approximation (IA) assumes the higher order terms in equation (2-22) can be neglected so that

$$\tau \cong t_{\pi N} \quad . \tag{2-23}$$

This approximation will be used throughout this work. With this assumption, the multiple scattering series for U can be written as

$$2\bar{\omega}\, U = N\, 2\bar{\omega}\, t_{\pi N} + N(N-1)\, 2\bar{\omega}\, t_{\pi N}\, GQ_o\ \underline{A} 2\bar{\omega}\, t_{\pi N}$$

$$+ N(N-1)^2\, 2\bar{\omega}\, t_{\pi N}\, GQ_o\ \underline{A} 2\bar{\omega}\, t_{\pi N}\, GQ_o\ \underline{A} 2\bar{\omega}\, t_{\pi N} + \cdots \quad . \tag{2-24}$$

This series for U will be the basis of our analysis of the pion-nucleus interaction. This work will not focus on the specific effects of each of the terms in equation (2-24), as these are discussed in Stricker's thesis [Str 79a], but will restrict the discussion to two broad cases. In Section 2.2 the first order part of this,

$$2\bar{\omega}\, U = N\, 2\bar{\omega}\, t_{\pi N} \quad , \tag{2-25}$$

will be examined. In Section 2.4 some of the higher order terms will be evaluated and summed to give the second order corrections to the interaction.

2.2 THE FIRST ORDER POTENTIAL

The starting point for this analysis is the measured pion-nucleon scattering amplitude. A convenient parametrization is

$$\begin{aligned} f_{\pi N} = {} & (b_o + b_1 \underset{\sim}{t}\cdot\underset{\sim}{\tau}) + (c_o + c_1 \underset{\sim}{t}\cdot\underset{\sim}{\tau})\vec{k}\cdot\vec{k}' \\ & + (s_o + s_1 \underset{\sim}{t}\cdot\underset{\sim}{\tau})\, \vec{\sigma} \cdot (\vec{k} \times \vec{k}') \end{aligned} \tag{2-26}$$

where $\underset{\sim}{t}$ and $\underset{\sim}{\tau}$ are the pion and twice the nucleon isospin operators, $\vec{k}$ is the pion momentum in the center of mass (to be written k_{cm} from here on), and $\vec{\sigma}$ is twice the nucleon spin operator. Appendix A defines the relationship between the parameters b_i, c_i, s_i and the corresponding pion-nucleon phase shifts. These phase shifts are computed from the parametrization of Rowe, Salomon and Landau, [Row 78] who fit an analytic function to the phase shift data below 400 MeV. This approach has the advantage of producing smooth, well-behaved results even where the data are particularly noisy, as is the case in the S_{11} channel below 100 MeV.

The values of these parameters are plotted in Figure 2-1. Notice that Reb_0 (solid curve) is nearly zero at low energy, due to cancellation between the S_{11} and S_{31} phase shifts, and becomes increasingly repulsive with increasing energy. Reb_1 (dashed curve), the isovector s-wave parameter, is roughly constant and repulsive. $Re\bar{b}_0$ (dash-dot curve) includes second order corrections and will be discussed in Section 2.4. Imb_0 increases slowly while Imb_1 is small at all energies. In contrast, the p-wave parameters c_0 (solid curve) and c_1 (dashed curve) demonstrate simple resonance behavior, reflecting the dominance of the P_{33} channel due to the low-lying $\Delta(1232)$ resonance. The spin-orbit parameters also vary rapidly as they are also dominated by the Δ_{33} resonance.

The pion-nucleon transition matrix is simply related to the scattering amplitude by

$$t_{\pi N}(k_{cm},\ k'_{cm}) = \frac{-4\pi}{2\bar{\omega}_{cm}}\ f_{\pi N}(k_{cm},\ k'_{cm}) \qquad (2\text{-}27)$$

and

$$t_{\pi N}(k,\ k',\ p,\ p') = (2\pi)^3\ \delta(k'+p'-k-p)\ t_{\pi N}(k_{cm},\ k'_{cm})\ . \qquad (2\text{-}28)$$

This is then used to generate the multiple scattering series for U as defined in equation (2-24) above. The lowest order result for the optical potential, with N=A nucleons, is

$$\begin{aligned} 2\bar{\omega}\ U_{opt} &= \langle 0|\, 2\bar{\omega}\ U|0\rangle \\ &= A\ \langle 0|\, 2\bar{\omega}\ t_{\ N}|0\rangle \\ &= A\ \langle 0|\, (2\pi)^3\ \delta(k+p-k'-p')\ \left[-4\pi\ \frac{\bar{\omega}}{\bar{\omega}_{cm}}\right] f_{\pi N}|0\rangle \end{aligned} \qquad (2\text{-}29)$$

Figure 2-1

Real and imaginary parameters of the pion-nucleon scattering amplitude, isoscalar (isovector) shown with a solid (dashed) curve.

MSUX-81-093

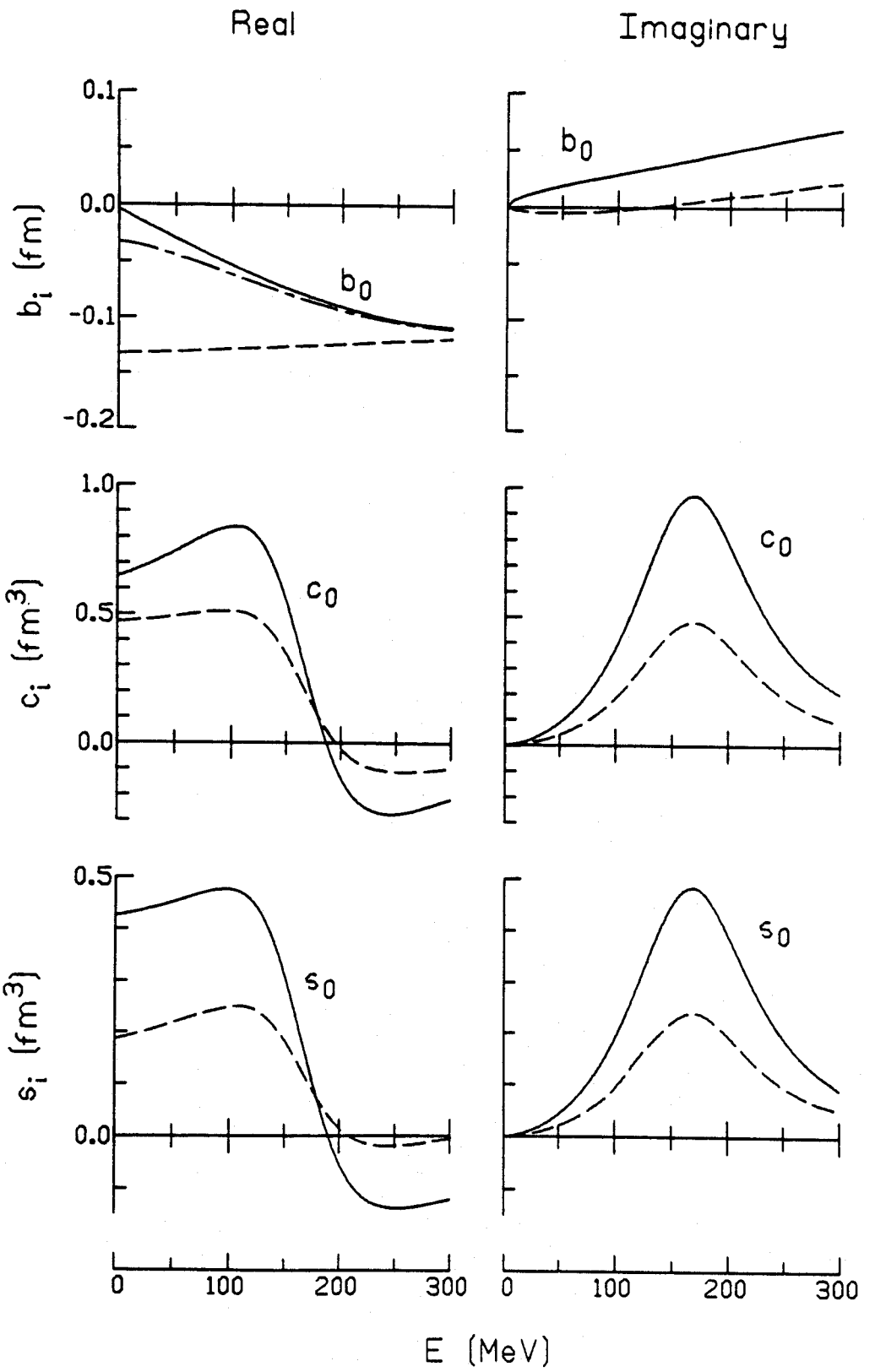

Figure 2-1

where $|0\rangle = \Psi(p, p_2, \cdots, p_A)$ and $\langle 0| = \Psi(p', p_2, \cdots, p_A)$. Since $f_{\pi N}$ is independent of p this can be reduced to

$$2\bar{\omega}\, U_{opt} = -4\pi \left[\frac{\bar{\omega}}{\bar{\omega}_{cm}}\right] f_{\pi N}(k, k')\ \rho(q) \qquad (2\text{-}30)$$

where $q = k'-k$ and the factor A has been incorporated into $\rho(q)$. If we assume a nucleus with N=Z we can conveniently drop the isovector terms. Further, the spin-orbit terms vanish for a closed-shell spin-0 nucleus, and will be small otherwise [Lov 81]. Then

$$2\bar{\omega}\, U_{opt}(k, k') = -4\pi \left[\frac{\bar{\omega}}{\bar{\omega}_{cm}}\right]\left(b_o\ \rho(q) + c_o\ \rho(q)\ \vec{k}\cdot\vec{k}'\right)$$

or (2-31)

$$2\bar{\omega}\, U_{opt}(r) = -4\pi \left[\frac{\bar{\omega}}{\bar{\omega}_{cm}}\right]\left(b_o\ \rho(r) - \vec{\nabla}\cdot\left[c_o\ \rho(r)\right]\ \vec{\nabla}\right)$$

are the appropriate forms for the optical potential. Other forms, particularly the local Laplacian form, are described in Appendix B.

Although this is a reasonable representation for the first order potential, it is not really complete because the potential will be used in the pion-nucleus center of mass (ACM) while $f_{\pi N}$ has been defined in the pion-nucleon center of mass (cm). The transformation needed is not well defined in this case because the interaction is not written in terms of invariants. Relativistic potential theory [Lan 73] gives one prescription for this, and this widely used [Tho 80, Bro 79] method will also be adopted here without further argument. Its effects are discussed in [Str 79a]. The prescription is to use

$$\langle k'p'|\, t_{Acm}\, |k-p\rangle = -4\pi(2\pi)^3\ \delta(k'+p'-k-p)\ \frac{\bar{\omega}}{\bar{\omega}_{cm}}\ \gamma\ f_{\pi N}(k'_{cm}, k_{cm}) \qquad (2\text{-}32)$$

where $\gamma = \frac{E_{cm}}{E}\frac{\omega_{cm}}{\omega}\frac{E'_{cm}}{E'}\frac{\omega'_{cm}}{\omega'} \simeq \frac{\omega_{cm}}{\omega}$

and $f_{\pi N}$ is evaluated at the pion-nucleon center of mass energy. The reader is reminded that unsubscripted variables are in the ACM system in the remainder of this thesis. Since

$$\gamma \frac{\bar{\omega}}{\bar{\omega}_{cm}} \simeq \frac{\omega_{cm}}{\omega}\frac{\bar{\omega}}{\bar{\omega}_{cm}} = \frac{1+\varepsilon}{1+\varepsilon/A} \quad , \tag{2-33}$$

the only change is the addition of this factor that multiplies the entire potential.

It is also necessary to express the momenta k_{cm}, k'_{cm} in the pion-nucleus center of mass as well. This will affect both the p-wave and the spin-orbit terms. The Lorentz transformation for $\vec{k}_{cm}$ is

$$\vec{k}_{cm} = \vec{k} + \vec{\beta}\left(\frac{\gamma}{\gamma+1}\vec{\beta}\cdot\vec{k} - \omega\right) \tag{2-34}$$

where $\beta = (\vec{k} + \vec{p})/(E + \omega)$, with a similar result for k'_{cm}. To first order this simplifies to

$$\vec{k}_{cm} = \frac{\vec{k}E - \vec{p}\omega}{E+\omega} \simeq \frac{\vec{k} - \varepsilon\vec{p}}{1+\varepsilon} \quad . \tag{2-35}$$

A particularly convenient way to do this "angle transformation" is to rewrite the equations in terms of

$$\begin{aligned} \vec{P} &= \frac{1}{2}(\vec{p}+\vec{p}') & \vec{p} &= \vec{p}'-\vec{p} \\ \vec{Q} &= \vec{k}+\vec{k}' & \vec{q} &= \vec{k}'-\vec{k} = -\vec{p} \end{aligned} \tag{2-36}$$

since the equations corresponding to (2-35) are

$$\vec{q}_{cm} = \vec{q} \quad \text{and} \quad \vec{Q}_{cm} = \frac{\vec{Q}}{1+\varepsilon} - \frac{2\varepsilon}{1+\varepsilon}\vec{P} \quad . \tag{2-37}$$

Then the transformation gives

$$\vec{k}_{cm}\cdot\vec{k}'_{cm} = \frac{1}{4}\left(Q_{cm}^2 - q_{cm}^2\right)$$

$$= \frac{1}{4}\frac{Q^2}{(1+\varepsilon)^2} - \frac{q^2}{4} - \frac{\varepsilon}{(1+\varepsilon)^2}\vec{P}\cdot\vec{Q} + \frac{\varepsilon^2}{(1+\varepsilon)^2}P^2 \qquad (2\text{-}38)$$

so that

$$\vec{k}_{cm}\cdot\vec{k}'_{cm} = \frac{1}{(1+\varepsilon)^2}\vec{k}\cdot\vec{k}' - \frac{\varepsilon}{(1+\varepsilon)^2}\frac{q^2}{2}$$

$$- \frac{\varepsilon}{(1+\varepsilon)^2}\vec{P}\cdot\vec{Q} + \frac{\varepsilon^2}{(1+\varepsilon)^2}P^2 \qquad (2\text{-}39)$$

The integration over the ground state momenta, called Fermi averaging, causes [Bro 79] the third term to vanish and the fourth term becomes proportional to the kinetic energy density in the Thomas-Fermi approximation,

$$K(r) = \frac{3}{5}\left(\frac{3}{2}\pi^2\right)^{2/3}\rho^{5/3} \quad . \qquad (2\text{-}40)$$

This term, which acts like an attractive s-wave term in the potential, will be ignored, as in [Str 80], by incorporating it in the second order corrections added in Section 2.4. In the fixed scatterer approximation it is ignored altogether.

The transformation of the spin-orbit term involves

$$\vec{k}_{cm}\times\vec{k}'_{cm} = \frac{1}{2}\vec{Q}_{cm}\times\vec{q}_{cm} = \frac{1}{2}\frac{1}{1+\varepsilon}\vec{Q}\times\vec{q} - \frac{\varepsilon}{1+\varepsilon}\vec{P}\times\vec{q} \qquad (2\text{-}41)$$

so that

$$\vec{k}_{cm}\times\vec{k}'_{cm} = \frac{1}{1+\varepsilon}\vec{k}\times\vec{k}' + \frac{\varepsilon}{1+\varepsilon}\vec{p}\times\vec{p}' \quad . \qquad (2\text{-}42)$$

The second term will be dropped. This term can contribute to elastic scattering from nuclei with spin-unsaturated subshells [Lov 81], such as ^{48}Ca. In addition, it can affect normal parity inelastic transitions, but will not be a significant part of the interaction for the states considered in this work. Notice that the spin-orbit force comes in with one less factor of $(1+\varepsilon)$ in the kinematics. Since this part of the potential only contributes to S=1 inelastic transitions, we will not return to it until much later.

If we collect together what we already have and include the isovector terms, we get the first order optical potential that will be used here. It is

$$2\bar{\omega}\, U_{opt}(r) = -4\pi \Big\{ p_1 \,[b_o\, \rho(r) + \varepsilon_\pi\, b_1\, \delta\rho(r)] - p_1^{-1}\, \vec{\nabla}\cdot [c_o\, \rho(r) + \varepsilon_\pi\, c_1\, \delta\rho(r)]\, \vec{\nabla} + \frac{1}{2}\left(1 - p_1^{-1}\right) \nabla^2\, [c_o \rho(r) + \varepsilon_\pi\, c_1\, \delta\rho(r)] \Big\} \qquad (2\text{-}43)$$

where $p_1 = (1+\varepsilon)/(1+\varepsilon/A)$, ε_π = pion charge, $\delta\rho(r) = \rho_p(r) - \rho_n(r)$ and ρ, ρ_p, ρ_n are normalized to A, Z, N, respectively. The densities are usually assumed to have the same radial dependence so that

$$\varepsilon_\pi\, \delta\rho(r) = \varepsilon_\pi\, \frac{Z-N}{A}\, \rho(r) \quad . \qquad (2\text{-}44)$$

2.3 CALCULATIONS WITH FIRST ORDER OPTICAL POTENTIAL

The properties of this potential will be illustrated with a series of calculations at a representative set of energies -- zero, 50 MeV and 162 MeV -- for a range of nuclei. The zero energy calculations are for the shifts and widths of levels in pionic atoms. The calculations use a modified version of MATOM [Seki] and are compared to the available

data. The other calculations are for elastic scattering from ^{16}O, ^{40}Ca (at 50 MeV only), ^{208}Pb. These results are obtained using a modified version of the program PIRK [Eis 74]. The density parameters for these calculations are taken from electron scattering. Tables are given in Appendix C.

Three sets of calculations will be described. The first, designated as Parameter Set A throughout this work, uses the phase shift values for the parameters b_o, b_1, c_o, c_1 in the optical potential defined in equation (2-43). These are listed in Table 2-1. This illustrates the effect of the lowest order estimate to the optical potential. The second, designated as Parameter Set B, results when fitted values for Reb_o and Imb_o, (at 50 MeV only) Rec_o and Imc_o are used. The fitting procedure was to minimize the average χ^2/point for all the data available at the given energy. These parameters are listed in Table 2-2. An auxillary Set, B', as defined at 50 MeV, varies only 3 independent parameters since the ratio of Imb_o/Imc_o was held fixed at the value determined by pionic atoms. These sets illustrate the effective potential required by the data at these energies which will be valuable when we look at the effects of the second order corrections in the next part of this chapter. A different Set B' is defined at higher energies. In this case the fit varies Rec_o and Imc_o as before, except the ∇^2 term in the optical potential is ommitted. This set allows a comparison to the potential used by Holtkamp and Cottingame [Cot 80].

The first illustration of the effects of these potentials will be taken from pionic atoms. Measurements of the strong interaction shift of level energies for 1s [Tau 74] and 2p [Bat 78] levels provide information on the real parts of the s- and p-wave potentials, respectively.

Table 2-1

Parameter Set A, Impulse Approximation Values for the Four-Parameter Optical Potential

	π-Atom	50 MeV	162 MeV
b_o	-0.006	-0.030 + 0.019 i	-0.079 + 0.041 i
b_1	-0.133	-0.131 - 0.005 i	-0.125 + 0.005 i
c_o	0.65	0.75 + 0.090 i	0.36 + 0.96 i
c_1	0.47	0.45 + 0.044 i	0.21 + 0.48 i

Table 2-2

Parameter Sets B and B', Fitted Values for the Four-Parameter Optical Potential as Described in the Text

	π-Atom	50 MeV (B')	50 MeV	162 MeV	162 MeV (B')
b_o	-0.0445 +0.0148 i	-0.0680 +0.017 i	-0.0686 +0.0064 i	-0.079 +0.041 i	-0.079 +0.041 i
c_o	0.513 +0.0343 i	0.550 +0.038 i	0.557 +0.091 i	0.58 +0.66 i	0.72 +0.68 i

The corresponding widths of these levels provide information on the imaginary parts of the s- and p-wave potentials. Since the potential under consideration has only four parameters (the isovector parameters are kept fixed), the effect of each one is easily identified. Specifically, the negative value of $\mathrm{Re}b_o$ produces the repulsive shift of the s-wave levels while the positive value of $\mathrm{Re}c_o$ produces the attractive shift of the p-wave levels. The level widths result from absorption which is modeled by the imaginary parts of b_o and c_o. This makes the

fitting procedure straightforward -- the values of b_o and c_o are varied to minimize the χ^2 for the s- and p-wave shifts and widths separately -- although there is an interdependence between some of these parameters that requires careful checking of the fit.

The results of this fit are given as Set B; the calculated shifts and widths are shown in Figure 2-2. It is not possible to calculate and plot similar results for the values of Parameter Set A as they do not produce a solution for a bound state in MATOM. However, the tabulated values for Set A are sufficient for a comparison. A reference to Tables 2-1 and 2-2 makes it immediately clear that the IA value for Reb_o is much too small to explain the s-wave repulsion required by the data. In contrast, the IA value for Rec_o is too large to explain the p-wave attraction indicated by the data. Since the IA potential is purely real at zero energy, Set A cannot explain the absorption of the pion in the nucleus. These phenomena -- increased s-wave repulsion, decreased p-wave attraction, true absorption of the pion -- are critical to the understanding of low energy pion scattering. Much of the study of the second-order potential is directed towards explaining these properties.

The other illustrations of the application of these potentials are taken from elastic scattering. These measurements are no less sensitive to the different pieces of the potential, although the effects cannot be clearly separated as is the case for pionic atoms. The low energy (50 MeV) scattering is dominated by the interference between the s- and p-wave potentials, which shows up as a minimum near 60° in the elastic scattering angular distribution. Furthermore, absorption dominates the

Figure 2-2

Calculation of pionic atom shifts and widths using Set B, which was fit to these data.

MSUX-81-094

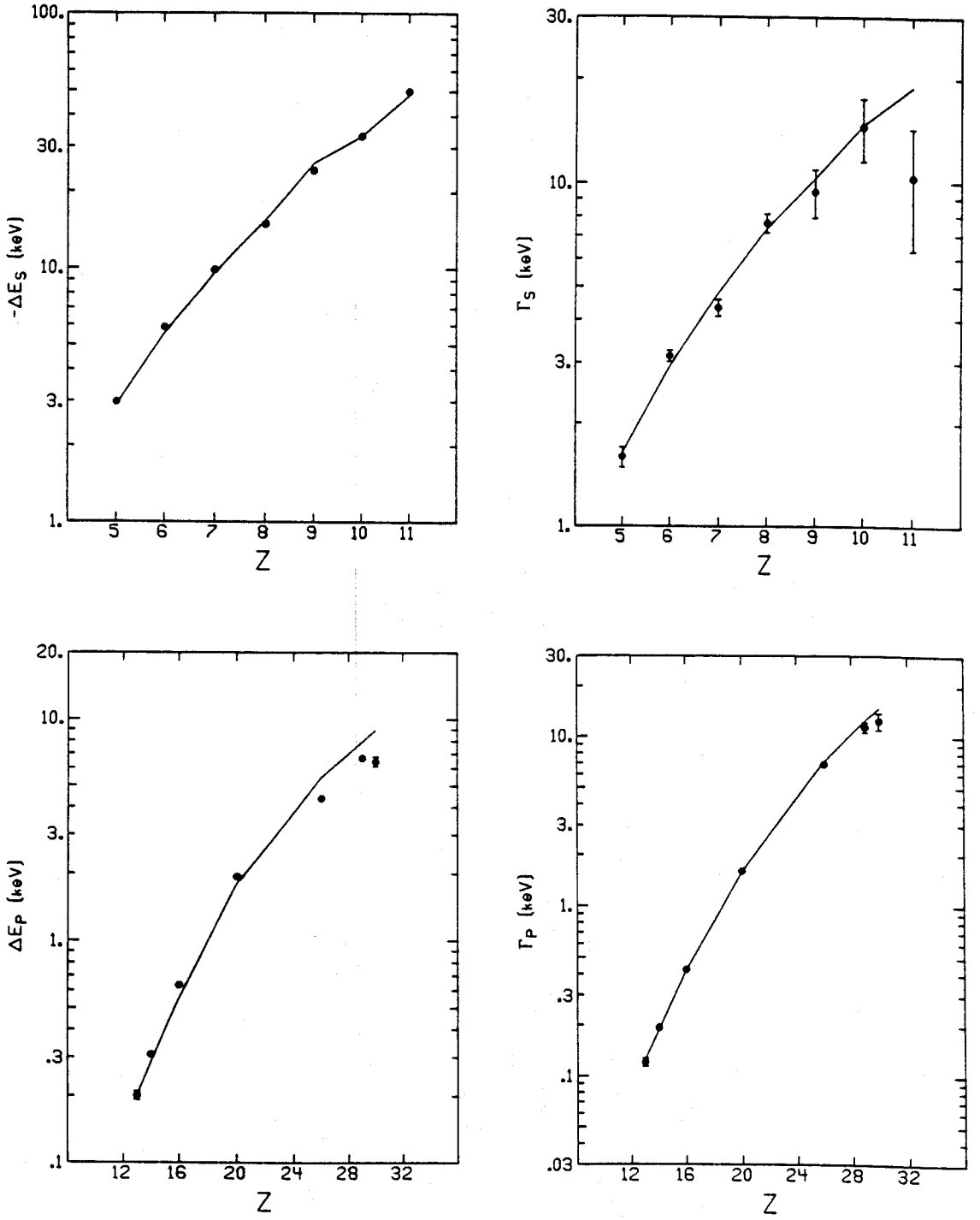

Figure 2-2

reaction cross section and has important effects on the elastic scattering process. Higher energy (162 MeV) scattering is dominated by the p-wave (Δ_{33}) resonance, so c_o is the important parameter. Since the nucleus is quite "black" at these energies, diffraction effects dominate the angular distribution. Sample calculations for sets A, B and B', described below, are shown in Figure 2-3.

The calculations using IA values (Set A) are shown with dashed curves. At low energy these results are clearly wrong. The IA values of Reb_o and Rec_o produce an interference minimum near 75° and the magnitudes are incorrect. On the other hand, the high energy results are much closer to reproducing the data. This occurs because the potential has sufficient absorption to produce the diffractive scattering that is observed. Several authors [Thi 76, Joh 78] have remarked on the fact that a sharp cutoff model will reproduce the angular distribution at small angles.

The calculations using fitted potentials require some discussion. The fits are global in the sense that a single set of optical parameters was determined by simultaneously fitting all nuclei for which data were available. The average χ^2/point was minimized for the entire data set. At 50 MeV there were seven nuclei used: ^{12}C, ^{16}O, ^{28}Si, ^{56}Fe from Dytman et al. [Dyt 79] and ^{12}C, ^{16}O, ^{40}Ca, ^{90}Zr, ^{208}Pb from Preedom et al. [Pre 81]. At 162-163 MeV there were six nuclei available: ^{12}C from Piffaretti et al. [Pif 77], ^{28}Si, ^{58}Ni, ^{208}Pb from Olmer et al. [Olm 80] and ^{16}O, ^{40}Ca from Ingram et al. [Ing 78].

The 50 MeV fits were obtained for a four-parameter fit (Set B) and a three-parameter fit (Set B') where the ratio of Imb_o/Imc_o was held constant at the pionic atom value. These are shown with the solid

Figure 2-3

Elastic scattering with 50 MeV (left) and 162 MeV (right) π^+ calculated with parameters from sets A (impulse approximation), B and B', shown with dashed, solid and dash-dot curves, respectively

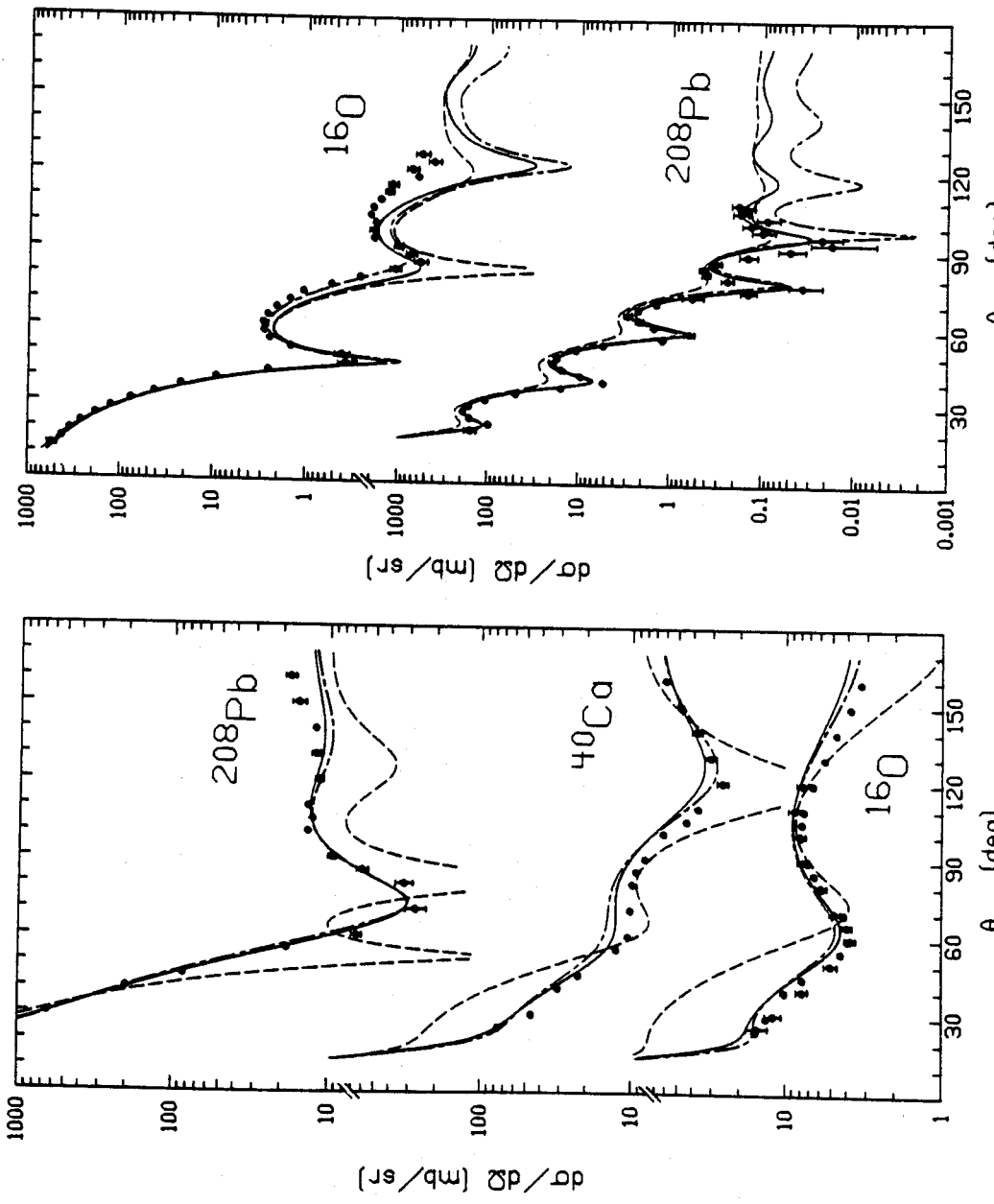
dσ/dΩ (mb/sr)
1000
100
10
1
0.1
0.01
0.001
30
60
90
120
150
θc.m.(deg)
16O
208Pb
40Ca

Figure 2-3

and dash-dot curves, respectively. Set B provides a slightly better fit but the difference is not very significant except at small angles, where the s-wave interferes with the coulomb amplitude. Notice that the improved agreement for these fitted sets comes about due to an increase in the s-wave repulsion and a decrease in the p-wave attraction, just as for pionic atoms. Notice also that the distribution of absorption between s- and p-wave is quite different for Set B compared to Set B'. Dytman [Dyt 77] obtained similar results for an unconstrained four-parameter fit, with all of the absorption going into $\mathrm{Im}c_0$ due to the lack of the ∇^2 term [Yoo 81]. The difficulty with this is that it lacks continuity with the pionic atom results. Set B' shows that a good fit can be obtained without substantially altering the energy dependence of the parameters. Since the model to be developed in the next section will use parameters that connect smoothly to pionic atoms, Set B' will be useful for comparison.

The 162 MeV fits were more difficult to obtain. Part of this seems related to normalization differences between the data taken at different laboratories by different groups. The solution was to examine a few nuclei in detail; adjustment of the normalization of the ^{16}O data by 10% produced consistent results. Others [Holt] seeking global fits have had to do similar things. The results are always presented without renormalization so the trends will be clear and not obscured by any scaling. For consistency, the data were only fit out to the second minimum, since the data sets cover quite different angular ranges. The fit with Set B (solid curve) is not substantially different from the results with Set A (dashed curve); the location of the minima are not

correctly reproduced. The fit with Set B' (dash-dot curve) is much better although the parameters are nearly the same as those in Set B. The increase in Rec_0 and decrease in Imc_0 is consistent with the energy shift proposed by [Cot 80]. This method is crude, but the results in Figure 2-3 serve to indicate the sensitivity of the calculation to variations of the parameters on this scale.

We can summarize the low energy results by observing that the s-wave repulsion (b_0) must be increased and the p-wave attraction (c_0) decreased. The absorption at 50 MeV is about 60% of the pionic atom value. The agreement with the data at higher energies is much better, with the uncorrected first order potential doing a reasonable job. Dropping the ∇^2 term improves the fit at low angles by making the nucleus look smaller; large angle cross section measurements may be a means to test whether this is a reasonable form of the potential.

2.4 HIGHER ORDER CORRECTIONS TO THE PION POTENTIAL

This section will discuss the contributions to the pion nucleus interaction from second and higher order terms in the multiple scattering series [equation (2-12)]. There are essentially three changes that occur. First, there is a second order correction to b_0 that increases the s-wave repulsion, working against the kinetic energy density term. This is important since Reb_0 is so small at low energies. Second, it is possible to sum the series for the p-wave part of the potential, an effect first described by Ericson and Ericson. [Eri 66]. Known as the Lorentz-Lorenz Ericson-Ericson (LLEE) effect because of the analogy to the Lorentz-Lorenz effect in dielectrics, it reduces the p-wave attraction. Third, the true absorption of a pion, which must occur on two or

more nucleons to conserve energy and momentum, will be included. The absorption of pions is a dominant part of the cross section at low energies and must be included in any discussion of the optical potential.

The first correction is to add the second order contribution to b_o. This is very important since the first order value for b_o is nearly zero due to the cancellation between the S_{11} and S_{31} phase shifts. The second order part of the optical potential is

$$4\pi\, p_1^{\,2}\, \frac{A-1}{A} \left(b_o^{\,2} + 2b_1^{\,2} \right) I\, \rho(r) \qquad (2\text{-}48)$$

so that we can define

$$\bar{b}_o = b_o - p_1 \left(b_o^{\,2} + 2b_1^{\,2} \right) I \qquad (2\text{-}49)$$

where I involves the expectation value of the two-nucleon correlation function. The result at zero momentum is

$$I = \frac{3k_f}{2\pi} \quad , \qquad (2\text{-}50)$$

assuming the Fermi Gas Model for the correlation function, and decreases rapidly as energy increases [Str 79a]. This parameter is plotted as the dash-dot curve in Figure 2-1, where its importance at low energies can be clearly seen. There are new results [McM 81] that suggest a further enhancement of $\bar{b}_o$ due to medium effects involving p-wave rescattering.

There is a second order correction, exactly analogous to $\bar{b}_o$, that comes in for the p-wave as well. This is small at low energies, but works against c_o in the resonance region. We will not investigate it here, but it should be important in getting the magnitudes of the theoretical parameters correct.

The most important second order correction is the Lorentz-Lorenz Ericson-Ericson (LLEE) effect, which is also the least well understood. First derived by Ericson [Eri 66], it is a result of summing the p-wave terms to all orders in the multiple scattering series. Assuming hard core repulsion between nucleons, the p-wave potential is

$$\vec{\nabla} \cdot 4\pi\, p_1^{-1}\, c_o \rho \sum_m \left[-\frac{4\pi}{3} \frac{A-1}{A}\, c_o\, p_1^{-1} \rho \right]^m \vec{\nabla}$$

$$= \vec{\nabla} \cdot \left[\frac{4\pi\, p_1^{-1}\, c_o \rho}{1 + \frac{4\pi}{3} \frac{A-1}{A}\, p_1^{-1}\, c_o \rho} \right] \vec{\nabla} \qquad (2\text{-}51)$$

The original derivation, in analogy to the electrostatic Lorentz-Lorenz effect, assumed the only effect was due to the "polarization" of the medium by the strong p-wave interaction through the Δ_{33} resonance. Subsequent calculations, particularly those by Brown [Bay 75], Weise [Ose 79], Eisenberg [Eis 73] and their collaborators, have included effects due to π, ρ, ω intermediate states and finite range effects. These modify the form of the LLEE effect by introducing a parameter λ in the formula

$$\frac{4\pi\, p_1^{-1}\, c_o \rho(r)}{1 + \frac{4\pi}{3} \lambda\, p_1^{-1}\, c_o \rho(r)} \qquad (2\text{-}52)$$

so that the original result corresponds to $\lambda = 1$. The consensus of recent calculations [Bay 75, Thi 76a] is that $1 < \lambda < 2$, with values around 1.6 to 1.8 being preferred [Ose 79] at low energy. The value of 1.6 will be used here as it falls in a range preferred by low energy data. These larger values serve to substantially decrease the p-wave

strength at low energies, a decrease that is important if agreement with the data is to be obtained. The value at higher energies is very poorly known, the choice of $\lambda = 1$ reflects that the value of λ should decline as energy increases and correlations become less important.

Last but not least, the effect of true absorption must be included. The absorption of a pion by two nucleons is the dominant part of the reaction cross section at low energies. Early pionic atom analyses assumed that

$$B_o \rho^2(r) - C_o \vec{\nabla} \cdot \rho^2(r) \vec{\nabla} \qquad (2\text{-}53)$$

would be a convenient parametrization, with the ρ^2 terms reflecting the fact that a two-nucleon density is required. It seems reasonable to cast the absorption into this form, but others [Ose 79] strongly suggest that this is only true below 50 MeV. Since approximate calculations [Cha 79] of these parameters, based on Fermi gas wave functions for the struck nucleons, exist over the full range of energies to be studied, we will adopt this form. Specifically, we take

$$B_o + C_o \vec{k}_{2cm} \cdot \vec{k}'_{2cm} \qquad (2\text{-}54)$$

to represent the absorption, where k_{2cm} is defined in the two-nucleon pion center of mass. The transformation from the pion-nucleus system to this system is the same as before except that $(1+\varepsilon)$ becomes $(1+\varepsilon/2)$.

The parameters calculated by Chai and Riska [Cha 79] are given in Figure 2-4. The short dashed lines at low energy indicate the values determined by pionic atoms, as will be described below. Although there are good arguments both against and in favor of these theoretical

Figure 2-4

Real and imaginary parameters used to describe absorption of a pion on two nucleons, isoscalar (isovector) parts shown with a solid (dashed) curve.

MSUX-81-096

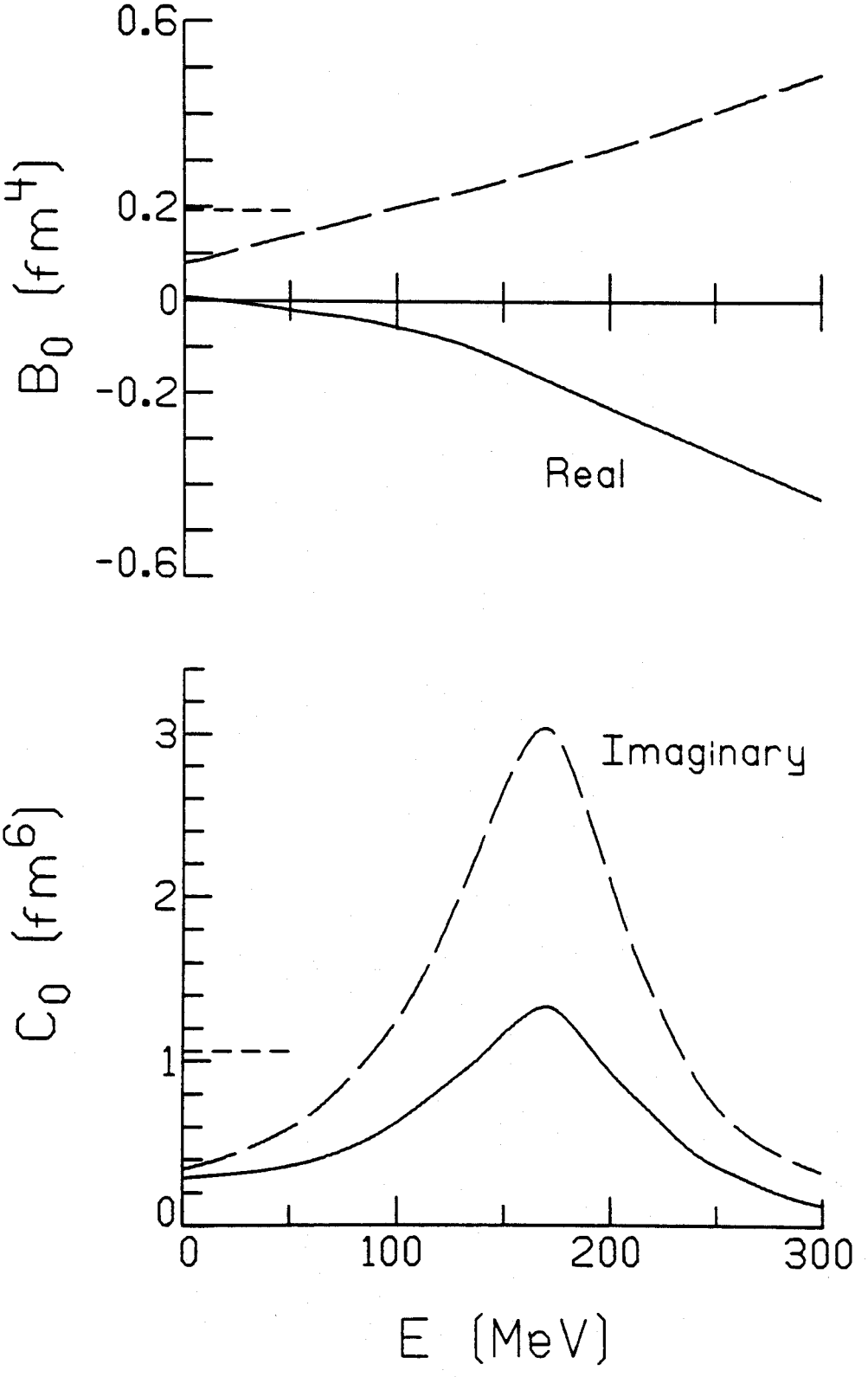

Figure 2-4

values, an empirical argument for them is that they have the behaviour that one would expect for absorption dominated by the Δ_{33} resonance.

When the absorption is included explicitly, it becomes necessary to identify Imb_o and Imc_o with the quasi-elastic cross section. When this is done it is necessary to reduce their phase shift value by a factor Q which accounts for Pauli blocking of inelastic scattering of the nucleon. Following [Str 79], this is evaluated from Goldberger's formula [Gol 48] using Landau and McMillan's approach [Lan 73]. This factor is 0.31 at 50 MeV, 0.54 at 100 MeV and 0.72 at 162 MeV. Results for $\sigma_{q.e.}$ appear consistent [Str 79a] with the limited data that is available.

When these new terms are combined with the first order terms already included in U_{opt} in equation (2-43), we get

$$2\bar{\omega}\, U_{opt} = -4\pi \Big\{ p_1 [b_o\, \rho(r) + \varepsilon_\pi\, b_1\, \delta\rho(r)] + p_2\, B_o\, \rho^2(r)$$

$$- \vec{\nabla} \cdot \frac{C(r)}{1 + \frac{4\pi}{3}\lambda\, C(r)}\, \vec{\nabla}$$

$$+ \frac{1}{2}\left(1 - p_1^{-1}\right) \nabla^2 [c_o\, \rho(r) + \varepsilon_\pi\, c_1\, \delta\rho(r)]$$

$$+ \frac{1}{2}\left(1 - p_2^{-1}\right) \nabla^2 [C_o\, \rho^2(r)] \Big\} \qquad (2\text{-}55)$$

where

$$C(r) = p_1^{-1} [c_o\, \rho(r) + \varepsilon_\pi\, c_1\, \delta\rho(r)] + p_2^{-1}\, C_o\, \rho^2(r)\ ,$$

where it has been assumed that the p-wave absorption terms are modified by the LLEE effect. The inclusion of $C_o\, \rho^2$ in the LLEE effect complicates the analysis, since a change in C_o affects the p-wave strength of c_o, and vice-versa. In addition, some authors [Huf 75] believe it

should be kept separate. From the point of view of this analysis, the difference is a moot point since it only affects the final magnitude of parameters needed to produce the same scattering, and these parameters are not particularly well known. The tradeoffs that are required between these two alternatives have been given elsewhere [Str 79].

2.5 CALCULATIONS WITH FULL OPTICAL POTENTIAL

The properties of the full optical potential will be illustrated with the same series of calculations used in Section 2.3. However, the increased complexity of the potential increases the number of options we have for choosing optical parameter sets. One way of dealing with this complexity is to relate all of these potentials to an equivalent four-parameter potential, so that a common set of four effective strengths can be used to relate all of these potentials to each other. This will be done in the next section when these results are summarized.

Two sets of calculations will be focused on at low energy, reflecting varying degrees of adjustment in the parameters. The first, Set C, uses the phase shift values for $\bar{b}_o$, b_1, c_o, c_1 and the Chai and Riska values for B_o and C_o. We fix $\lambda = 1.6$ as listed in Table 2-3. This set is analogous to Set A and illustrates the effect of a purely theoretical model for the optical potential. The second, Set D, results when $\mathrm{Re}b_o$ and $\mathrm{Re}c_o$, and the amount of absorption (with $\mathrm{Im}B_o/\mathrm{Im}C_o$ held constant) are adjusted to fit the data in the same way as described earlier for Set B'. Three sets are used at 162 MeV. Set C is defined using the theoretical values for b_o, c_o, B_o, C_o as described above, with $\lambda=1$. Set D is the same except that $\mathrm{Re}c_o$ and $\mathrm{Im}C_o$ are fit to the data, in analogy to Set B. Set D' is also a fit, except the ∇^2 terms are omitted in analogy to Set B'. The results are given in Table 2-4.

Table 2-3

Parameter Set C, Multiple Scattering Theory
Values for the Second-Order Optical Potential

	π-Atom	50 MeV	162 MeV
$\bar{b}_o$	-0.033	-0.045 + 0.006 i	-0.083 + 0.029 i
b_1	-0.133	-0.131 - 0.002 i	-0.125 + 0.003
c_o	0.65	0.75 + 0.028 i	0.37 + 0.67 i
c_1	0.47	0.45 + 0.013 i	0.21 + 0.33 i
λ	1.6	1.6	1.0
B_o	0.007 +0.08 i	-0.02 + 0.14 i	-0.15 + 0.28
C_o	0.29 +0.34 i	0.36 + 0.59 i	1.29 + 2.95 i

Table 2-4

Parameter Sets D and D', Fitted Values for
Second-Order Optical Potential Described in the Text

	π-Atom	50 MeV	162 MeV	162 MeV (D')
$\bar{b}_o$	-0.0468	-0.060 +0.006 i	-0.083 +0.029 i	-0.083 +0.029 i
c_o	0.70	0.75 +0.028 i	0.45 +0.67 i	0.62 +0.67 i
λ	1.6	1.6	1.0	1.0
B_o	0.007 +0.19 i	-0.02 +0.12 i	-0.15 +0.28 i	-0.15 +0.28 i
C_o	0.29 +1.06 i	0.36 +0.66 i	1.29 +2.0 i	1.29 +2.1 i

These sets will be compared in the same way as in Section 2.3, starting with the pionic atom calculations shown in Figure 2-5. The dashed curve shows Set C, which does reasonably well but fails to get the details correct. The parameters of Set D were fit as described earlier, except that ImB_0 and ImC_0 were varied instead of Imb_0 and Imc_0. The results with Set D, shown with the solid curve, are quite similar to the results with Set B in Figure 2-2. This illustrates that the fit results are not particularly sensitive to the form of the potential. What is promising is that the values of the purely theoretical potential of Set C are now quite close to those required to fit the data. Indeed, some recent results [McM 81] suggest that p-wave medium corrections to $\bar{b}_0$ will increase its value to that required by the data. The absorption parameters are low, but the theoretical situation is far from clear. Recent work by Saraffian [Ris 80] indicates that medium corrections to the calculation of B_0 will bring agreement with the fit value in Set D. Calculations by Weise and coworkers [Ose 79] have produced values of ImC_0 that are much larger than those used in Set C. One set gave the value of $ImC_0 = 0.68$ fm^6, which is much closer to the number determined here. Their value of $ReC_0 = 0.97$ fm^6 would drastically change the result for c_0, reducing it to 0.60 fm^3. However, the value of λ significantly affects these predictions since all of the p-wave parameters are interrelated by the LLEE effect. It is large ambiguities like this that force us to fix on a single set and adjust it to the data, with the understanding that future theoretical work may clarify the exact values for different parts of the potential but will probably not alter the overall strength of the real and imaginary parts of the potential.

Figure 2-5

Pionic atom observables calculated with sets C (theory) and D, shown with dashed and solid curves, respectively.

MSUX-81-097

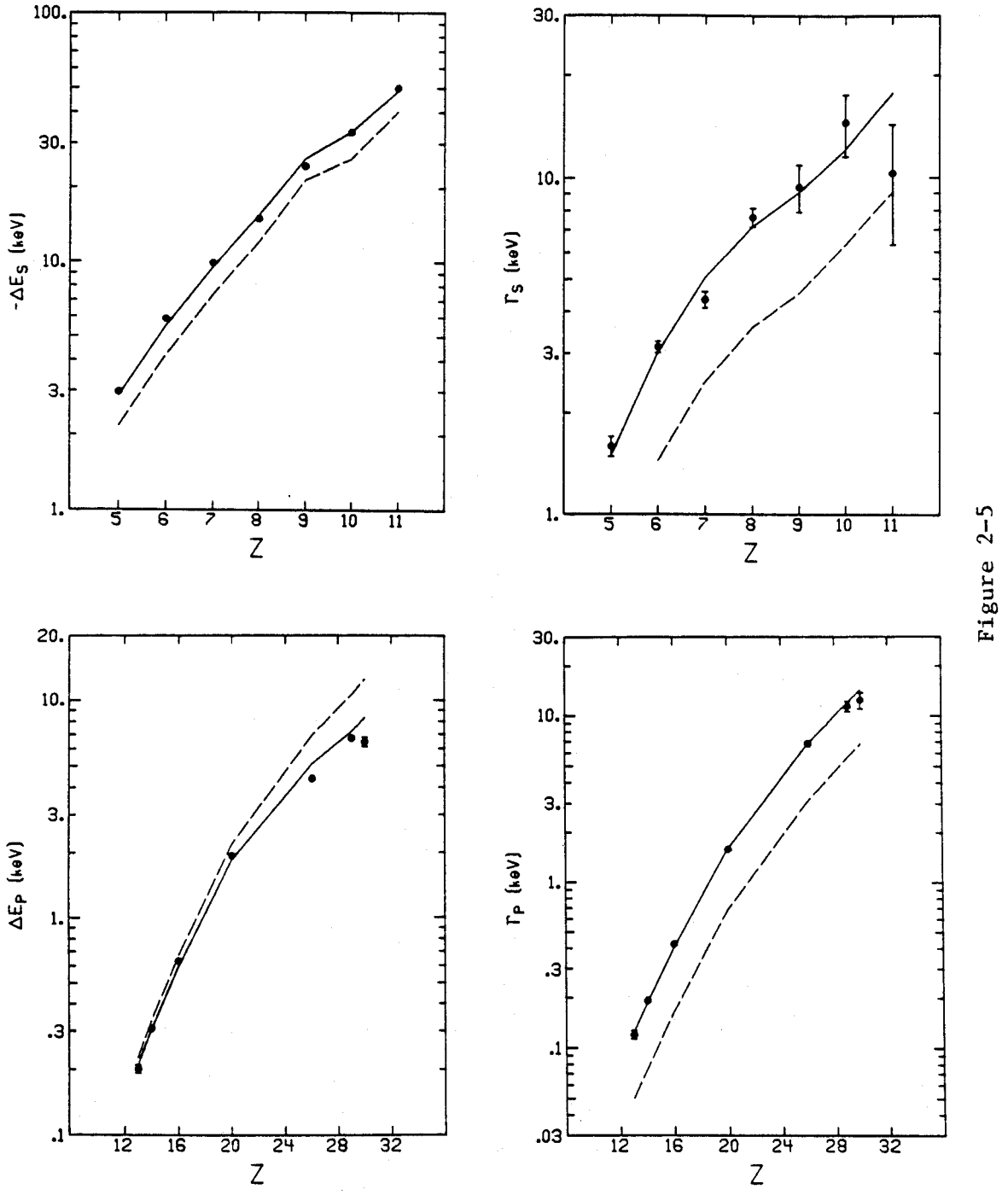

Figure 2-5

The conclusions about low energy elastic scattering are similar. As can be seen in Figure 2-6, the results with Set C (the dashed curve) are a big improvement over those with Set A in Figure 2-3. This is primarily due to the increase in s-wave repulsion due to the use of $\bar{b}_o$, and the decrease in the p-wave attraction due to the LLEE effect. The solid curves show the result of a fit, producing Set D. This is a three-parameter fit, with Reb_o, Rec_o and the absorption (ImB_o/ImC_o fixed) adjusted to fit the data in the same way as was done for Set B'. A comparison of sets C and D indicates that the change in $\bar{b}_o$ required is almost the same as for pionic atoms, -0.015 fm. The p-wave parameters agree very well, but this is mostly due to the deliberate choice of $\lambda = 1.6$.

It is particularly interesting to note that the absorption required is about 62% of the pionic atom values for Set D. The implication is that the absorption parameters decrease as energy increases, a result contrary to the predictions of all theories. However, calculations of absorption cross sections agree reasonably well with some recent absorption measurements [Car 81] if the absorption data [Nak 80] are systematically renormalized within the stated errors. Whether this correctly reflects the physical situation remains to be seen, as it will require additional experimental measurements.

The situation at higher energy is less clear. The results with Set C are shown with a dashed curve in Figure 2-6. The change from Set A is not very great; although differences at backward angles are significant, there is little data in this region. Set D is fit in the same way as Set B, with the same renormalizations of the data, and the

Figure 2-6

Elastic scattering calculated for 50 and 162 MeV π^+ using parameters from sets C, D and D', shown with dashed, solid and dash-dot curves, respectively.

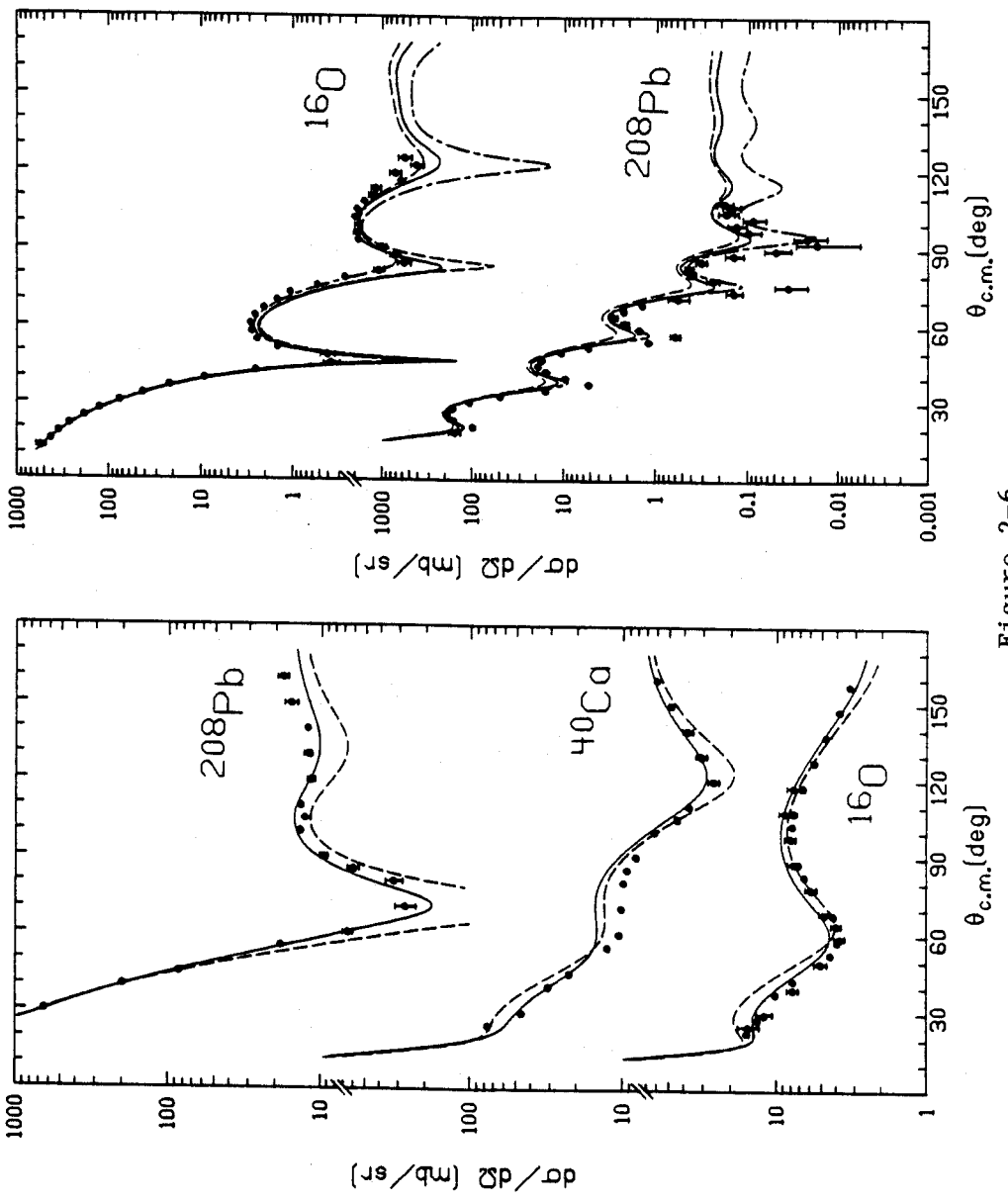

Figure 2-6

results are comparable. Removal of the ∇^2 term improves the fit, as Set D' (dash-dot curve) shows. The shift of the minimum is about the same as observed for Set B'. One reason that the calculations are similar is that the reactive content of the potentials is similar. Table 2-5 gives the reaction cross sections for these parameter sets. Although it is not always possible to decompose the reaction cross section into absorption and quasi-elastic cross sections, it is clear that the model used here produces reasonable values for the imaginary part of the optical potential.

A short summary of these results is that the increased s-wave repulsion ($\bar{b}_0$) and decreased p-wave attraction (LLEE effect) obtained from the second order corrections do much to improve agreement with the low energy data. Further, it is observed that absorption is important, contributing markedly to back-angle cross sections, and that it is possible to define absorption parameters which are consistent with the

Table 2-5

Reaction Cross Sections in mb for
162 MeV π^+ Elastic Scattering

	^{16}O	^{40}Ca	^{208}Pb
Set A	517	914	1955
Set B	510	899	1966
Set B'	510	901	1968
Set C	503	883	1930
Set D	509	893	1957
Set D'	507	894	1962

trend in σ_{abs} and $\sigma_{elastic}$ from zero to 50 MeV. The higher energy data are reasonably reproduced by all sets, although dropping the ∇^2 terms improves the fit. Both fitted sets have larger values of Rec_o and smaller values for ImC_o, as was observed for the sets B and B'.

2.6 SUMMARY OF ELASTIC SCATTERING RESULTS

The most straightforward way to compare these potentials is to formulate an "equivalent" potential so that changes in a few parameters can be related to the changes in the calculations. A convenient form is the simple Kisslinger form

$$2\bar{\omega}\, U = -4\pi\left[b_{eff}\ \rho(r) - c_{eff}\ \vec{\nabla}\cdot\ \rho(r)\ \vec{\nabla}\right] \qquad (2\text{-}56)$$

so that terms of higher order in ρ are incorporated into s-wave and p-wave strengths. We use a simple ansatz to define

$$b_{eff} = p_1 \bar{b}_o + p_2\ B_o\ \rho_{eff}$$

and (2-57)

$$c_{eff} = \frac{p_1^{-1}\ c_o + p_2^{-1}\ C_o\ \rho_{eff}}{1 + \frac{4\pi}{3}\lambda\left[p_1^{-1}\ c_o + p_2^{-1}\ C_o\ \rho_{eff}\right]\rho_{eff}}$$

where isovector terms are suppressed. This prescription does not produce a four-parameter potential that will generate exactly the same result as the full interaction; the density dependence cannot be replaced by a simple constant except within a small region of parameter space. Despite this restriction, the use of $\rho_{eff} \cong 0.7\ \rho_o = 0.12\ fm^{-3}$ provides a basis for a qualitative comparison [Str 80] of quite different potentials.

This form is particularly useful for interpreting the tradeoffs that occur between parameters. For example, the pionic atom data determined $ImB_o = 0.19$ for Set D, hence $ImB_o \rho_{eff} p_2/p_1 = 0.021$ which is only 30% greater than the fitted value for Imb_o in Set B. In a similar vein it was observed above that increasing ReC_o from 0.29 to 0.97 had to be compensated by a decrease of Rec_o from 0.70 to 0.61. Since the change in ReC_o translates into $(0.68)\ \rho_{eff}\ p_2/p_1 = 0.076$, we see that the simple model explains 80% of this change. The LLEE term is much more complicated, but implicit differentiation can be used to relate changes in λ to changes in the other parameters. For example, we can get

$$\frac{d\lambda}{d(Rec_o)} = \left(\frac{4\pi}{3} \rho_{eff}\ p_1 \left[\frac{c_o}{p_1} + \frac{C_o}{p_2}\ \rho_{eff} \right]^2 \right)^{-1} \qquad (2\text{-}58)$$

which is 3.7 for Set D at 50 MeV. This compares favorably with the value of $(1.4\text{-}1.6)/(0.70\text{-}0.75) = 4.0$ deduced from comparing this set to the best fit set with $\lambda = 1.4$ [Car 81]. These results serve to indicate how this equivalent potential provides a basis for a qualitative interpretation of the full potential in terms of a more easily understood four-parameter potential.

In summary, the simple four-parameter potential with IA fails miserably at low energy. The s-wave repulsion (Reb_{eff}) must be increased while the p-wave attraction (Rec_{eff}) is reduced. Also, there must be a large amount of absorption added, although the distribution between s- and p-wave is not clear. The results with IA values in the full potential outlined in Section 2.4 are much improved. This occurs since the second order corrections all go in the direction required by

the data. The use of $\bar{b}_o$ increases the repulsion in Reb_{eff}, while the LLEE effect substantially reduces Rec_{eff}. Fits indicate that only small adjustments are required to remove the remaining discrepancies. The calculated absorption is still too small for π-Atoms, although reasonable at 50 MeV. It remains to be seen if the 60% decrease in the absorption parameters from zero to 50 MeV can be explained theoretically, it is clearly required by the data.

The higher energy results were that the simple four-parameter potential is reasonable, but is improved by using p-wave parameters that correspond to a shift of the resonance by 20-30 MeV. The full potential gives better results to begin with, but is also improved by a similar adjustment in the p-wave parameters. Omitting the ∇^2 kinematic term makes the nucleus appear smaller, improving the fit to the low angle data, but decreasing the cross section at larger angles. If one is willing to adjust the size of the nuclear density [Olm 80], a similar improvement in the fit would also result. More complete studies will be needed to sort out these differences.

In summary, we have obtained four potentials that reflect varying degrees of theoretical sophistication and phenomenological input. Each is suitable for the exact calculation of the distorted waves needed for the inelastic scattering calculations, allowing investigation of the sensitivity of inelastic scattering to the distorted waves used. Further, they provide reference values for the pion-nucleon interaction that will generate the inelastic transition, allowing a test of whether inelastic scattering is as sensitive to second-order corrections in the interaction as elastic scattering is.

CHAPTER 3

INELASTIC SCATTERING FORMALISM

The analysis of inelastic pion-nucleus scattering usually makes use of the Distorted Wave Born Approximation (DWBA), based on the assumption that this is a direct reaction process involving the excitation of a single nuclear state without the involvement of other reaction channels. There are transitions for which this assumption is not valid; they should be analyzed in the Coupled Channels Born Approximation (CCBA) which we are not investigating here. This introduces an ambiguity into the analysis of some states which will be pointed out when appropriate.

This chapter will detail the theory and equations necessary for the analysis of inelastic pion scattering. First, the formal theory of the DWBA will be outlined. The expressions for the transition matrix are worked out, relating the cross section to matrix elements of the pion-nucleon interaction. These matrix elements are then worked out, separating terms involving the pion-nucleus interaction and nuclear structure, which include the "physics" of the process being studied, from angular momentum factors that reflect the rotational properties of space. The formulae of angular momentum algebra follow the conventions of Brink and Satchler [Bri 75] with the exception of the notation for the Clebsch-Gordon coefficient, which is given in Table 1-1. Finally, the details of the form factor are presented for the specific models considered here.

3.1 OVERVIEW OF SCATTERING THEORY AND THE DWBA

The DWBA has its origins in the Gell-Mann-Goldberger [Gel 53] relation for scattering from two potentials. The details of the formal theory of scattering used in deriving this result will not be given here, as they can be found in many places [Gol 64, Aus 70, Jac 75, Sat 64, Sch 68]. However, a summary is presented here for completeness. In Chapter 2 it was shown how the cross section was related to the transition matrix T, which satisfies the Lippman-Schwinger equation

$$T = V + VGT \quad . \tag{3-1}$$

The expansion of this gives

$$T = V + VGV + VGVGV + \cdots \tag{3-2}$$

which is recognized as the Born series for T. If we keep only the first term of this series, which corresponds to taking the first term of the series for $\Omega = 1 + GT$, we obtain the Plane Wave Born Approximation (PWBA). This gets its name from the fact that

$$T = \langle \phi_a | V | \phi_b \rangle \quad . \tag{3-3}$$

Although simple, this approach fails when V is strong, so that the series in equation (3-2) does not converge quickly, if at all.

The Gell-Mann-Goldberger relation provides a way around this problem when the potential can be broken into two parts, $V = V_0 + V_1$, where $V_0 << V_1$ and is known so that scattering by V_0 can be calculated exactly.

We define

$$T_o = V_o + V_o G T_o$$

and

$$\Omega_o = 1 + G T_o \tag{3-4}$$

for scattering from the potential V_o. Then the expression for T becomes

$$\begin{aligned} T &= (1 + T_o G)^{-1} T_o + V_1 + (1 + T_o G)^{-1} T_o + V_1 G T \\ &= T_o + (1 + T_o G) V_1 (1 + G T) \\ &= T_o + \hat{\Omega}_o V_1 \Omega \end{aligned} \tag{3-5}$$

where $\hat{\Omega}_o = 1 + T_o G$ is the time-reversed (incoming) solution corresponding to Ω_o. This relation is <u>exact</u> and involves no approximations. However, it still involves the unknown scattered wave Ω, so we still have an integral equation for T analogous to that defined in equation (3-1).

If we expand out Ω we obtain that

$$\Omega = \Omega_o + G V_o (\Omega - \Omega_o) + G V_1 \Omega \ . \tag{3-6}$$

Under the condition that $V_o >> V_1$, Ω will be well approximated by Ω_o and we can drop the higher order terms in equation (3-6). Then we get

$$T = T_o + \hat{\Omega}_o V_1 \Omega_o \tag{3-7}$$

which defines the Distorted Wave Born Approximation (DWBA). Since Ω_o includes the effects of V_o (the stronger part of the total potential V)

to all orders, this is a much better approximation than the PWBA defined by equation (3-3).

For our applications to inelastic scattering, V_o is chosen to be the elastic scattering part of V, so that V_1 then includes the interaction that excites the inelastic transition of interest. We can identify V_o with the U_o obtained in Chapter 2 since they both satisfy the same integral equation (2-16 or 3-4). Since T_o does not contribute to inelastic scattering, the formula for T simplifies to be

$$T_{ab} = \left\langle \phi_b \hat{\Omega}_o \middle| V_1 \middle| \Omega_o \phi_a \right\rangle = \left\langle \chi_b \middle| V_1 \middle| \chi_a \right\rangle \qquad (3\text{-}8)$$

where $\chi_a = \Omega_o \phi_a$ is the elastically scattered distorted wave which is the solution to the Hamiltonian $H_o + V_o$.

At this point it is easy to identify three limitations on the calculations performed this way that are essentially beyond our control. (i) The optical potential used for V_o is necessarily approximate since the elastic scattering of pions is not fully understood. It is presumed here that the choice is reasonable if the elastic scattering is fit by V_o. This will be examined in later chapters. (ii) The interaction V_1 is not completely known, and we will include only the most important terms that should contribute to inelastic scattering. (iii) The assumption that V_1 is small may not be satisfied, particularly in the case where coupled channels effects may be important. With these caveats in mind, we can now proceed to the evaluation of the formulae that are realized in the scattering program MSUDWPI [Carr] for use in performing the calculation which will appear later in this thesis.

3.2 REDUCTION OF THE CROSS SECTION FORMULA

The T-matrix is defined in DWBA [Aus 70] as

$$T^{DW} = \mathcal{J} \int d\vec{r}_i^{\,3} \int d\vec{r}_f^{\,3} \;\; \chi_f^{(-)*}(\vec{r}_f) \left\langle f \left| V_1 \right| i \right\rangle \; \chi_i^{(+)}(\vec{r}_i) \qquad (3\text{-}9)$$

where $\mathcal{J}$ is the Jacobian for the transformation to relative coordinates (omitted from here on) and where $\left\langle f \left| V_1 \right| i \right\rangle = \left\langle \Psi_f \, \phi_f \left| V - V_o \right| \Psi_i \, \phi_i \right\rangle$ is integrated over the internal coordinates of the scattered particle wave function (Ψ) and the nuclear state wave function (ϕ). This leaves $\left\langle I'M' \left| V_1 \right| IM \right\rangle$ where I, M (I'M') and the initial (final) state spin and Z-projection. After a partial wave decomposition we obtain

$$T^{DW} = \sum_{\substack{\ell m \\ \ell' m'}} \iint \chi_{f\,\ell' m'}^{(-)*}(\vec{r}') \; Y_{\ell' m'}(\hat{k}_f)$$

$$x \left\langle I'M' \left| V_1 \right| IM \right\rangle \; \chi_{i\,\ell m}^{(+)}(\vec{r}) \; Y_{\ell m}^{*}(\hat{k}_i) \; d\vec{r}^{\,3} \, d\vec{r}^{\,3\prime} \qquad (3\text{-}10)$$

where $\chi_{\ell m}(\vec{r}) = i^{\ell} \; (4\pi) \left[u_\ell(r)/r \right] Y_{\ell m}(\hat{r})$ and where $u_\ell(r)$ has the normalization that

$$\lim_{r \to \infty} u_\ell(r) = \frac{1}{k} \sin \left(kr - \frac{\ell\pi}{2} - \eta \ln(2kr) + \delta_\ell + \sigma_\ell \right) e^{i\delta_\ell} \; . \qquad (3\text{-}11)$$

The formula (3-10) can be rewritten to give

$$T^{DW} = \sum_{\substack{\ell m \\ \ell' m'}} \sum_{JM_J} \left\langle \ell' m' \; I'M' \left| JM_J \right\rangle \right\langle \ell m \; IM \left| JM_J \right\rangle \; Y_{\ell' m'}(\hat{k}_f) \; Y_{\ell m}^{*}(\hat{k}_i)$$

$$x \iint \left\langle \left[\chi_{\ell'}(\vec{r}') \times I' \right]^{JM_J} \left| V_1 \right| \left[\chi_\ell(\vec{r}) \times I \right]^{JM_J} \right\rangle d\vec{r}^{\,3} \, d\vec{r}^{\,3\prime} \qquad (3\text{-}12)$$

We define a transition-matrix element

$$T^{J*}_{\ell I \ell' I'} = \iint \left\langle [\ell' \times I']^{JM_J} \middle| V_1 \middle| [\ell \times I]^{JM_J} \right\rangle d^3r\, d^3r' \qquad (3\text{-}13)$$

where the quantum number M_J is not included in the definition of $T^J_{\ell I \ell' I'}$ since, as will be shown in equation (3-41) of the next section, this matrix element is independent of M_J. Note in particular that it is the complex conjugate of T that is defined here. This is done to be compatible with the definitions used in the original version of DWPI.

The expression for the cross section is

$$\frac{d\sigma}{d\Omega} = \left(\frac{\bar{\omega}}{2\pi \hbar^2} \right)^2 \frac{k_f}{k_i} \frac{1}{(2I+1)} \sum_{\substack{M_i \\ M_f}} \left| T^{DW} \right|^2 \qquad (3\text{-}14)$$

where the extra factors of k account for differences in the flux definition in the two channels and the sum does the average over initial and sum over final spin projections required for the unpolarized cross section. Using the definitions in equations (3-12) and (3-13), we obtain that

$$\sum_{MM'} T\, T^*_1 = \sum_{MM'} \sum_{\substack{\ell m \\ \ell' m'}} \sum_{JM_J} \sum_{\substack{\ell_1 m_1 \\ \ell_1' m_1'}} \sum_{J_1 M_{J_1}} T^{J*}_{\ell I \ell' I'}\; T^{J_1}_{\ell_1 I \ell_1' I'}$$

$$\times \left\langle \ell m\ IM \middle| JM_J \right\rangle \left\langle \ell' m'\ I'M' \middle| JM_J \right\rangle \left\langle \ell_1 m_1\ IM \middle| J_1 M_{J_1} \right\rangle \qquad (3\text{-}15)$$

$$\times \left\langle \ell'_1 m'_1 I'M' \middle| J_1 M_{J_1} \right\rangle Y^*_{\ell m}(\hat{k}_i)\, Y_{\ell' m'}(\hat{k}_f)\, Y_{\ell_1 m_1}(\hat{k}_i)\, Y^*_{\ell_1' m_1'}(\hat{k}_f)$$

This can be separated into two pieces. We first use the sum or M(M') to simplify the clebsches using triangular relations. Then the first piece is

$$\sum_{mm_1} \langle \ell m \; I \; M_J - m | JM_J \rangle \langle \ell_1 m_1 \; I \; M_{J_1} - m | J_1 M_{J_1} \rangle Y^*_{\ell m}(\hat{k}_i) \; Y_{\ell_1 m_1}(\hat{k}_i) \tag{3-16}$$

Using that $Y^*_{\ell m} = Y_{\ell -m}(-)^m$ and then redefining m in the sum we get

$$\sum_{mm_1} \langle \ell -m \; I \; M_J + m | JM_J \rangle \langle \ell_1 m_1 \; I \; M_{J_1} - m_1 | J_1 M_{J_1} \rangle (-)^m \; Y_{\ell m}(\hat{k}_i) \; Y_{\ell_1 m_1}(\hat{k}_i) \tag{3-17}$$

These two clebsches can be rewritten using

$$\langle \ell -m \; I \; M_J + m | JM_J \rangle = \frac{\hat{J}}{\hat{I}} (-)^{J-I+m} \langle \ell m \; JM_J | I \; M_J + m \rangle$$

and

$$\langle \ell_1 m_1 \; I \; M_{J_1} - m_1 | J_1 M_{J_1} \rangle = \frac{\hat{J}_1}{\hat{\ell}_1} (-)^{2I+\ell_1 - J_1 + M_{J_1} - m_1} \langle I \; M_{J_1} - m_1 J_1 - M_{J_1} | \ell_1 \; m_1 \rangle . \tag{3-18}$$

Since

$$\langle \ell m \; JM_j | I \; M_J + m \rangle \langle I \; M_{J_1} - m_1 \; J_1 - M_{J_1} | \ell_1 - m_1 \rangle$$

$$= \sum_L \langle JM_J \; J_1 - M_{J_1} | L \; M_J - M_{J_1} \rangle \langle \ell m \; L - (m+m_1) | \ell_1 - m_1 \rangle$$

$$x \; \hat{I}\hat{L} \; W(\ell J \ell_1 J_1 ; \; IL) \; (-)^{J+\ell_1 - I - L} \; W(\ell L \; IJ_1 ; \; \ell_1 J) \quad , \tag{3-19}$$

we obtain the result that equation (3-17) is now

$$\sum_L \sum_{mm_1} \frac{\hat{J} \; \hat{J}_1 \; \hat{L}}{\hat{\ell}_1} (-)^{2J - J_1 - L + M_{J_1} - m_1} \; Y_{\ell m}(\hat{k}_i) \; Y_{\ell_1 m_1}(\hat{k}_i)$$

$$x \langle JM_J \; J_1 - M_{J_1} | L \; M_J - M_{J_1} \rangle \langle \ell m \; L - (M+m_1) | \ell_1 - m_1 \rangle \; W(\ell L \; IJ_1 ; \; \ell_1 J) \quad . \tag{3-20}$$

Since

$$\left\langle \ell m\ L{-}(m_1{+}m) \middle| \ell_1 {-}m_1 \right\rangle = \frac{\hat{\ell}_1}{\hat{L}} (-)^{\ell-m} \left\langle \ell m\ \ell_1 m_1 \middle| L\ m{+}m_1 \right\rangle \quad , \tag{3-21}$$

we can write equation (3-20) as

$$\sum_L \hat{J}\ \hat{J}_1 (-)^{2J-J_1+\ell-L+M_{J_1}} W(\ell L\ IJ_1;\ \ell_1 J) \left\langle JM_J\ J_1 {-}M_{J_1} \middle| L\ M_J {-}M_{J_1} \right\rangle$$

$$\times \sum_{m_1 m} (-)^{m+m_1} \left\langle \ell m\ \ell_1 m_1 \middle| L\ m{+}m_1 \right\rangle Y_{\ell m}(\hat{k}_i)\ Y_{\ell_1 m_1}(\hat{k}_i) \quad . \tag{3-22}$$

We can now use the result that

$$\sum_{m m_1} \left\langle \ell m\ \ell_1 m_1 \middle| LM \right\rangle Y_{\ell m}(\hat{k})\ Y_{\ell_1 m_1}(\hat{k})$$

$$= \frac{\hat{\ell}\hat{\ell}_1}{\sqrt{4\pi}\,\hat{L}} (-)^M Y_{LM}(\hat{k}) \left\langle (\ell 0\ \ell_1 0 \middle| L0) \right\rangle \tag{3-23}$$

when $M = m_1 + m_2$ is held fixed. Since M is not fixed in the sum above, we get a sum on M and the final result for equation (3-16) is given by

$$\sum_{LM} \frac{\hat{J}\ \hat{J}_1\ \hat{\ell}\hat{\ell}_1}{\sqrt{4\pi}\,\hat{L}} (-)^{2J-J_1+\ell-L+M_{J_1}} W(\ell L\ IJ_1;\ \ell_1 J)$$

$$\times \left\langle JM_J\ J_1 {-}M_{J_1} \middle| LM \right\rangle \left\langle \ell 0\ \ell_1 0 \middle| L0 \right\rangle\ Y_{LM}(\hat{k}_i) \tag{3-24}$$

The second factor that we can remove from equation (3-15) is

$$\sum_{\ell m' m_1'} \left\langle \ell' m' \; I' M_J - m' \middle| J M_J \right\rangle$$

$$\times \left\langle \ell_1' m_1' \; I' M_{J_1} - m_1' \middle| J_1 M_{J_1} \right\rangle Y_{\ell' m'}(\hat{k}_f) \; Y^*_{\ell_1' m_1'}(\hat{k}_f) \tag{3-25}$$

In a derivation that follows the same pattern as we used for equation (3-16), we rewrite this using

$$Y_{\ell' m'}(\hat{k}) = (-)^{m'} \; Y^*_{\ell' -m'}(\hat{k})$$

and reorder the clebsches. When the clebsches are combined into a Racah coefficient we get

$$\sum_L \sum_{m \, m_1} \frac{\hat{J} \, \hat{J}_1 \, \hat{L}'}{\hat{\ell}_1} (-)^{2J + J_1 - L' + M_{J_1} - m_1'} W(\ell' L' \; I' J_1 ; \; \ell_1 J)$$

$$\times \left\langle J M_J \; J_1 - M_{J_1} \middle| L' \; M_J - M_{J_1} \right\rangle \left\langle \ell' m' L' \; - (M' + m_1) \middle| \ell_1' - m_1' \right\rangle Y^*_{\ell' m'}(\hat{k}) \; Y_{\ell_1' m_1'}(\hat{k}) \tag{3-26}$$

which is analogous to equation (3-20). Then the sum on m and m_1 is used to obtain

$$\sum_{L' M'} \frac{\hat{J} \, \hat{J}_1 \hat{\ell}' \hat{\ell}_1'}{\sqrt{4\pi} \, \hat{L}'} (-)^{2J + J_1 - L' + \ell' + M_{J_1}} W(\ell' L' I' J_1 ; \; \ell_1 J)$$

$$\times \left\langle J M_J \; J_1 - M_{J_1} \middle| L' M' \right\rangle \left\langle \ell' 0 \; \ell_1 0 \middle| L' 0 \right\rangle Y^*_{L' M'}(\hat{k}_f) \tag{3-27}$$

for the equation (3-25) parts of equation (3-15). These terms can now be inserted into equation (3-15) which becomes

$$\sum_{mm'} |T|^2 = \sum_{\substack{\ell\ell' \\ LM}} \sum_{\substack{\ell_1\ell_1' \\ L'M'}} \sum_{\substack{J\,M_J \\ J_1 M_{J_1}}} \frac{\hat{J}^2\hat{J}_1^2\ \hat{\ell}\hat{\ell}'\ \hat{\ell}_1\hat{\ell}_1'}{\sqrt{4\pi}\,\hat{L}\,\hat{L}'}\ Y_{LM}(\hat{k}_i)\ Y^*_{L'M'}(\hat{k}_f)$$

$$\times \left\langle \ell 0\, \ell_1 0 \middle| L0 \right\rangle \left\langle \ell' 0\, \ell_1' 0 \middle| L'0 \right\rangle W(\ell L\ I J_1;\ \ell_1 J)$$

$$\times W(\ell' L'\ I' J_1;\ \ell_1' J) \left\langle J M_J\ J_1 - M_{J_1} \middle| LM \right\rangle \left\langle J M_J\ J_1 - M_{J_1} \middle| L'M' \right\rangle$$

$$(-)^{\ell+\ell'-L-L'}\ T^{J*}_{\ell I \ell' I'}\ T^{J_1}_{\ell_1 I \ell_1' I'} \quad . \tag{3-28}$$

We now use that

$$\sum_{M_J M_{J_1}} \left\langle J M_J\ J_1 - M_{J_1} \middle| LM \right\rangle \left\langle J M_J\ J_1 - M_{J_1} \middle| L'M' \right\rangle = \delta_{LL'}\ \delta_{MM'}\ ,$$

$$\left\langle \ell 0\ \ell_1 0 \middle| L0 \right\rangle = \frac{\hat{L}}{\hat{\ell}_1} (-)^{\ell} \left\langle \ell 0\ L0 \middle| \ell_1 0 \right\rangle ,$$

$$\left\langle \ell' 0\ \ell_1' 0 \middle| L0 \right\rangle = \frac{\hat{L}}{\hat{\ell}'_1} (-)^{\ell'} \left\langle \ell' 0\ L0 \middle| \ell_1' 0 \right\rangle ,$$

and

$$\sum_{M} Y_{LM}(\hat{k}_i)\ Y^*_{LM}(\hat{k}_f) = \frac{\hat{L}^2}{4\pi} P_L(\cos\ \theta) \ ,$$

where θ is the (scattering) angle between $\vec{k}_f$ and $\vec{k}_i$, to reduce equation (3-28) to

$$\sum_{mm'} \left|T\right|^2 = \sum_{L} \sum_{\substack{\ell\ell' \\ \ell_1\ell_1'}} \sum_{\substack{J \\ J_1}} \frac{\hat{J}^2 \hat{J}_1^2 \hat{L}^2 \hat{\ell}\hat{\ell}'}{(4\pi)^2} \left\langle \ell 0\ L0 \middle| \ell_1 0 \right\rangle \left\langle \ell' 0\ L0 \middle| \ell_1 0 \right\rangle$$

$$\times W(\ell L\ IJ_1;\ \ell_1 J)\ W(\ell' L'\ I' J_1;\ \ell_1' J)\ T^{J*}_{\ell I \ell' I'}\ T^{J_1}_{\ell_1 I \ell_1' I'}\ P_L(\cos\theta)$$

$$= \frac{1}{(4\pi)^2} \sum_{L} \sigma_L\ P_L(\cos\theta) \qquad (3\text{-}29)$$

This final equation defines the quantity σ_L, which allows a compact expression for the cross section,

$$\frac{d\sigma}{d\Omega} = \left(\frac{\bar{\omega}}{2\pi \hbar^2} \right)^2 \frac{k_f}{k_i} \frac{1}{(2I+1)} \frac{1}{(4\pi)^2} \sum_{L} \sigma_L\ P_L(\cos\theta) \quad . \qquad (3\text{-}30)$$

Although this is a correct result, a correction must be made in the formula to make contact with the assumptions included in the program DWPI. The wave functions calculated by the program [Eis 76] are normalized so that

$$\chi_{\ell m}(\vec{r}) = i^{\ell} \frac{u_\ell(r)}{r}\ Y_{\ell m}(\hat{r})$$

and (3-31)

$$\lim_{r\to\infty} u_\ell(r) = \frac{1}{\hbar c}\ \sqrt{\frac{2\bar{\omega}}{\pi k}} \sin\left(kr - \frac{\ell\pi}{2} - \eta \ln(2kr) + \delta_\ell + \sigma_\ell \right) e^{i\delta_\ell}$$

rather than as given in equation (3-11). In order to convert equation (3-30) to this normalization, a factor of

$$\frac{k}{4\pi} \frac{1}{\hbar c}\ \sqrt{\frac{2\bar{\omega}}{\pi k}} = \frac{1}{\hbar c} \sqrt{\frac{k\bar{\omega}}{8\pi^3}}$$

must be absorbed into the $T^J_{\ell I \ell' I}$ for each of the four wave functions. If we remove this factor of

$$\frac{k_i\ k_f\ \bar{\omega}^2}{64\ \pi^6\ \hbar^4}$$

from the factors in equation (3-30) and include it in the wave function normalization, we are left with

$$\frac{d\sigma}{d\Omega} = \frac{\pi^2}{k_i^2(2I+1)} \sum_L \sigma_L\ P_L(\cos\ \theta) \quad . \tag{3-32}$$

This is used in the main program of DWPI to calculate the cross sections from the matrix elements, which are described in the next section.

3.3 EXPANSION OF THE TRANSITION MATRIX ELEMENTS

The matrix element defined in equation (3-13) is

$$T^J_{\ell I \ell' I'} = \iint \left\langle (\ell \otimes I)^{JM_J} \middle| V_1 \middle| (\ell' \otimes I')^{JM_J} \right\rangle\ d\vec{r}^3\ d\vec{r}'^3 \tag{3-33}$$

where

$$V_1 = At_{\pi N} \sum_{\lambda\mu}\ T_{\lambda 0 \lambda,\mu}(r)\ Y_{\lambda\mu}(\hat{r}) \tag{3-34}$$

for natural parity (S=0) transitions. Equation (3-33) can be expanded to give

$$T^J_{\ell I \ell' I'} = \sum_{\substack{mM \\ m'M'}} \left\langle \ell m\ IM \middle| JM_J \right\rangle \left\langle \ell' m'\ I'M' \middle| JM_J \right\rangle \tag{3-35}$$

$$\times \iint \sum_{\lambda\mu} \left\langle \chi_{\ell m} \middle|\ At_{\pi N}\ \left\langle IM \middle| T_{\lambda 0 \lambda,\mu} \middle| I'M' \right\rangle\ Y_{\lambda\mu} \middle| \chi_{\ell' m'} \right\rangle\ d\vec{r}^3\ d\vec{r}'^3$$

The second half of this equation can be further simplified to give

$$\sum_{\lambda\mu}\left\langle \ell m\ Y_{\lambda\mu}\middle|\ell' m'\right\rangle \ \frac{i^{-\ell}\ u_{\ell}^{(-)*}(r)}{r}\ At_{\pi N}\left\langle IM\middle|T_{\lambda 0\lambda,\mu}\middle|I'M'\right\rangle \frac{i^{\ell'}\ u_{\ell'}^{(+)}(r)}{r} \tag{3-36}$$

where the fact that the angular integral can be brought through $t_{\pi N}$ for the interactions used here is proven in Appendix D.

At this point it is convenient to define a new operator

$$\bar{T}_{\lambda 0\lambda,-\mu} = (-)^{\mu}\ T_{\lambda 0\lambda,\mu} \tag{3-37}$$

Then equation (3-36) becomes

$$\sum_{\lambda\mu}\ (-)^{\mu}\left\langle \ell' m'\ \lambda\mu\middle|\ell m\right\rangle\ \left\langle I'M'\ \lambda\ -\ \mu\middle|IM\right\rangle\ \left\langle \ell\middle\|\ Y_{\lambda}\middle\|\ \ell'\right\rangle \tag{3-38}$$

$$\int x\ \frac{i^{-\ell}\ u_{\ell}^{(-)*}(r)}{r}\ \left[At_{\pi N}\left\langle I\middle\|\ \bar{T}_{\lambda 0\lambda}\middle\|\ I'\right\rangle\right]\ \frac{i^{\ell'}\ u_{\ell'}^{(+)}(r)}{r}\ r^2\ dr$$

and equation (3-35) then includes a sum on four clebsches

$$\sum_{\mu}\ \sum_{\substack{mM\\ m'M'}}(-)^{\mu}\left\langle \ell m\ IM\ JM_J\right\rangle\ \left\langle \ell' m'\ I'M'\ JM_J\right\rangle \tag{3-39}$$

$$\left\langle \ell' m'\ \lambda\mu\middle|\ell M\right\rangle\ \left\langle I'M'\ \lambda\ -\ \mu\middle|IM\right\rangle$$

in addition to the integral and the reduced matrix elements. The sum in equation (3-39) can be reduced to a single Racah coefficient. The procedure is to rewrite

$$\left\langle I'M'\ \lambda\ -\ \mu\middle|\ IM\right\rangle = \frac{\hat{I}}{\hat{I}'}\ (-)^{\lambda-\mu}\ \left\langle \lambda\mu\ IM\middle|I'M'\right\rangle$$

and use the sums on m, M and M' to satisfy the triangular conditions so equation (3-39) becomes, for fixed M_J,

$$\frac{\hat{I}}{\hat{I}'}(-)^{\lambda}\sum_{m'}\left\langle \ell' m' \lambda\mu \middle| \ell\ m'+\mu\right\rangle \left\langle \ell m'+\mu\ I M_J \middle| JM_J\right\rangle$$

$$\left\langle \lambda\mu\ I\ M_J-m'-\mu \middle| I' M_J-m'\right\rangle \left\langle \ell' m'\ I'\ M_J-m' \middle| JM_J\right\rangle$$

$$= \frac{\hat{I}}{\hat{I}'}(-)^{\lambda}\,\hat{\ell}\hat{I}'\,W(\ell'\lambda\ JI;\ \ell I')$$

$$= \hat{I}\hat{\ell}\,(-)^{J-\ell-I}\ W(\ell\ell'\ II';\ \lambda J) \tag{3-40}$$

which is independent of M_J. Substituting this into equation (3-35) gives

$$T^J_{\ell I \ell' I'} = \sum_{\lambda}\hat{\ell}\hat{I}\,(-)^{J-\ell-I}\,W(\ell\ell'\ II';\ \lambda J)\left\langle \ell \middle\| Y_\lambda \middle\| \ell'\right\rangle$$

$$\times\int \frac{i^{-\ell}\ (-)^{*}\ u_\ell(r)}{r}\,At_{\pi N}\left\langle I\middle\| \bar{T}_{\lambda 0\lambda}\middle\| I'\right\rangle \frac{i^{\ell'}\ (+)\ u_{\ell'}(r)}{r}\,r^2\,dr\ . \tag{3-41}$$

The final step is to evaluate the reduced matrix element and put the equations into a standard form. First we use

$$\left\langle \ell \middle\| Y_\lambda \middle\| \ell'\right\rangle = (4\pi)^{-1/2}\,(-)^{\lambda}\hat{\lambda}\left\langle \ell 0\ \lambda 0 \middle| \ell 0\right\rangle$$

and

$$\left\langle I\middle\| \bar{T}_{\lambda 0\lambda}\middle\| I'\right\rangle = \frac{\hat{I}'}{\hat{I}}(-)^{I-I'}\left\langle I'\middle\| \bar{T}_{\lambda 0\lambda}\middle\| I\right\rangle$$

and

$$u_\ell^{(+)}(r) = u_\ell^{(-)*}(r)$$

to get

$$T^J_{\ell I \ell' I'} = (4\pi)^{-1/2} \sum_\lambda (-)^{J+2I+I'} \hat{I}' \, W(I'\ell' \, I\ell; \, J\lambda)$$
$$\times (-)^{\ell} \, i^{\ell'-\ell} \left\langle \ell 0 \; \lambda 0 \middle| \ell' 0 \right\rangle (-)^{\lambda-I+I'}$$
$$\times \int \frac{u^{(-)*}_{\ell'}(r)}{r} \left[At_{\pi N} \left\langle I' \middle\| \bar{T}_{\lambda 0 \lambda} \middle\| I \right\rangle \right] \frac{u^{(+)}_{\ell}(r)}{r} \, r^2 \, dr \quad . \qquad (3\text{-}42)$$

This can be more conveniently written as

$$T^J_{\ell I \ell' I'} = (4\pi)^{-1/2} \sum_\lambda (-)^{J+2I+I'} \hat{I}' \, W(I'\ell' \, I\ell; \, J\lambda) \, F_{\ell\ell'\lambda}$$

where

$$F_{\ell\ell'\lambda} = (-)^{\ell} \, i^{\ell'-\ell} \, \hat{\ell} \left\langle \ell 0 \; \lambda 0 \middle| \ell' 0 \right\rangle (-)^{\lambda-I+I'} \, \hat{\lambda}$$

(3-43)

$$\times \int \frac{u^{*}_{\ell'}}{r} \, \bar{F}_\lambda(r) \, \frac{u_\ell}{r} \, r^2 \, dr$$

and

$$\bar{F}_\lambda(r) = At_{\pi N} \left\langle I' \middle\| \bar{T}_{\lambda 0 \lambda} \middle\| I \right\rangle \quad .$$

Thus we have an expression for $T^J_{\ell I \ell' I'}$ that separates the rotational properties of the matrix elements from the physics contained in $t_{\pi N}$ and $\left\langle I' \middle\| \bar{T}_{\lambda 0 \lambda} \middle\| I \right\rangle$. Although the formula written here is restricted to natural parity transitions, it is modified in a straightforward way for unnatural parity (S=1) transitions. These details, along with those for normal parity transitions, follow in the next sections.

3.4 EVALUATION OF THE FORM FACTOR FOR NATURAL PARITY TRANSITIONS

The form factor $\bar{F}_\lambda(r)$ defined in equation (3-43) can be evaluated for a number of different cases; we will examine only a few of them here. First, the transition density $\left\langle I' \left\| T_{LSJ} \right\| I \right\rangle$ will be evaluated in the collective and microscopic models. Then it will be shown how the Impulse Approximation (IA) form of $t_{\pi N}$, as defined in equation (2-43), can be used to form $\bar{F}_\lambda(r)$ in several different ways. Finally, an ansatz will be shown for including the second order terms of equation (2-55) in $\bar{F}_\lambda(r)$.

A collective model transition density is particularly convenient for comparison to scattering by other probes because of its common use and simple definition. However, its use is best limited to those (usually low lying) states in nuclei where rotational or vibrational degrees of freedom dominate. This model assumes the nucleus behaves like a quantized liquid drop where the surface is deformed from a spherical shape to

$$R(\theta,\phi) = R_o\left[1 + \sum_{LM} (-)^M \bar{\alpha}_{L-M} Y_{LM}(\theta,\phi)\right] \qquad (3\text{-}44)$$

where

$$\bar{\alpha}_{L-M} = (-)^M \alpha_{LM} = \beta_L \hat{L}^{-1}\left[b_{LM} + (-)^M b^+_{L-M}\right]$$

includes the operators b_{LM} (b^+_{LM}) which destroy (create) an excitation with angular momentum L and the amplitude of the excitation β_L. This

deformation produces a change in the density from a spherical form $\rho(r)$ to

$$\rho(r,\theta,\phi) = \rho(r) + \delta\rho$$

$$= \rho(r) - \sum_{LM} \alpha_{LM} R_o \frac{\partial\rho(r)}{\partial r} Y_{LM}(\theta,\phi) \tag{3-45}$$

in lowest order. This deformed part is assumed to give rise to the nuclear transition. In this case

$$\left\langle I' \left\| T_{JOJ} \right\| I \right\rangle = F_C(r) \left\langle I' \left\| \alpha_J \right\| I \right\rangle \tag{3-46}$$

where $F_C(r) = -R_o \, \partial\rho/\partial r$, since Y_J has already been factored out [see equation (3-34)]. This matrix element is evaluated by writing

$$\left\langle I' \left\| \bar{\alpha}_J \right\| I \right\rangle = \left\langle (JI)^{I'} \left\| \bar{\alpha}_J \right\| (OI)^{I} \right\rangle$$

$$= (-)^{I'-J-I} W(JO\ I'I;\ JI) \left\langle J \left\| \bar{\alpha}_J \right\| O \right\rangle$$

$$= (-)^{I'-J-I} \left\langle J \left\| \bar{\alpha}_J \right\| O \right\rangle \tag{3-47}$$

and then using

$$\left\langle J \left\| \bar{\alpha}_J \right\| O \right\rangle = \left\langle JM \left| \bar{\alpha}_{JM} \right| O \right\rangle$$

$$= (-)^M \left\langle JM \left| \alpha_{J-M} \right| O \right\rangle$$

$$= (-)^M \beta_J \hat{J}^{-1} \left\langle JM \left| b_{J-M} + (-)^M b^+_{JM} \right| O \right\rangle$$

$$= \beta_J \hat{J}^{-1} \left\langle JM \left| b^+_{JM} \right| O \right\rangle = \beta_J \hat{J}^{-1} \quad . \tag{3-48}$$

Combining these we obtain the result that

$$\bar{F}_\lambda(r) = At_{\pi N}\, F(r)\, \beta_\lambda\, \hat{\lambda}^{-1}\, (-)^{I'-\lambda-I} \tag{3-49}$$

for a collective model transition. Notice that use of this result in equation (3-43) gives us

$$F_{\ell\ell'\lambda} = \beta_\lambda\, (-)^{\ell}\, i^{\ell'-\ell}\hat{\ell}\, \left\langle \ell 0\ \lambda 0 \middle| \ell' 0 \right\rangle$$

$$\times \int \frac{u^*_{\ell'}}{r}\, At_{\pi N} \left(- R_o \frac{\partial \rho}{\partial r} \right) \frac{u_\ell}{r}\, r^2\, dr \tag{3-50}$$

which is the standard formula included in the original version of DWPI.

A microscopic model for the transition density has the advantage of allowing direct calculation of transitions between states which can be described by simple configurations in the nuclear shell model. The equations written here will be specialized to the case of transitions from a closed shell ground state to an excited state made up of a particle and a hole coupled to good J. Such a state can be written as

$$\left| JM \right\rangle = \sum_{ij} C_{ij} \sum_{\substack{m \\ m_{p_i} \\ m_{h_j}}} \left\langle j_{p_i}\, m_{p_i}\, j_{h_j}\, -m_{h_j} \middle| JM \right\rangle$$

$$\times (-)^{j_{h_j}-m_{h_j}}\, a^+_{p_i}\, a_{h_j} \left| C \right\rangle \tag{3-51}$$

since a hole state $\left| h_{jm} \right\rangle = (-)^{j-m}\, a_{jm} \left| C \right\rangle$ has quantum numbers j_h and $-m_{jh}$.

The C_{ij} can be obtained by diagonalizing a shell model Hamiltonian for the residual interaction between pairs of particle-hole states. The core C is assumed to be a filled shell. Such a process is known as the Tamm-Danckoff Approximation (TDA). A better approximation, one that accounts partially for the effects of ground state correlations, is the Random Phase Approximation (RPA). Here the ground state is assumed to include 2p-2h (and 4p-4h, etc.) components, so that a 1p-1h state can be reached by annihilating a particle-hole pair (with amplitude Y_{ij}) as well as by creating one (with amplitude X_{ij}). This case can be treated in exactly the same way, where we replace C_{ij} with $X_{ij} + (-)^S Y_{ij}$ [Pet 70].

What remains is to evaluate the reduced matrix elements of

$$T_{LSJ,M_J} = \sum_{M\lambda} \left\langle LM\ S\lambda \middle| JM_J \right\rangle Y_{LM}\ \sigma^S_\lambda\ , \tag{3-52}$$

where $\sigma^0 = 1$ and $\sigma^1 = \vec{\sigma}$, for a transition to the state in equation (3-51). Although only S=0 transfers are considered here, it is convenient to also do the S=1 transfer that will be used in Section 3.5. The particle-hole matrix element is

$$\left\langle I'M' \middle| T_{LSJ,M_J} \middle| 0 \right\rangle = \sum_{ij} \sum_{m_{p_i}} \sum_{m_{h_j}} C_{ij} \left\langle j_{p_i}\, m_{p_i}\ j_{h_j}\, -m_{h_j} \middle| JM_J \right\rangle$$

$$\times (-)^{j_{h_j} - m_{h_j}} \left\langle j_{p_i}\, m_{p_i} \middle| T_{LSJ,M_J} \middle| j_{h_j}\, m_{h_j} \right\rangle R_i(r)\ R_j(r)$$

$$= \sum_{ij} C_{ij} \frac{\hat{j}_{p_i}}{\hat{I}'} \left\langle j_{p_i} \middle\| T_{LSJ} \middle\| j_{h_j} \right\rangle \delta_{JI'}\ R_i(r)\ R_j(r)\ , \tag{3-53}$$

where $R_i(r)$ is the radial part of the shell model wave function. A convenient formula for these is

$$R_{n\ell}(r) = \pi^{-1/4}\left[\frac{2^{n+\ell+1}\,(n-1)!}{(2n+2\ell-1)!!}\right]^{1/2} \alpha^{3/2}\,(\alpha r)^{\ell} e^{-\alpha^2 r^2/2}\, P_{n\ell}(\alpha r) \qquad (3\text{-}54)$$

where the $P_{n\ell}$ are the associated Laquerre polynomials

$$P_{n\ell}(\alpha r) = \sum_{S=1}^{n} (-)^{S-1}\, 2^{S-n}\left[\frac{(2n+2\ell-1)!!}{(n-S)!\;(S-1)!\;(2\ell+2S-1)!!}\right](\alpha r)^{2S-2}\,. \qquad (3\text{-}55)$$

Clearly the product wave function can be written as

$$R_{n_1\ell_1}\, R_{n_2\ell_2} = \alpha^3 \sum_{n} A_n\,(\alpha r)^n\, e^{-\alpha^2 r^2} \qquad (3\text{-}56)$$

where n runs from $\ell_1+\ell_2$ to $\ell_1+\ell_2+2(n_1+n_2)$ in steps of 2. Finally, the reduced matrix element in equation (3-53) can be evaluated as

$$\begin{aligned}\left\langle j_1 \left\| T_{LSJ} \right\| j_2 \right\rangle &= \hat{j}_2\,\hat{J}\hat{\ell}_1\,\tfrac{1}{2}\,\mathrm{X}\left(j_1 j_2 J;\ \ell_1 \ell_2 L;\ \tfrac{1}{2}\,\tfrac{1}{2}\,S\right) \\ &\quad \times \left\langle \ell_1 \left\| Y_L \right\| \ell_2 \right\rangle \left\langle \tfrac{1}{2} \left\| \sigma^S \right\| \tfrac{1}{2} \right\rangle \\ &= \frac{\hat{j}_2\,\hat{\ell}_2\,\hat{\tfrac{1}{2}}\,\hat{J}\hat{L}\hat{S}}{4\pi}\ \mathrm{X}\left(j_1 j_2 J;\ \ell_1 \ell_2 L;\ \tfrac{1}{2}\,\tfrac{1}{2}\,S\right) \left\langle L0\,\ell_2 0 \,\middle|\, \ell_1 0 \right\rangle \end{aligned} \qquad (3\text{-}57)$$

The results in equations (3-53), (3-56) and (3-57) can be combined to give the result that

$$\bar{F}_{\lambda}(r) = A t_{\pi N}\, F_M(r) \qquad (3\text{-}58)$$

where

$$F_M(r) = \frac{f_o}{A}\,\alpha^3 \sum_N C_N(\alpha r)^N\, e^{-\alpha^2 r^2}$$

$$= \frac{f_o}{A}\,\alpha^3 \left[A(\alpha r)^\lambda + B(\alpha r)^{\lambda+2} + D(\alpha r)^{\lambda+4} + \cdots\right] e^{-\alpha^2 r^2}$$

where C_N includes the C_{ij}, the reduced matrix elements, and the coefficients of the polynomial, and where N runs from the smallest value of $\ell_1+\ell_2$ to the largest value of $\ell_1+\ell_2 + 2(n_1+n_2)$ for the configurations involved. F_M is divided by A (the number of nucleons) to correct for the A included explicitly, and the normalization f_o is used to correct for the extraneous spin factor of $\sqrt{2}$ which is often included in microscopic form factors calculated for proton scattering.

The next step is to include the pion force for a normal parity transition. In the notation of equation (2.43) this takes the form

$$\bar{F}_\lambda(r) = \frac{\hbar c}{2\bar{\omega}}\left[A_1 F(r) + \vec{\nabla}\cdot A_2 F(r)\ \vec{\nabla} + \nabla^2\, A_3 F(r)\right] \qquad (3\text{-}59)$$

for $F(r) = F_C(r)$ or $F_M(r)$. Notice that when $F_C(r)$ is used this is just

$$\bar{F}_\lambda(r) = -R_o \frac{\partial U_{opt}}{\partial r} \qquad (3\text{-}60)$$

where the first order form of U_{opt} is used. If we make the ansatz that the form factor can be calculated in the same way (i.e., by differentiating the potential) from the second order form of U_{opt}, equation (2.55), then the effects of second order terms in $t_{\pi N}$ can be included by using

$$\bar{F}_\lambda(r) = \frac{\hbar c}{2\bar{\omega}} \left\{ [A_1+2A_4\ \rho(r)]\ F_C(r) + \vec{\nabla}\cdot \frac{(A_2+2A_6\rho)\ F_C(r)}{\left[1+\frac{\lambda}{3}\left(A_2\ \rho+A_6\ \rho^2\right)\right]^2}\ \vec{\nabla} \right.$$

$$\left. +\ \vec{\nabla}\cdot\ [2A_5\ \rho(r)\ F_C(r)]\ \vec{\nabla} + \nabla^2\ (A_3+2A_7\rho)\ F_C(r) \right\} \tag{3-61}$$

We can extend this ansatz to include $F_M(r)$ based on the similar structure of these transition densities. Although reasonable, this model has less theoretical basis than the extension of equation (3-59) to second order potentials in the collective model.

An alternative approach for including the pion force is to do a simple folding calculation, described in Appendix E, where the force is used in momentum space. This takes the form

$$\bar{F}_\lambda(r) = 4\pi \sum_n w_n^2\ g_o(k_n)\ j_\lambda(k_n)\ \rho_\lambda(k_n) \tag{3-62}$$

where $w_n^2 = 2q^2/R_{max}$, $k_n = n(\pi/R_{max})$, and $\rho_\lambda(k_n)$ is the Fourier transform of the transition density $F_M(r)$, and $g_o(k_n)$ is the pion-nucleus interaction expressed in the local form

$$g_o(q) = \frac{(\hbar c)^2}{2\bar{\omega}}\left[A_1 - A_2\left(k^2 - \frac{q^2}{2}\right) + A_3(-q^2)\right] . \tag{3-63}$$

This form can also be used with the ansatz used in equation (3-62) by replacing A_1, A_2 and A_3 with the corresponding terms, except that $\rho(r)$ must be replaced with $\rho(q)$. However, the non-local form in equation (3-60) or (3-62) is a better interaction than the local form in equation (3-64) (with or without the second-order ansatz). In any case, this local form is quite useful for getting a qualitative picture of the effects of the corrections to $t_{\pi N}$ since it allows us to plot the force.

3.5 EVALUATION OF TRANSITION MATRIX FOR UNNATURAL PARITY TRANSITION

Unnatural parity transitions, since they involve spin flip in the target, can only be produced by the spin-orbit part of the pion-nucleus interaction. The interaction involved can be written [see Appendix E, equation (E-13)] in the folding model as

$$V_l = \sum_n w_n^2 \, g^{LS}(k_n) \; iZ'(LJ) \; [-iP_{JJ}(p)] \cdot T_{LlJ}(t) \qquad (3\text{-}64)$$

which differs substantially from the $T_{JOJ}(p) \cdot T_{JOJ}(t)$ form that occurs in normal parity transitions. Actually, the target space part is easy, and it has already been evaluated to give the result above in equation (3-57). What is new is the current operator

$$P_{JJ} = \left[T_J \times P\right]^J = \frac{i}{r}\sqrt{\frac{2J+1}{J+1}}\,\mathscr{L}_{J-1,J} \qquad (3\text{-}65)$$

where

$$\mathscr{L}_{J-1,J} = \left[Y_{J-1} \circledast \ell\right]^J$$

which changes the angular momentum algebra in the derivation of the T-matrix in Section 3.3. Specifically, the evaluation of $\left\langle \ell' \middle\| Y_\lambda \middle\| \ell \right\rangle$ in equation (3-38) must be replaced with the evaluation of $\left\langle \ell' \middle\| \mathscr{L}_{J-1,J} \middle\| \ell \right\rangle$. This matrix element is

$$\begin{aligned}
\left\langle \ell' \middle\| \mathscr{L}_{LJ} \middle\| \ell \right\rangle &= \left\langle \ell' \middle\| \left[Y_L \times \vec{\ell}\right]^J \middle\| \ell \right\rangle \\
&= \sum_{M_J m} \left\langle \ell m \; JM_J \middle| \ell' m' \right\rangle \left\langle \ell' m' \middle| \left[Y_L \circledast \ell\right]^{JM_J} \middle| \ell m \right\rangle \\
&= \sum_{M_J m} \sum_{m\mu} \left\langle \ell m \; JM_J \middle| \ell' m' \right\rangle \left\langle LM \; 1\mu \middle| JM_J \right\rangle \\
&\qquad \times (-)^\mu \left\langle \ell' m' \middle| Y_{LM} \, \vec{\ell} \middle| \ell m \right\rangle \quad . \qquad (3\text{-}66)
\end{aligned}$$

Since $\vec{\ell}_{-\mu}\left|\, \ell m\right\rangle = \sqrt{\ell(\ell+1)}\, \frac{\hat{\ell}}{\hat{1}}\, (-)^{\ell+m+\mu} \left\langle \ell m-\mu\ \ell -m \middle| 1-\mu \right\rangle \left|\, \ell m-\mu\right\rangle$

this becomes

$$\sum_{\substack{M_J m \\ M}} \ell m\ JM_J \left| \ell' m' \right\rangle \left\langle LM\ 1\mu \middle| JM_J \right\rangle \left\langle \ell m-\mu\ \ell -m \middle| 1-\mu \right\rangle$$

$$\left\langle \ell M-\mu\ LM \middle| \ell' m' \right\rangle \sqrt{\ell(\ell+1)}\, \frac{\hat{\ell}}{\hat{1}}\, (-)^{\ell+M+\mu} \left\langle \ell' \middle\| Y_L \middle\| \ell \right\rangle \tag{3-67}$$

The sum on four clebsches can be reduced to a Racah coefficient where

$$\sum_m \left\langle \ell m\ JM_J \middle| \ell' m' \right\rangle \left\langle LM\ 1\mu \middle| JM_J \right\rangle (-)^{m+\mu}$$

$$\left\langle \ell m-\mu\ \ell -m \middle| 1-\mu \right\rangle \left\langle \ell m-\mu\ LM \middle| \ell' m' \right\rangle$$

$$= \frac{\hat{1}}{\hat{\ell}}\, (-)^{L+1-J+\ell}\ \hat{\ell}\hat{J}\ W(\ell 1 \ell' L;\ \ell J) \tag{3-68}$$

which can be used to get the result

$$\left\langle \ell' \middle\| \mathscr{L}_{LJ} \middle\| \ell \right\rangle = (4\pi)^{-1/2}\ \frac{\hat{J}\ \hat{L}\ \hat{\ell}^2}{\hat{\ell}'} \sqrt{\ell(\ell+1)}\ (-)^{\ell'-\ell+1-J}$$

$$\times\ W(\ell 1 \ell' L;\ \ell J) \left\langle \ell 0\ L0 \middle| \ell' 0 \right\rangle \quad . \tag{3-69}$$

Since $\left\langle \ell' \middle\| Y_J \middle\| \ell \right\rangle = (4\pi)^{-1/2}\ \hat{\ell}\hat{J}/\hat{\ell}'\ (-)^{\ell-\ell'+J} \left\langle \ell 0\ J0 \middle| \ell' 0 \right\rangle$ for non-spin flip cases, we see that the spin-flip term requires an extra factor of

$$\hat{L}\hat{\ell}\ \sqrt{\ell(\ell+1)}\ \ W(\ell 1 \ell' L;\ \ell \lambda) \tag{3-70}$$

where $L = \lambda - 1$, and we also have to change

$$(-)^{\lambda} \left\langle \ell 0\ \lambda 0 \middle| \ell' 0 \right\rangle \rightarrow (-)^{L} \left\langle \ell 0\ L0 \middle| \ell' 0 \right\rangle , \tag{3-71}$$

which also changes the combinations of incoming and outgoing partial waves that match up in the integrals that form the matrix element.

What remains is the evaluation of the form factor, which is

$$\bar{F}_\lambda(r) = 4\pi \sum_n w_n^2 \, g^{LS}(k_n) \, \rho_J^S(k_n) \, j_J(k_n r) \qquad (3\text{-}72)$$

where ρ_J^S is given in equation (E-15), and

$$g^{LS}(q) = -4\pi \frac{(\hbar c)^2}{2\bar{\omega}} (s_o + s_1 \, \underline{t}\cdot\underline{\tau}) \, q^2 \qquad (3\text{-}73)$$

which is obtained from equation (E-11). This form factor in equation (3-72) is calculated by ALLWRLD [Car 81a] and supplied to MSUDWPI for the scattering calculation.

3.6 SUMMARY

In this chapter we have outlined the basic equations of the DWBA and their specific application to the problem of pion inelastic scattering. In equations (3-29) and (3-32) the formula for the inelastic cross section was presented in terms of a set of transition matrix elements. In equation (3-43) these matrix elements were expressed in terms of the overlap between the distorted waves and the pion-nucleus form factor for normal parity transitions. The modifications required for unnatural parity transitions were given in equations (3-70) and (3-71). Finally, the models for including the nuclear structure and the pion-nucleus interaction in the form factor were presented. The

collective and microscopic transition densities were defined in equations (3-49) and (3-58), while the form of the interactions to be investigated were presented in equations (3-59), (3-61), (3-62) and (3-72).

The remainder of this thesis will be concerned with the application of these formulae and the testing of these models. At first the pion-nucleus interaction will be tested against transition densities determined by nucleon scattering. Later, the knowledge of the interaction will allow the study of some new states and their nuclear structure.

CHAPTER 4

INELASTIC SCATTERING IN THE COLLECTIVE MODEL

The remainder of this thesis will be devoted to the examination of various test cases that illustrate the properties of the pion-nucleus interaction and the application of these techniques to the study of the nature of nuclear excited states. This chapter primarily addresses the first of these concerns: the following sections will examine transitions to collective states in order to study the properties of the pion-nucleus effective interaction.

The existing collection of inelastic data place narrow limits on the choice of test cases. The nuclei for which data are available at a range of energies are ^{12}C, the 4.44 MeV 2^+ state, and ^{40}Ca, the 3.74 MeV 3^- state. The former will be used in the detailed comparisons of the next three sections, while the latter will be included at the end for comparisons with microscopic models in the next chapter.

The first two sections will examine in detail the effects of including various corrections to the pion-nucleus interaction at 50 MeV (Section 4.1) and 162 MeV (Section 4.2). The elastic scattering optical potential will be fixed at one that fits the elastic scattering data, normally Set D defined in Chapter 2. The effects of changes in the distorted waves due to the use of other optical potentials will be discussed separately in Section 4.3. The remainder of the chapter will present a survey of low (Section 4.4) and higher (Section 4.5) energy scattering to states described by the collective model. This will review most of the states for which data exist, as well as some for which data is not yet available.

Throughout this chapter the curves drawn on the figures will follow a consistent pattern. A curve based on a theoretical force will be dashed and a curve based on a fitted force will be a solid line. A dash-dot curve will be used for a second fitted force. Exceptions to this convention will be noted as needed.

4.1 EXAMPLE OF COLLECTIVE MODEL AT LOW ENERGY

The 4.44 MeV 2^+ state in ^{12}C has been chosen for this example because it is the best known angular distribution for low energy pion scattering. The other transitions that have been observed at low energy are fairly recently studied and often incompletely known. This state offers the additional advantage of having been extensively studied with other projectiles. The use of a form factor determined by an independent experiment allows the separate investigation of the properties of the pion interaction.

For these calculations we will use the collective model described in Section 3.4, with $\beta_2 = 0.60$ taken from proton scattering analyses [Fri 65]. The elastic scattering optical potential will be the one given by Set D in Table 2-4. The only remaining factor in the model is then the pion-nucleon interaction, which will be examined by comparing the predictions of the various interactions presented in Chapter 2. The effects will be illustrated by plotting the pion-nucleus t-matrix, using the local approximation described in Appendix B, alongside the angular distribution [Dyt 79] for the inelastic scattering. The figures will also show the elastic scattering data taken by the same experimental group, for scale. The other elastic data are from [Pre 81].

The first calculations use the four parameter potential developed in Section 2.2 based on the Impulse Approximation (IA). The IA potential using phase shift parameters (Set A) is shown as the dashed curve in Figure 4-1. The minimum in the angular distribution occurs at 80° rather than at 65° as required by the data. This is the same shift that we saw for the elastic scattering earlier. The plot of the t-matrix on the right shows quite clearly that this shift is due to a defect in the force, specifically the relative strengths of the s- and p-wave parameters. The solid curve is the result of the fit to all four parameters, Set B. Notice that when the elastic is fit the interference minimum falls in the correct location. The dash-dot curve uses Set B', which only varies three parameters in the fit. This alternate fit is quite similar in character to the other fit -- leading to the observation that forces with quite different parameters can be essentially equivalent in their description of the pion-nucleus interaction.

Figure 4-2 shows the same case, except that the full potential was used. The dashed curve is the purely theoretical potential based on phase shift values for the parameters, with absorption parameters as calculated by Riska [Cha 79a]. Agreement with the data is quite good. The graph of the t-matrix shows how the LLEE effect and second-order s-wave parameters give the correct interference. The solid curve shows the fitted Set (D), where the only major change is a further increase in b_o by 50%. This shifts the minimum a small amount and raises the inelastic calculation to give slightly better agreement with the data.

It has been noted before [Str 79, Dyt 79] that potentials which fit the elastic will also reproduce the inelastic data. Now we see a

Figure 4-1

Elastic and inelastic scattering of 50 MeV π^+ from ^{12}C and its 4.44 MeV (2^+) state using optical parameters from Set D and an inelastic scattering t-matrix (plotted on the right) defined with parameters from sets A, B and B', shown with dashed, solid and dash-dot curves, respectively.

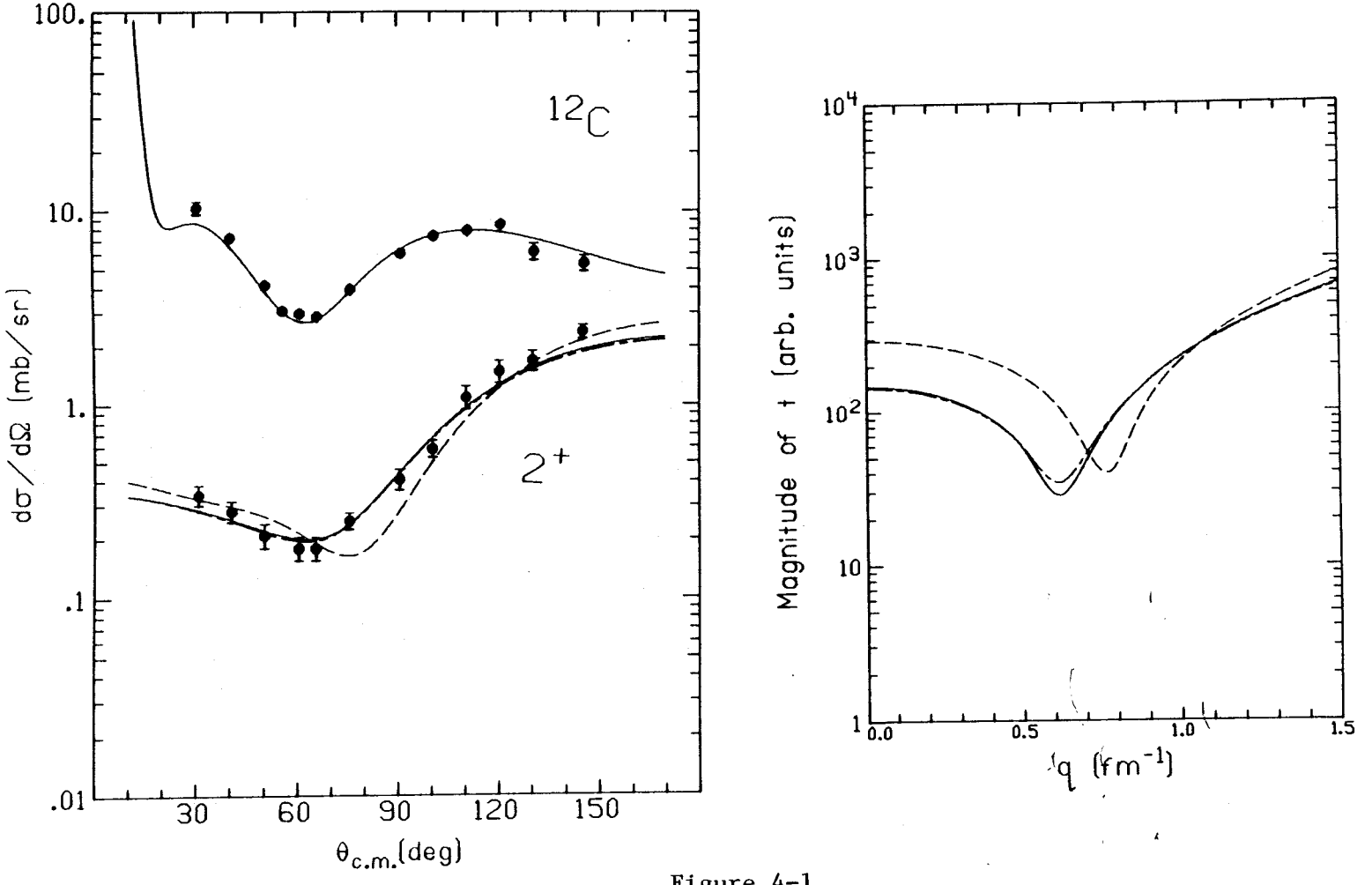
100.
10.
1.
.1
.01
dσ/dΩ (mb/sr)
12C
2+
30
60
90
120
150
θc.m.(deg)
10^4
10^3
10^2
10
1
Magnitude of t (arb. units)
0.0
0.5
1.0
1.5
q (fm^-1)

Figure 4-1

Figure 4-2

Same as Figure 4-1, except the t-matrix was calculated with parameters from sets C and D, shown with dashed and solid curves, respectively.

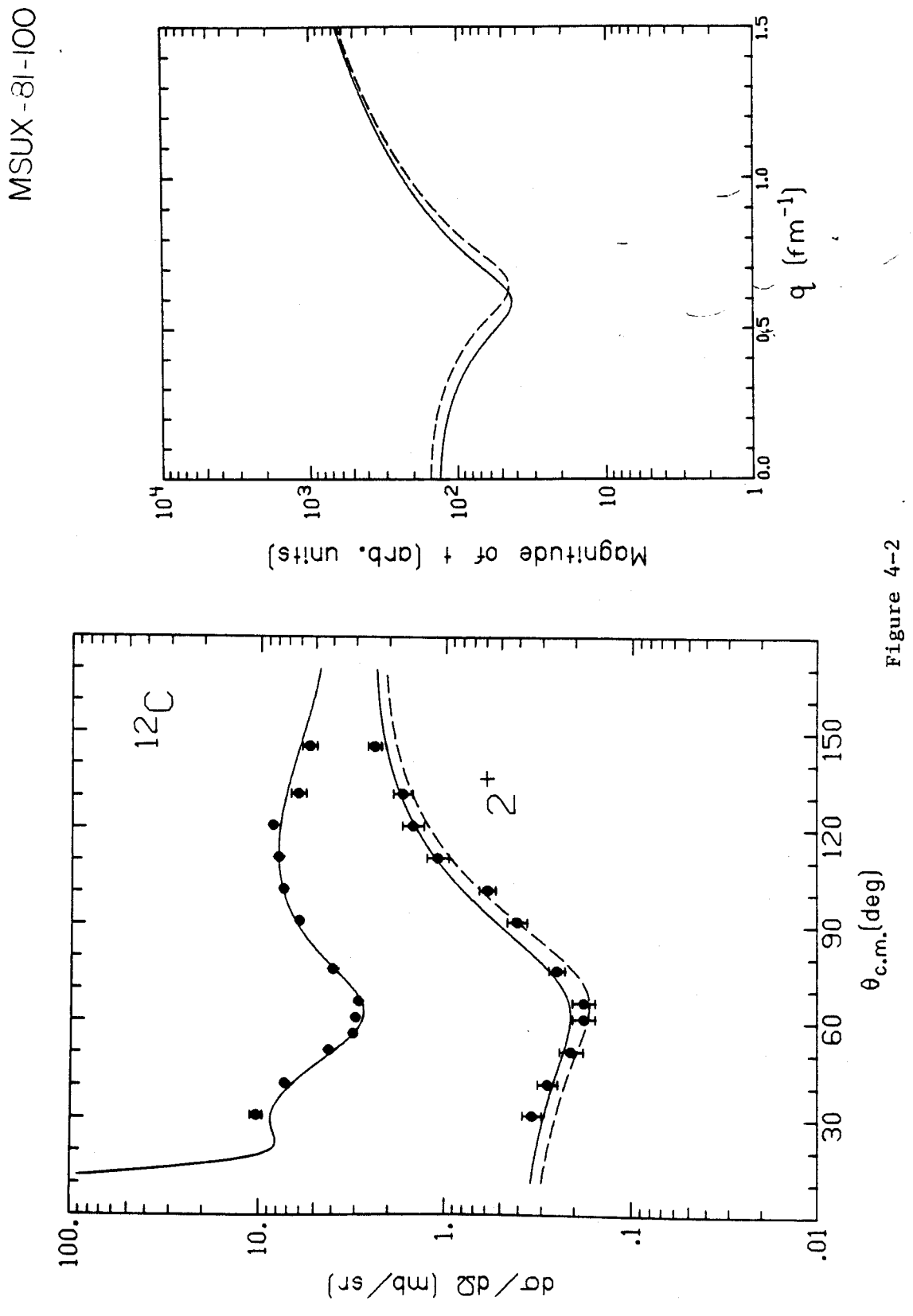
MSUX-81-100
^{12}C
2^+
100.
10.
1.
.1
.01
dσ/dΩ (mb/sr)
30
60
90
120
150
$\theta_{c.m.}$(deg)
Magnitude of + (arb. units)
10^4
10^3
10^2
10
1
0.0
0.5
1.0
1.5
q (fm^{-1})

Figure 4-2

much more interesting result: potentials that give similar fits to the elastic data will also fit the inelastic data, even if the optical potential that generates the distorted waves is held constant. The fact that a four-parameter and nine-parameter potential give similar results suggests that they are both modeling an effective interaction that describes the pion in a nucleus. Thus we have the advantage of using the full potential when discussing the values of the parameters in the context of multiple scattering theory, and also using a completely equivalent four-parameter potential to discuss the qualitative behaviour in a simple and straightforward fashion.

In summary, the 50 MeV inelastic data for ^{12}C are well described by any of the potentials (B, B', D) which were fit to the elastic scattering. The theoretical Set (C) also does an adequate job. This can be attributed to the similarity of the t-matrices for these potentials, which reflect a common effective interaction.

4.2 EXAMPLE OF COLLECTIVE MODEL NEAR THE RESONANCE

The same state (4.44 MeV 2^+ in ^{12}C) and transition density (collective model with $\beta_2 = 0.60$) will be used in this example. The data are at 162 MeV [Cha 79] for both π^+ and π^-. We will only look at the π^+ here, but both will be shown later in Section 4.5. These data are particularly interesting because they were taken all the way back to 180°, the only such case currently available. The elastic scattering is calculated using Set D for every case.

The first set of calculations, shown in Figure 4-3, use the IA form of the force given in equation (2-43). The dashed curve shows Set A, which uses the phase shift parameters with no adjustments. It

Figure 4-3

Elastic and inelastic scattering of 162 MeV π^+ from ^{12}C and its 4.44 MeV (2^+) state using optical parameters from Set D and an inelastic scattering t-matrix (plotted on the right) defined with parameters from sets A, B and B', shown with dashed, solid and dash-dot curves, respectively.

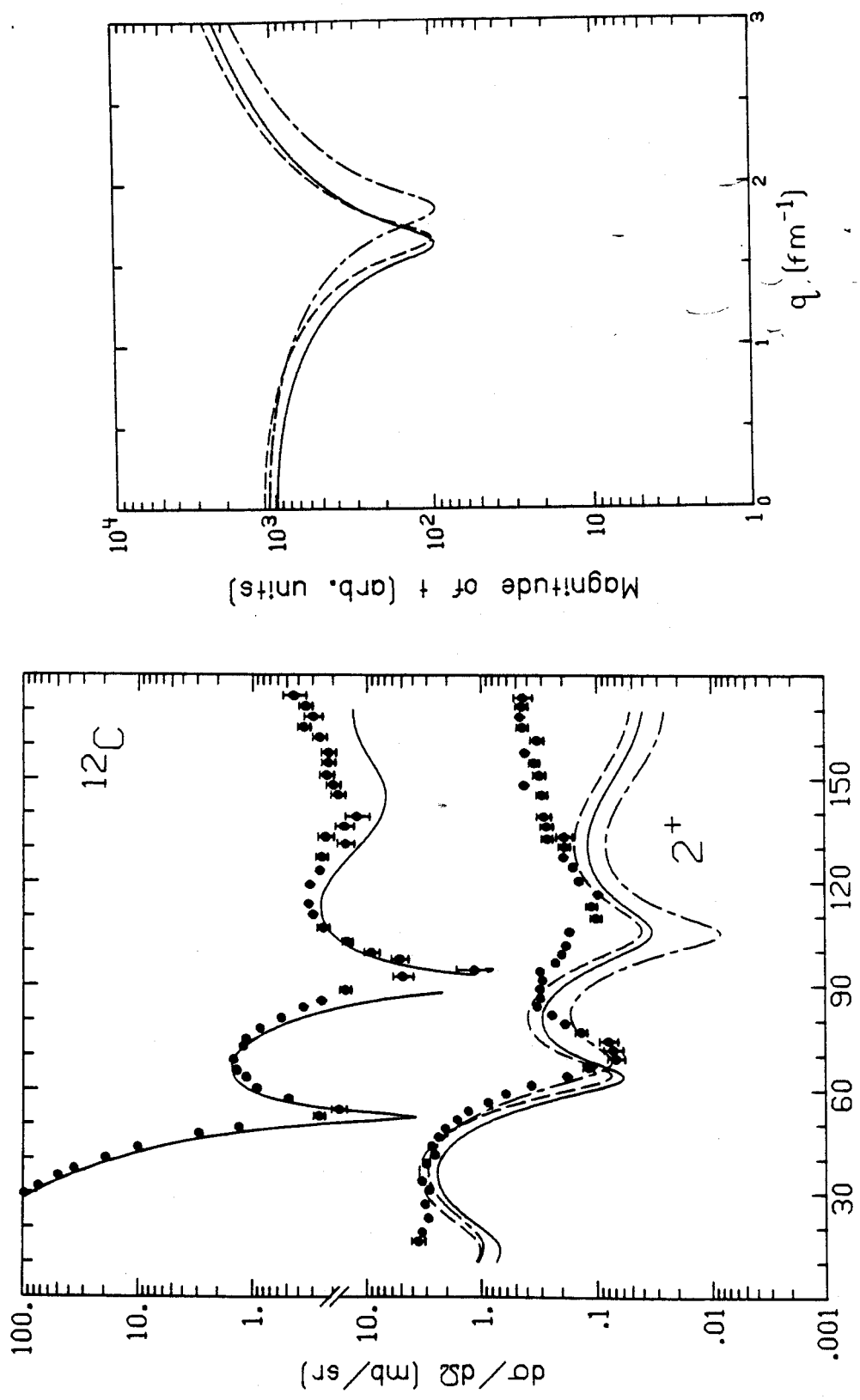
MSUX-81-101
12C
2+
dσ/dΩ (mb/sr)
θc.m.(deg)
Magnitude of + (arb. units)
q (fm-1)

Figure 4-3

does a fair job of reproducing the experimental values at small angles, but it has the wrong phase. This is the same problem we had with the 162 MeV elastic data. Notice that the angular distribution is now diffractive, with the minimum in the force at 70° not evident in the calculation which has a minimum at 65°. The solid curve uses Set B, which was fit to the elastic, but there is little improvement. The dash-dot curve used Set B', where the ∇^2 term was dropped, and the result is an improvement in the first minimum at the expense of the back angle data. The t-matrix shows the shift of the minimum to larger q, so the nucleus looks smaller and the minimum is shifted. Notice that the second minimum is not affected, and thus the apparent improvement is not really very great.

Figure 4-4 shows the same series of calculations, but the full interaction given in equation (2-55) has been used. The difference between the theory (Set C, dashed) and fitted (Set D, solid) curves is negligible. Except for the phase at the first minimum and the rise at 180°, the data is well described by this calculation. As before, dropping the ∇^2 terms (Set D') improves the fit at the first minimum but fails at larger angles.

The pion-nucleus effective interaction is fairly well described by the full potential with either theoretical values (phase shifts and Riska's absorption values) or adjusted p-wave strengths. The four-parameter model does not seem to be completely equivalent. It is similar at forward angles but lacks the density dependence that seems important to the description of data between 90° and 180°. Although Set D fails to reproduce some important details, there is a dramatic improvement at backward angles.

Figure 4-4

Same as Figure 4-3, except the t-matrix was calculated with parameters from sets C, D and D', shown with dashed, solid and dash-dot curves, respectively.

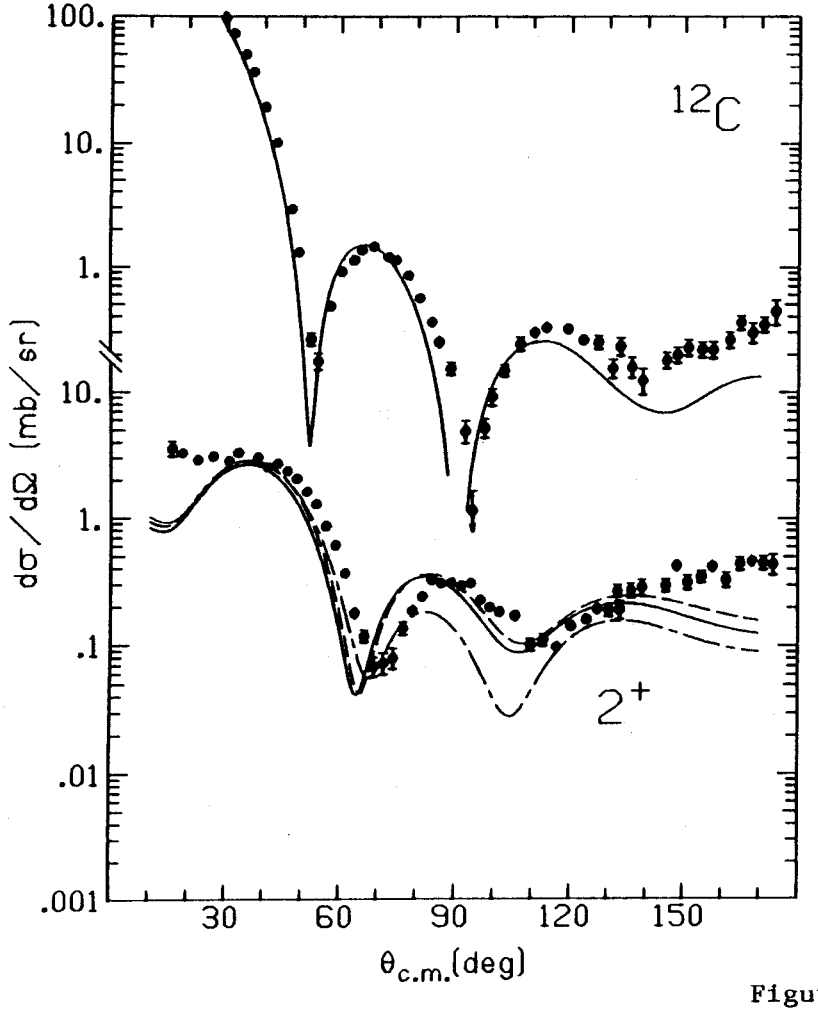
100.
10.
1.
10.
1.
.1
.01
.001
^{12}C
2^+
$d\sigma/d\Omega$ (mb/sr)
30
60
90
120
150
$\theta_{c.m.}$(deg)

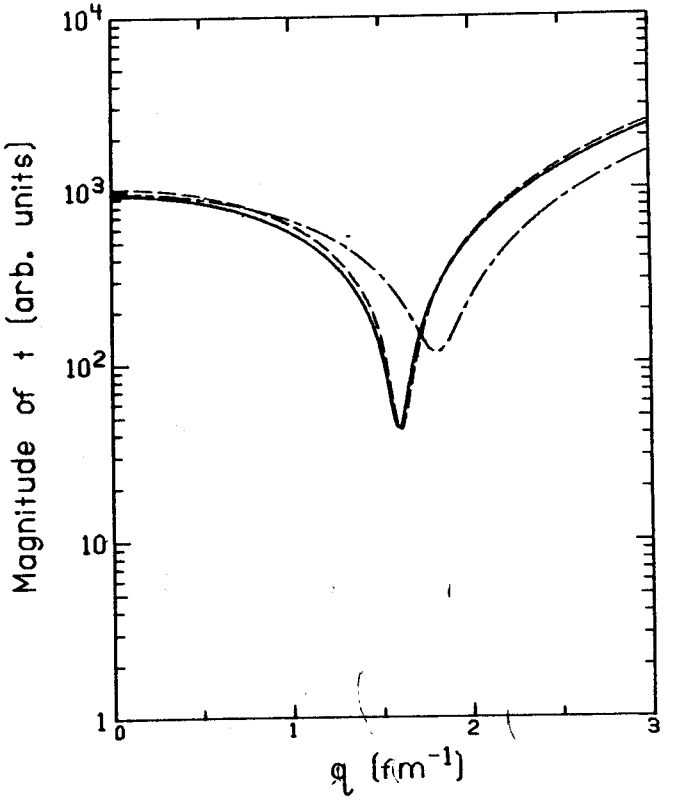
10^4
10^3
10^2
10
1
0
1
2
3
Magnitude of t (arb. units)
q (fm^{-1})

Figure 4-4

In summary, the calculations with the full potential describe the data much better than the other alternatives, particularly at back angles. If the phase problem near 70° can be understood, then large angle data will become a crucial test of the form to be used for the force and any possible coupled channels effects.

4.3 DISTORTED WAVE EFFECTS

The calculations in the preceding sections used a fixed optical parameter set in order to eliminate any variation due to changes in the distorted waves. However, the choice of optical parameters is not well determined and it is important to identify how these changes affect the inelastic cross section. Figure 4-5 shows $|S_\ell|^2$, where $S_\ell = \exp(2i\delta_\ell)$ and δ_ℓ = phase shift for the ℓ^{th} partial wave. The magnitude of S_ℓ is a measure of the transparency of the potential, since it is 1.0 when the phase shifts are purely real and less than 1.0 as flux is removed from that partial wave. As can be readily seen in the figure, there are some significant differences in the makeup of distorted waves produced by different potentials.

The 50 MeV curves are for sets A (dashed), B (solid) and B' (dash-dot). The different absorption required by the fitted sets is clearly evident; what is surprising is the large differences between the two fitted sets which reflects the different distribution of the absorption between the s- and p-waves. The 163 MeV curves show little of this sensitivity. Sets A, B and B' are all strongly absorbing and determine the same radius, so different choices should not affect the inelastic scattering results as much as they do at 50 MeV. One can also see why a diffraction model, which assumes a sharp cutoff at a characteristic

Figure 4-5

Plots of $|S_\ell|^2$ for elastic scattering of 50 and 162 MeV π^+ with parameters from sets A, B and B', shown with dashed, solid and dash-dot curves, respectively.

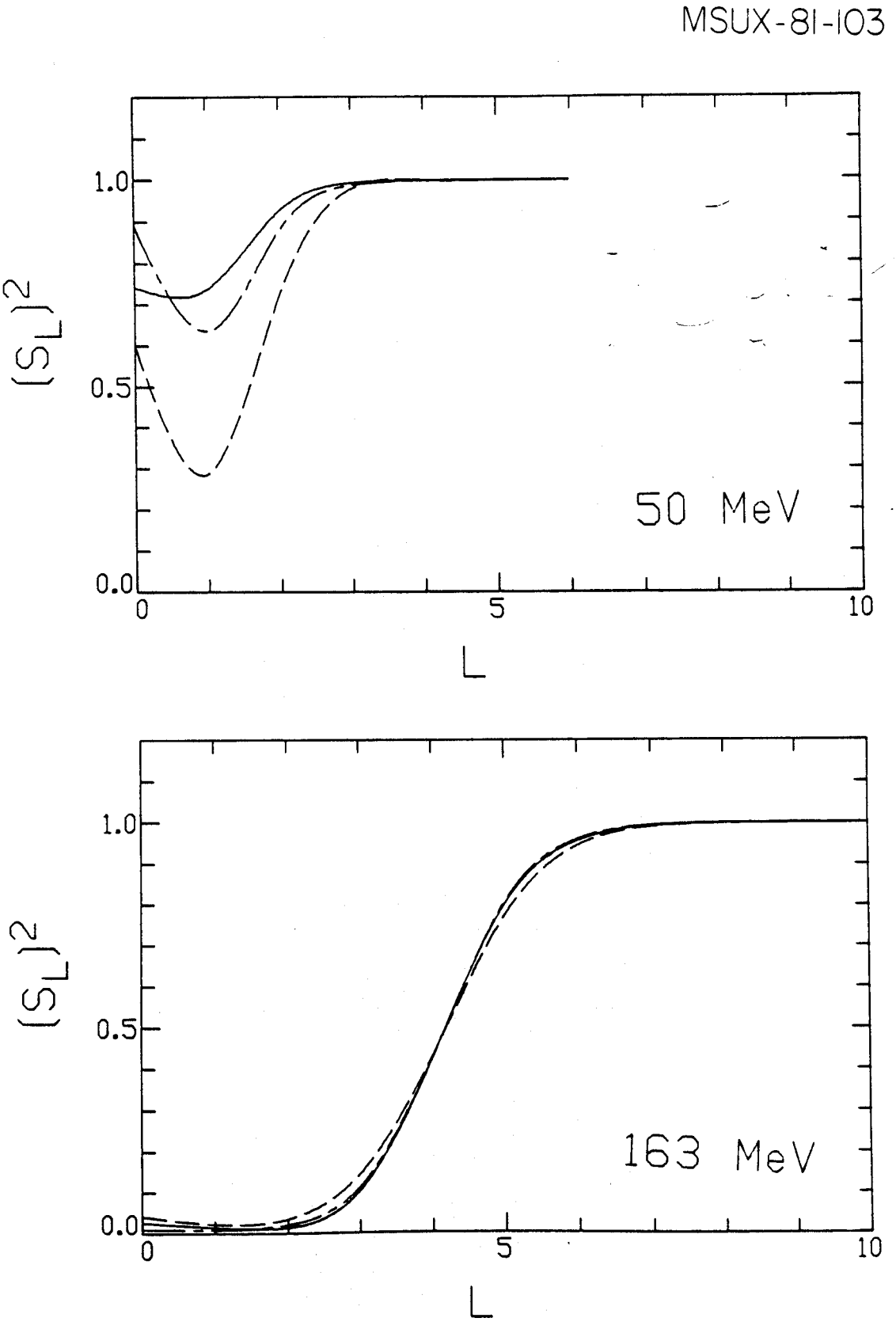

Figure 4-5

value of ℓ, would give a good approximation to the resonance region data.

The effects of distortion will be illustrated by the same calculations as we used in Sections 4.1 and 4.2 except that now the t-matrix used in evaluating the form factor is held constant (at Set D) while the optical potential is varied. Thus the figures will now have pairs of curves, the first showing the change in the elastic scattering cross section and the second showing the induced effect on the inelastic calculation. The 50 MeV results will be presented first, followed by the 163 MeV calculations.

The solid curves in Figure 4-6 use Set D for the elastic, and are thus exactly the same calculations as were shown in Figure 4-2. The dashed curves show the effect of using Set C, the theoretical values, in the full optical potential. The curves are slightly higher, but clearly the change in b_0 does not have a big effect here.

The curves in Figure 4-7 show a much greater sensitivity to the potential. These use the four-parameter potential with sets B (solid), B' (dash-dot) and A (dash), which were the ones used in Figure 4-5. Using Set A destroys the agreement in the inelastic calculation, as might be expected. What is more interesting is that sets B and B' produce measurably different results (as Figure 4-5 would suggest) while the elastic calculations differ mainly in the coulomb-nuclear interference region. It's clear that measurements in this region would help pin down the optical potential at low energy, although data taking is difficult at these angles.

These results are summarized in Figure 4-8, where both the optical potential and the inelastic scattering t-matrix are varied. The solid

Figure 4-6

Elastic and inelastic scattering of 50 MeV π^+ from ^{12}C and its 4.44 MeV (2^+) state using Set D to calculate the inelastic scattering t-matrix, while the optical potential used parameters from sets C (dashed curve) and D (solid curve).

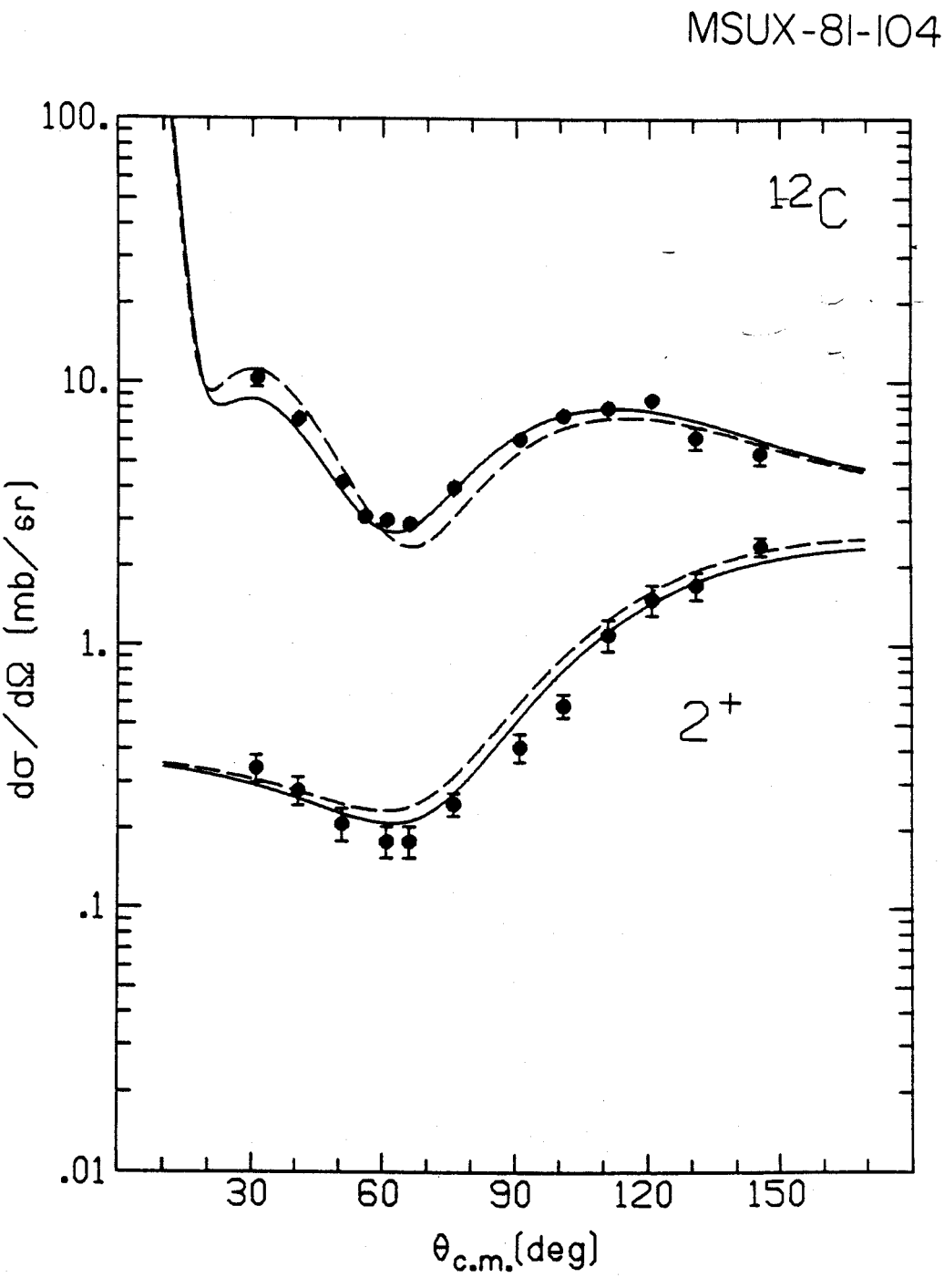

Figure 4-6

Figure 4-7

Same as Figure 4-6, except the optical potential used parameters from sets A, B and B', shown with dashed, solid and dash-dot curves, respectively.

MSUX-81-105

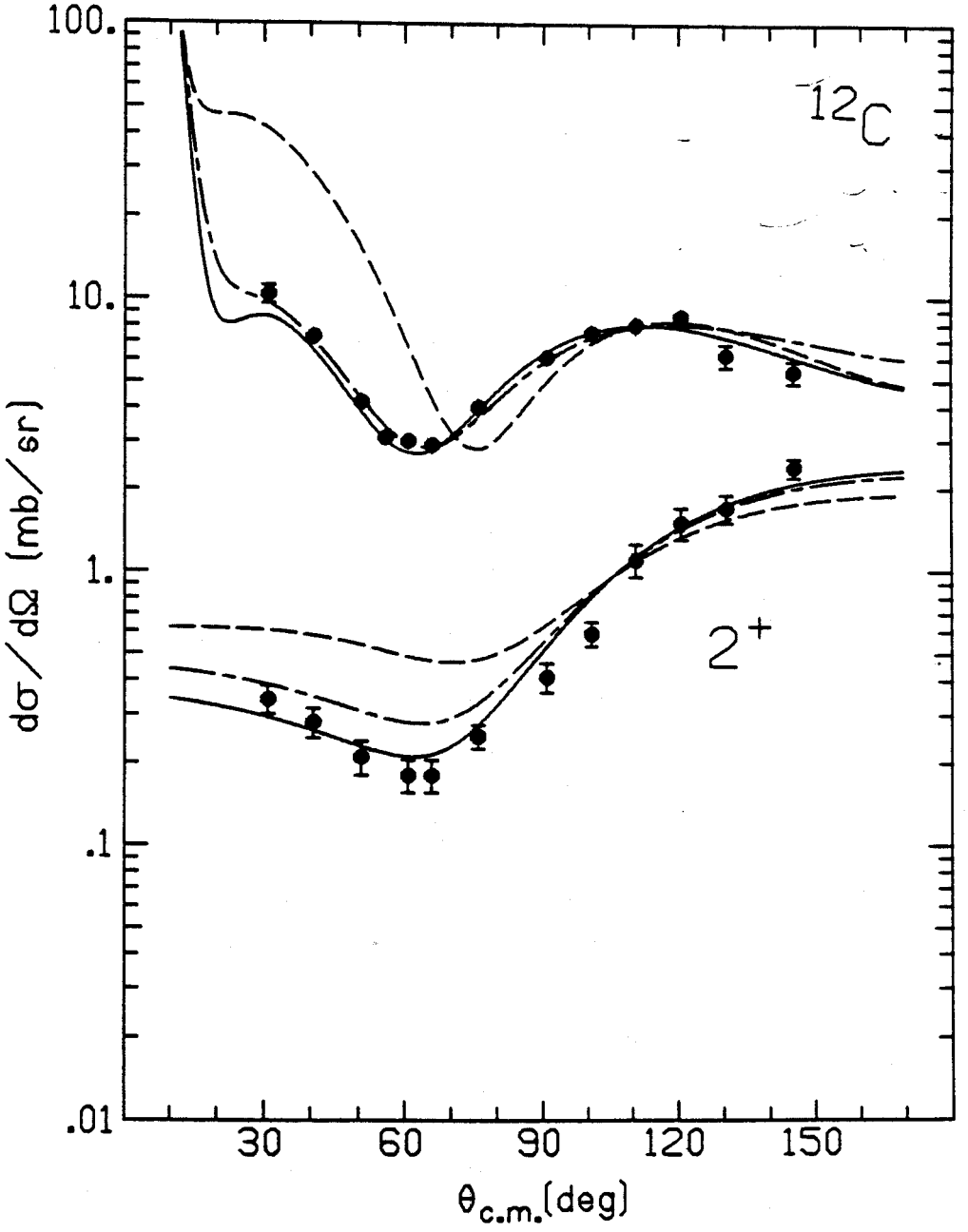

Figure 4-7

Figure 4-8

Same as Figure 4-6, except the same parameters were used for both the optical potential and the inelastic scattering t-matrix, either Set B (dashed curve) or Set D (solid curve).

MSUX-81-106

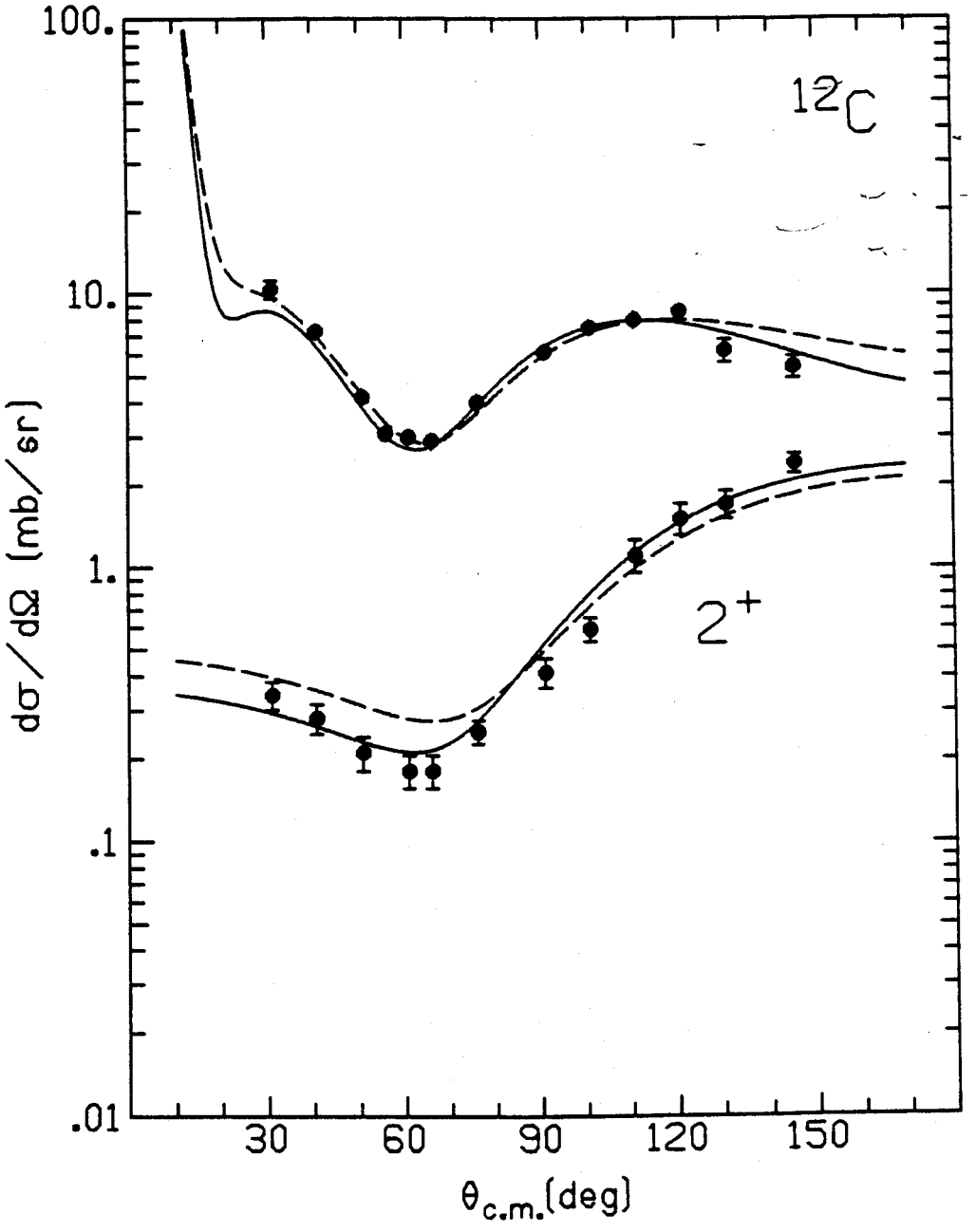

Figure 4-8

curve uses Set D (fitted with full potential), while the dashed curve is Set B (fitted with four-parameter potential). We saw in Section 4.1 that these potentials produced equivalent inelastic cross sections, while in this section we saw that the results were extremely sensitive to some details of the optical potential. In this case, most of the variation in the inelastic results is due to the change in the optical potential. Thus at low energy we have a fairly well defined effective pion-nucleus interaction for inelastic scattering, but are quite sensitive to the choice of the distorting potential.

We now turn our attention to the effects of distortion at 163 MeV. The t-matrix for the inelastic transition is fixed using the parameters of Set D. Then the solid curves in Figure 4-9, which use Set D for the elastic, are the same as in Figure 4-4 for comparison. Clearly it makes little difference whether we use Set D or sets C (dash) or D' (dash-dot) for the distortion -- the inelastic results are nearly identical. The same conclusion can be made from Figure 4-10, where sets B (solid) and B' (dash-dot) also give nearly identical results. The only exception is Set A (dashed), which is based on phase shifts only, where the inelastic calculation comes out lower than the others. This last case corresponds to the dashed curve in Figure 4-5, which differs from the others with respect to the slope in the surface region.

These results are summarized in Figure 4-11, where both the optical potential and the t-matrix are varied. The solid curve is for Set D (fitted with full potential), while the dashed curve is for Set B' (fitted with four-parameter potential with no ∇^2 term). We saw in Section 4.2 that these two sets produced very different inelastic cross sections when the same optical potential was used, whereas we just

Figure 4-9

Elastic and inelastic scattering of 162 MeV π^+ from ^{12}C and its 4.44 MeV (2^+) state using Set D to calculate the inelastic scattering t-matrix, while the optical potential used parameters from sets C, D and D', shown with dashed, solid and dash-dot curves, respectively.

MSUX-81-107

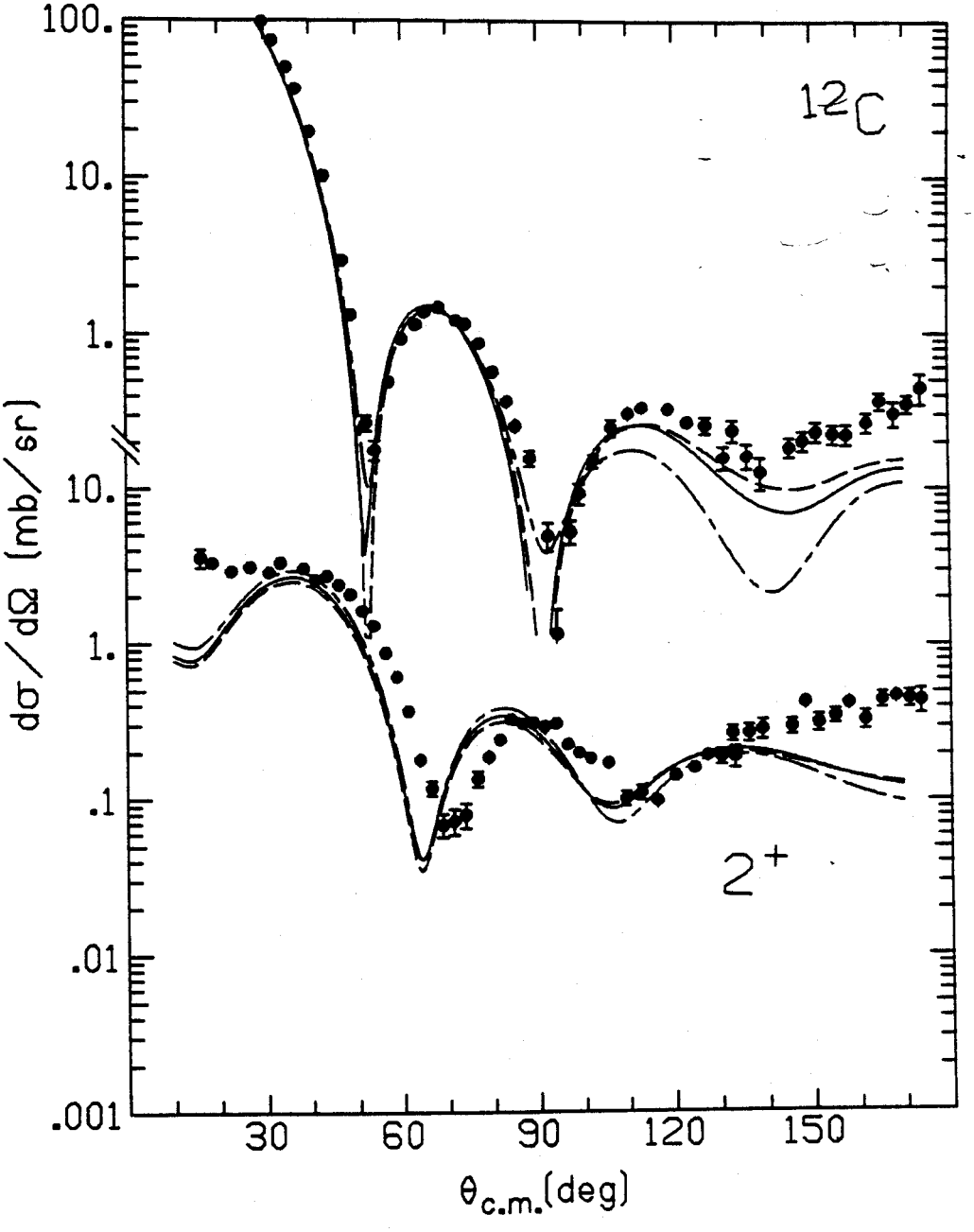

Figure 4-9

Figure 4-10

Same as Figure 4-9, except the optical potential used parameters from sets A, B and B', shown with dashed, solid and dash-dot curves, respectively.

MSUX-81-108

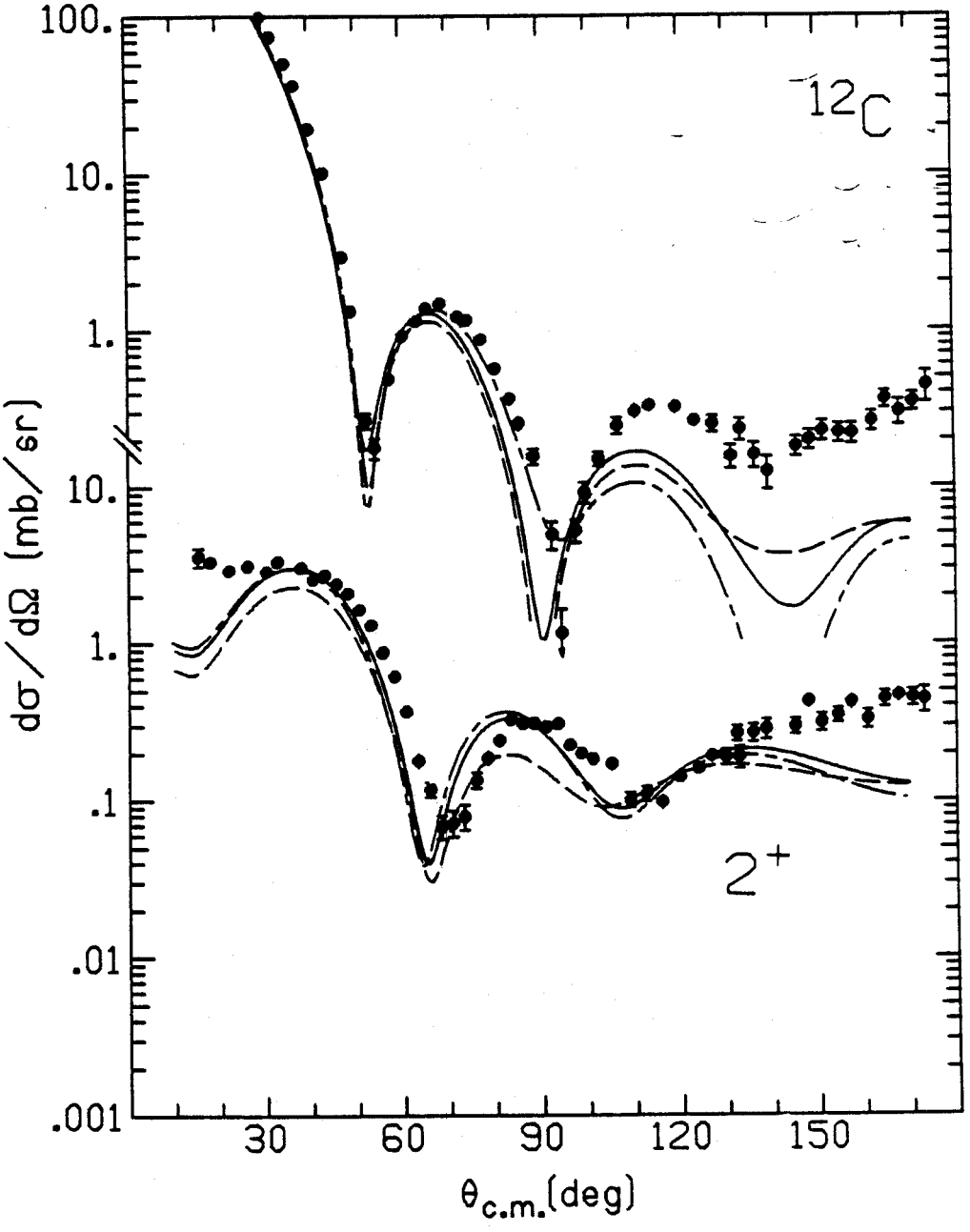

Figure 4-10

Figure 4-11

Same as Figure 4-9, except the same parameters were used for both the optical potential and the inelastic scattering t-matrix, either Set B' (dashed curve) or Set D (solid curve).

MSUX-81-109

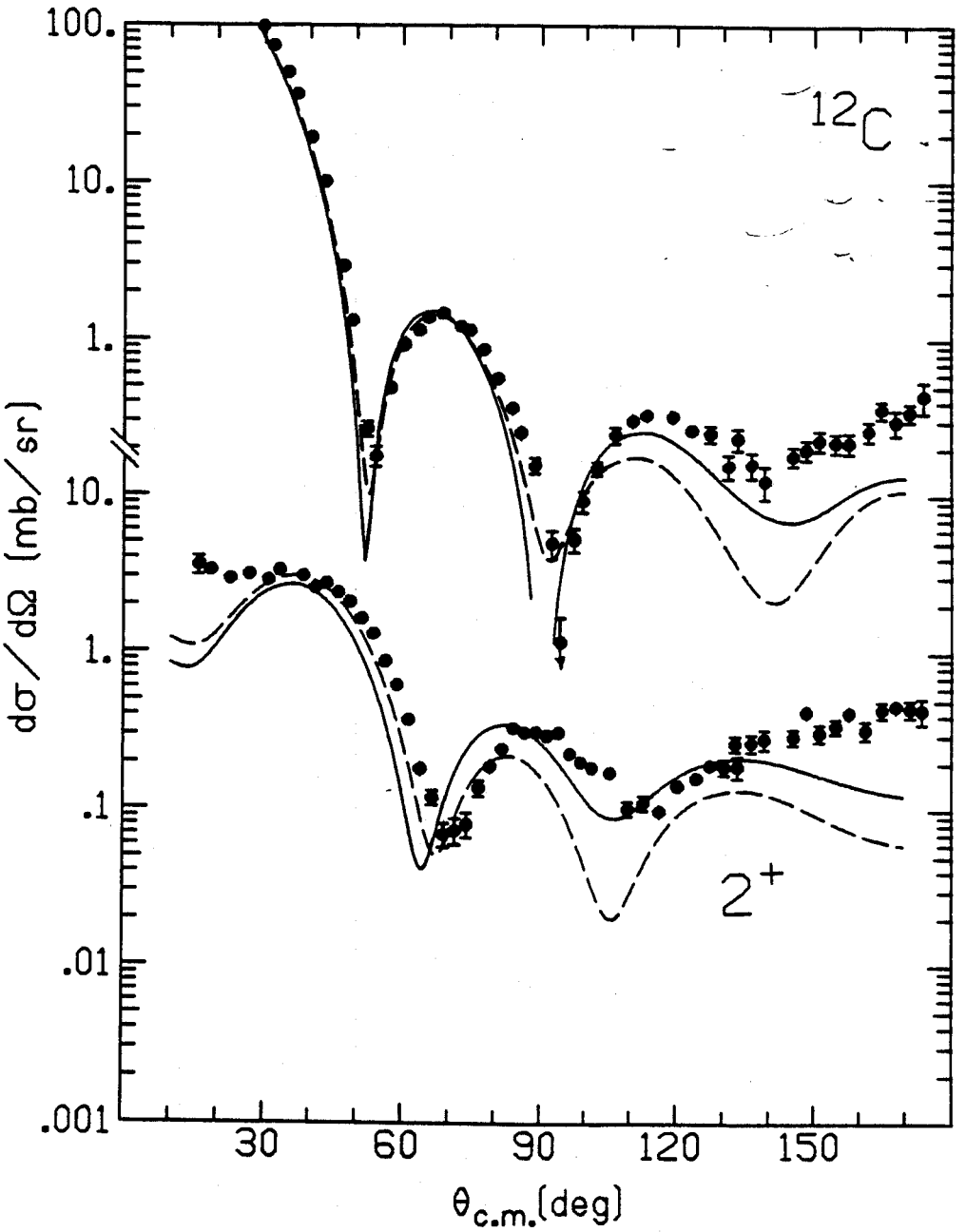

Figure 4-11

learned that the optical potentials alone do not affect the inelastic results in any significant way. The entire variation in the inelastic calculations is due to the change in the t-matrix used to calculate the form factor -- exactly the opposite of the situation at low energy. Thus at high energy we have a reasonably well defined distorting potential (despite some rather obvious defects) but greater sensitivity to the effective interaction. The full potential, with some adjustments, seems to be preferred over the other models that have been examined.

4.4 OTHER LOW ENERGY CASES

We will now proceed to survey the existing experimental data to see how their trends fit into the patterns that have been outlined for the two specific cases above. This section will only review data below 100 MeV. This division is convenient and historical: the only apparatus for such experiments is the Low Energy Pion (LEP) channel at Los Alamos, and most data there were taken near 50 MeV. Now that LEP has been pushed up to 80 MeV, this division is less sharply drawn. Indeed, one goal of current research is to predict the complicated transition between the simple descriptions of 50 and 163 MeV scattering that have been given here.

For simplicity, these discussions will be restricted to two parameter sets. One will be Set C, which uses phase shift values [Row 78] for the single nucleon parameters and Riska's values [Cha 79a] for the absorption. These are given in Table 4-1 for the energies we will study in this section. The other will be Set D, which has Reb_0, Rec_0, and the amount of absorption (with ImB_0/ImC_0 fixed at the pionic atom value) adjusted to fit the elastic data. These are given in Table 4-2. The

Table 4-1

Parameter Set C Theory Values
for Low Energy Scattering

	36 MeV	50 MeV	67 MeV	80 MeV
$\bar{b}_o$	-0.041 +0.004 i	-0.045 +0.006 i	-0.051 +0.009 i	-0.055 +0.011 i
b_1	-0.131 -0.001 i	-0.131 -0.002 i	-0.130 -0.002 i	-0.129 -0.002 i
c_o	0.71 +0.011 i	0.75 +0.028 i	0.79 +0.063 i	0.82 +0.10 i
c_1	0.44 +0.005 i	0.45 +0.013 i	0.47 +0.031 i	0.47 +0.05 i
λ	1.6	1.6	1.6	1.6
B_o	-0.01 +0.12 i	-0.02 +0.14 i	-0.03 +0.16 i	-0.04 +0.18 i
C_o	0.33 +0.50 i	0.36 +0.59 i	0.41 +0.74 i	0.48 +0.92 i

Table 4-2

Parameter Set D Fitted Values
for Low Energy Scattering

	36 MeV*	50 MeV	67 MeV	80 MeV
$\bar{b}_o$	-0.056 +0.004 i	-0.060 +0.006 i	-0.048 +0.009 i	-0.026 +0.011 i
b_1	-0.131 -0.001 i	-0.131 -0.002 i	-0.130 -0.002 i	-0.129 -0.002 i
c_o	0.74 +0.011 i	0.75 +0.028 i	0.64 +0.063 i	0.54 +0.10 i
c_1	0.44 +0.005 i	0.45 +0.013 i	0.47 +0.031 i	0.47 +0.05 i
λ	1.6	1.6	1.6	1.6
B_o	-0.01 +0.14 i	-0.02 +0.12 i	-0.03 +0.13 i	-0.04 +0.28 i
C_o	0.33 +0.77 i	0.36 +0.66 i	0.41 +0.76 i	0.48 +1.54 i

*Linearly Interpolated.

one exception is at 36 MeV, where the values were interpolated between zero and 50 MeV since the data seemed too sparse for a reliable fit. There are indications [Car 81] that this procedure can explain all the data between zero and 50 MeV within systematic errors.

Some conventions have been chosen. Set D is shown with a solid curve. The elastic and inelastic calculations use the same force. Results for π^- scattering have been shown whether data exists yet or not, since these are an important prediction of the model. Solid points are used for π^+ data, while open ones indicate π^- data.

We begin with 36 MeV calculations for scattering from ^{12}C (4.44 MeV 2^+ state) and ^{28}Si (1.73 MeV 2^+ state). The density parameters are given in Appendix C. The collective model form factor for ^{12}C uses $\beta_2 = 0.60$ [Fri 65] as before. The form factor for ^{28}Si uses $\beta_2 = 0.40$ [Ful 68]. The results of these calculations are shown in Figure 4-12. The data are all from [Ama 81].

The results for π^+ elastic scattering are fair, as might be expected since Set D was not fit to the data. This set agrees much better [Car 81] with the 40 MeV [Ble 79] and 30 MeV [Pre 81] elastic data taken by a different experimental group on the same beam line. There must be some systematic normalization differences. Notice that the shape, particularly the absence of a clear dip in the coulomb-nuclear interference region near 30°, is well reproduced. The inelastic calculations slightly overestimate the cross section for the 2^+ in ^{12}C, but underestimate that for the 2^+ in ^{28}Si. The latter will turn out to be a persistent problem, and will be discussed at length in Section 4.5.

The π^- predictions are shown on the right. The characteristic shape change from π^+ to π^-, due to the change in sign of the coulomb

Figure 4-12

Elastic and inelastic scattering of 36 MeV π^+ and π^- from ^{12}C (top row) and ^{28}Si with parameters from Set C (dashed curve) and Set D (solid curve) as described in the text.

MSUX-81-110

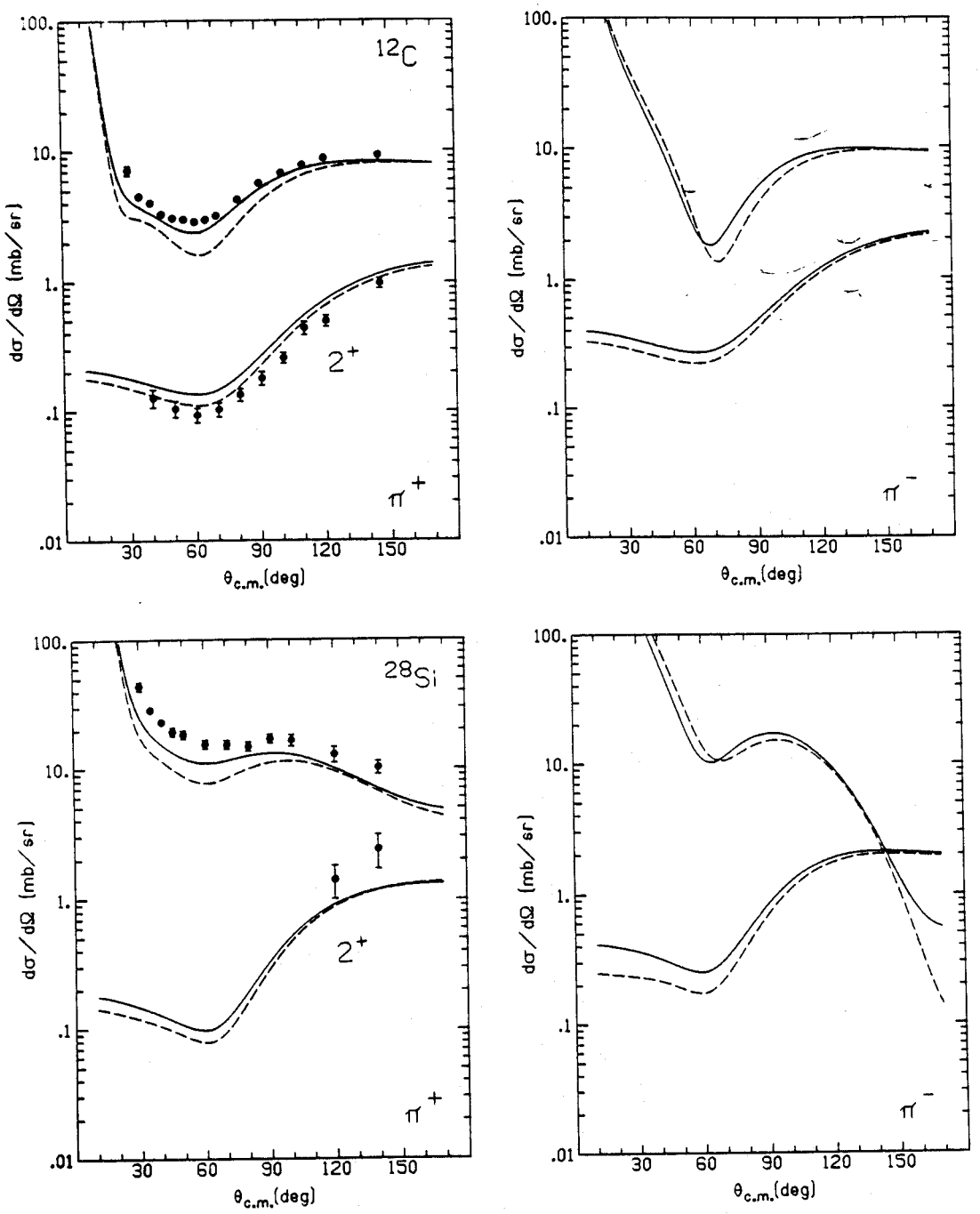

Figure 4-12

term which eliminates the forward angle interference, is seen. This change agrees with data [Joh 78] at 29 MeV [Str 80]. The inelastic calculations do not substantially change shape.

We now turn our attention to the 50 MeV calculations. Here we examine scattering from ^{12}C (4.44 MeV 2^+ and 9.63 MeV 3^- states), ^{28}Si (1.72 MeV 2^+ state), ^{40}Ca (3.74 MeV 3^- state) and ^{208}Pb (2.62 MeV 3^- state). The collective model deformation parameters used were $\beta_2 = 0.60$ for ^{12}C and $\beta_2 = 0.40$ for ^{28}Si as before, and $\beta_3 = 0.44$ [Fri 65] for ^{12}C, $\beta_3 = 0.39$ for ^{40}Ca [Ful 68] and $\beta_3 = 0.12$ for ^{208}Pb [Wag 75]. The results for the π^+ cross sections are given in Figure 4-13. The data for ^{12}C and ^{28}Si are from [Dyt 79], while the elastic data for ^{40}Ca, ^{208}Pb (and some for ^{12}C) come from [Pre 81]. The π^- predictions are shown in Figure 4-14.

The π^+ elastic scattering is quite well reproduced. The only way to improve on these results is to fit the potentials to each target separately. The inelastic data is also well described by these calculations. The two low points for the ^{12}C 3^- state are new [Ama 81] and at very low cross section where it is difficult to extract a peak area from the background. The ^{28}Si 2^+ cross sections are below the measured values as noted at 36 MeV. There is as yet no data for any of the other cases. It should be possible to get data for ^{40}Ca, since the back angle inelastic cross section is comparable to the elastic cross section. The ^{208}Pb inelastic calculation is a factor of 10 below the elastic cross section, so that higher resolution will be required before it can be seen.

The π^- predictions are most interesting. The elastic cross section for ^{12}C is characterized by a change in the interference between

Figure 4-13

Elastic and inelastic scattering of 50 MeV π^+ from ^{12}C, ^{28}Si, ^{40}Ca and ^{208}Pb with parameters from Set C (dashed curve) and Set D (solid curve) as described in the text.

MSUX-81-111

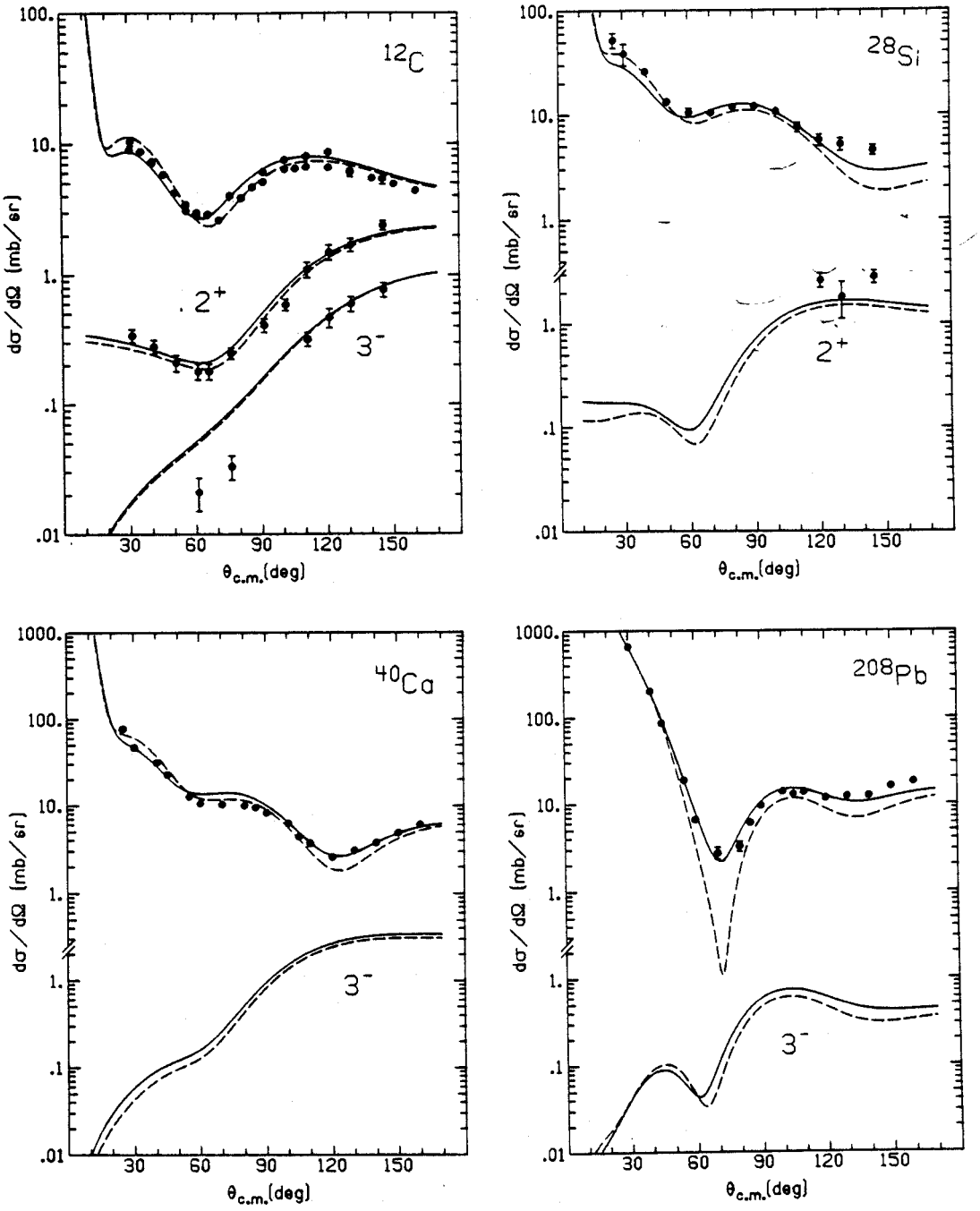

Figure 4-13

Figure 4-14

Same as Figure 4-13, except
calculated for 50 MeV π^- scattering.

MSUX-81-112

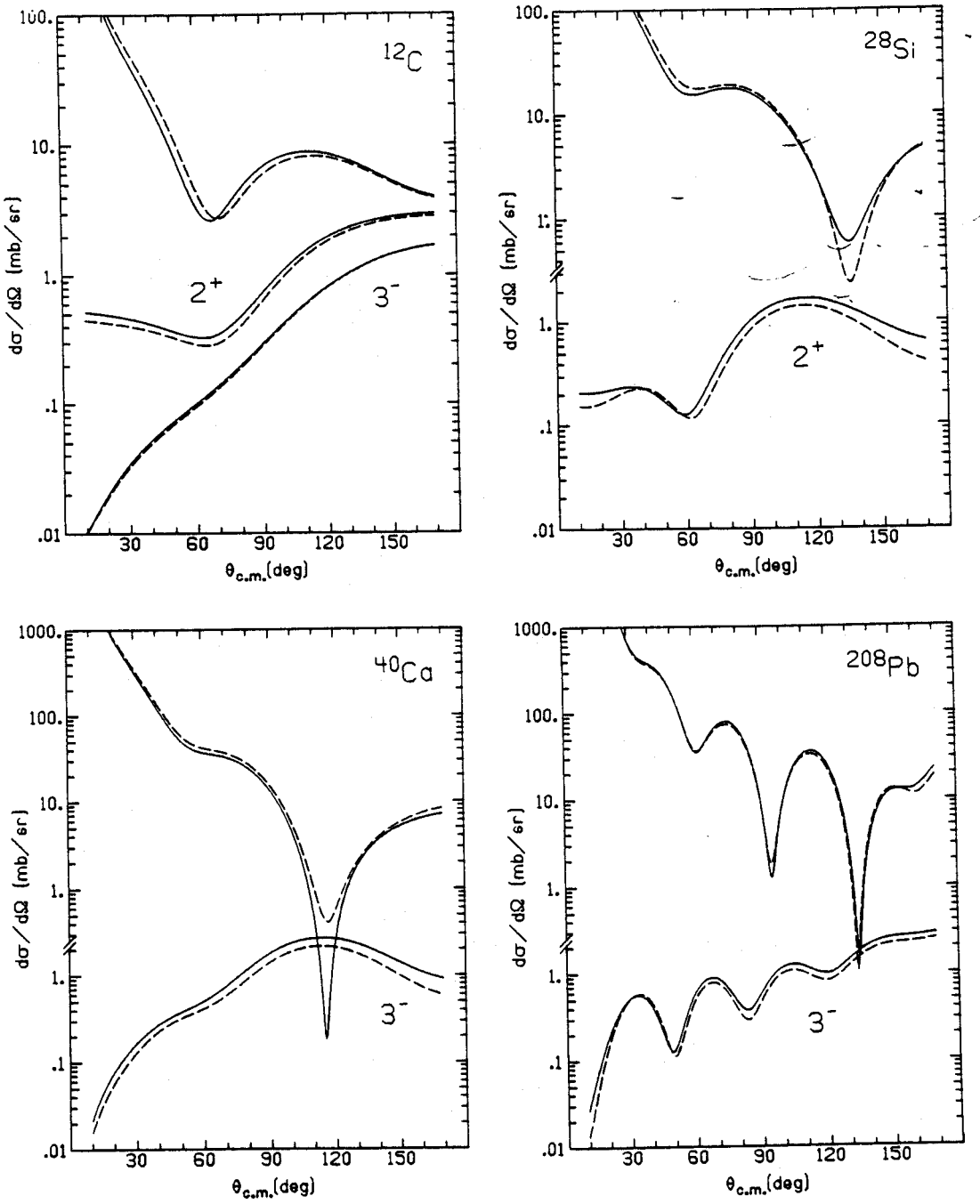

Figure 4-14

the pion-nucleus and coulomb interactions, but as A increases we see diffractive minima come in. The ^{208}Pb calculations almost look as if they were done 70 MeV higher in energy (c.f. Figure 4-19), since they are characterized by a strong diffraction pattern. This was noted several years ago [Str 79], and experiments to examine this prediction have been performed at LAMPF although the results are not yet available. The inelastic predictions follow a similar trend, with the ^{12}C results resembling the corresponding π^+ curves, while the ^{208}Pb calculations are very diffractive.

It should be emphasized that the input for the π^- runs was exactly the same as for π^+, except the pion charge of course. The optical parameters were not changed. The effect that is seen at large A is due to the explicit velocity dependence of the $k \cdot k'$ term in the optical potential. Thus when the π^- is attracted to ^{208}Pb by its large Z, the increased energy is translated into a stronger p-wave attraction/absorption, which leads to a result that resembles scattering at much higher energies. These statements are illustrated in Figure 4-15, which plots $|S_\ell|^2$ for π^+ and π^- scattering from ^{208}Pb for the cases just described. It can be clearly seen that the π^- is more strongly absorbed, leading to the diffractive scattering. Note the similarity of the π^- graph here to the one for 162 MeV π^+ on ^{12}C, given in Figure 4-5, where the resonance dominates the reaction. These predictions of low energy π^- cross sections provide a good test of the choice of this velocity-dependent interaction.

The next case, 67 MeV scattering from ^{12}C, is shown in Figure 4-16. The π^+ data are from LAMPF [Ama 81], while the π^- data are from the old Nevis cyclotron [Ede 61]. The parameters of Set D were fit to the π^+

Figure 4-15

Comparison of $|S_\ell|^2$ for elastic scattering of 50 MeV π^+ (top) and π^- from ^{208}Pb.

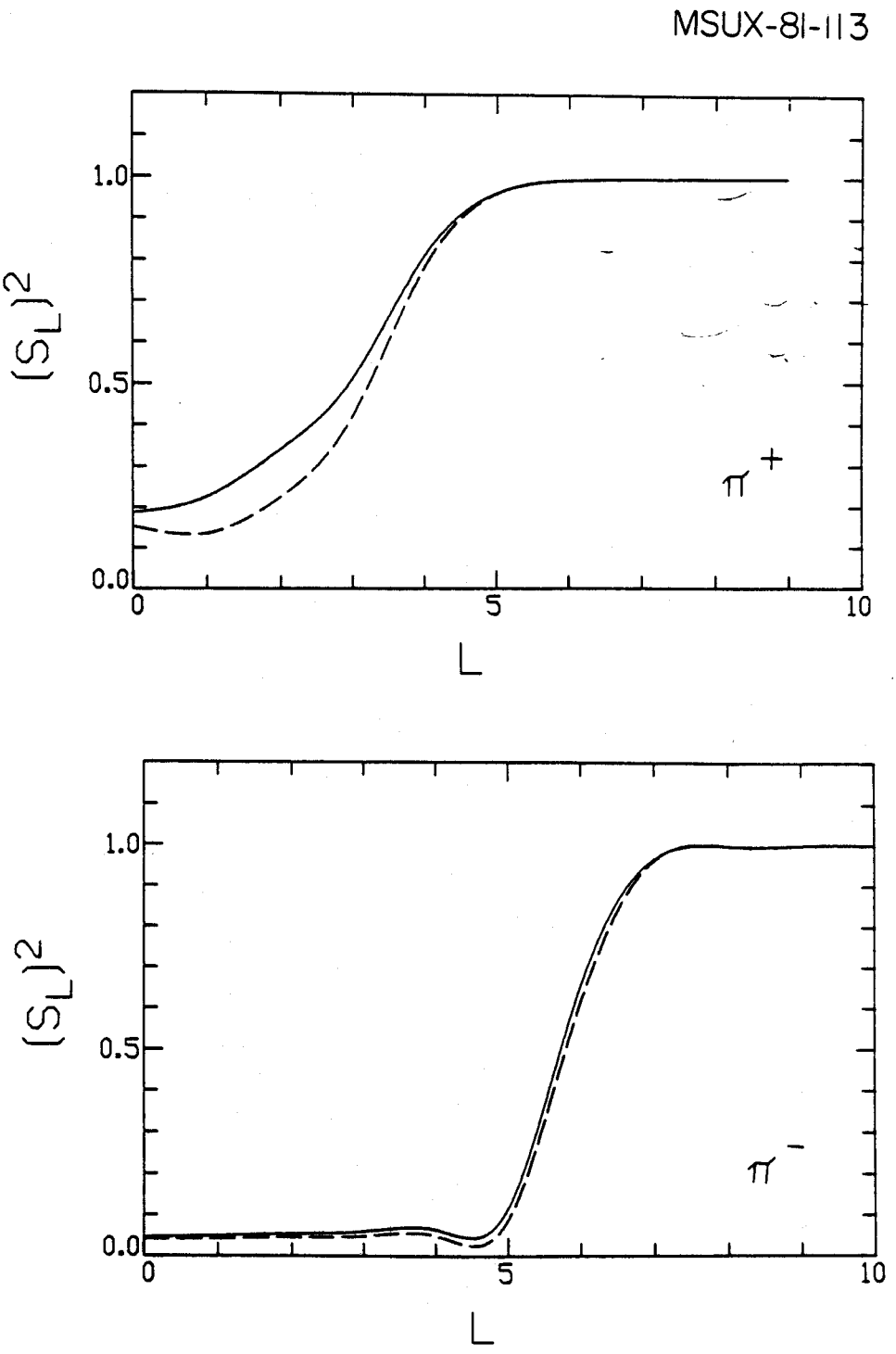

Figure 4-15

Figure 4-16

Elastic and inelastic scattering of 67 MeV π^+ and π^- from ^{12}C using parameters from Set C (dashed curve) and Set D (solid curve) as described in the text.

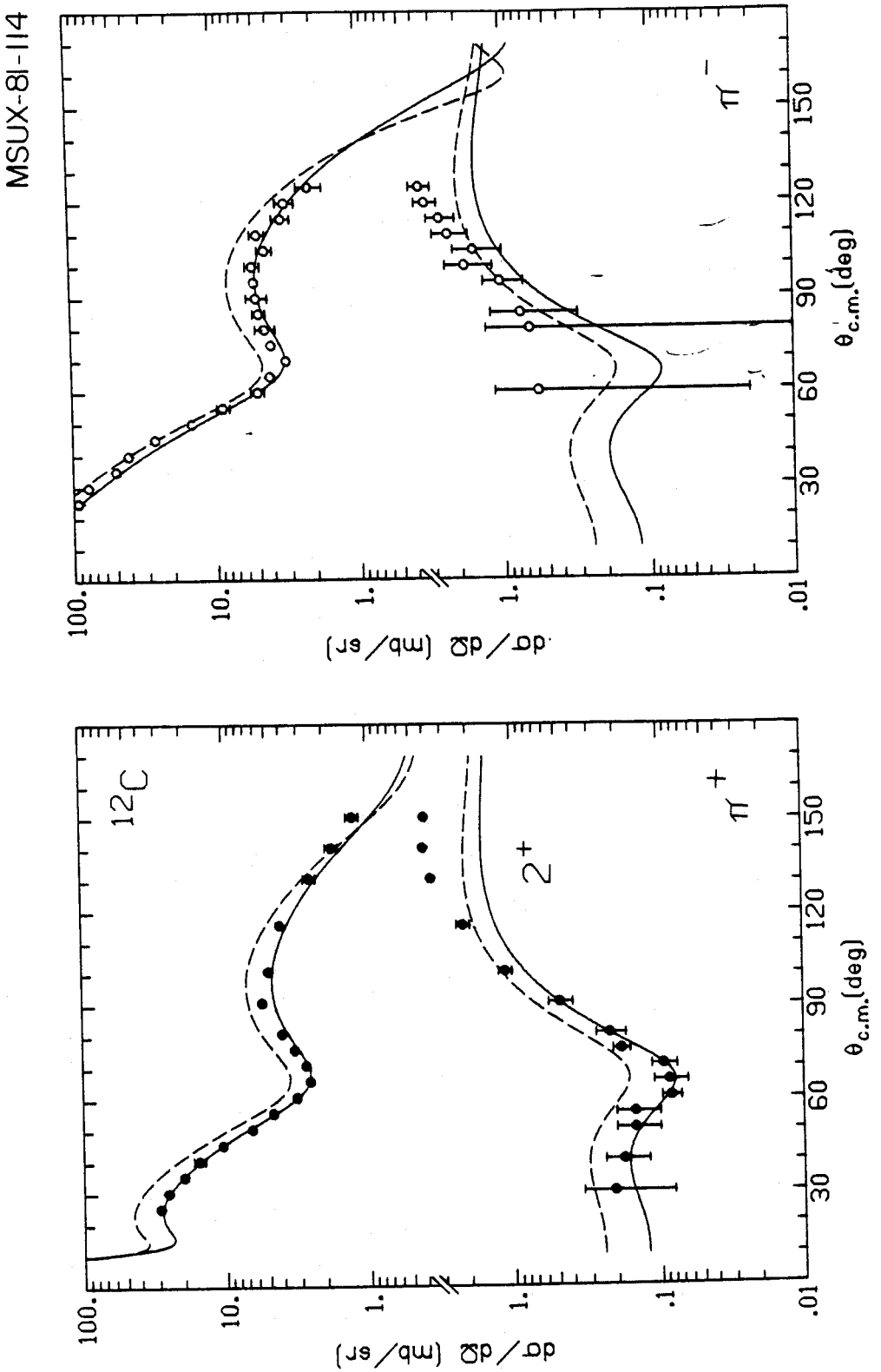
MSUX-81-114
12C
2+
π+
π−
dσ/dΩ (mb/sr)
θc.m.(deg)
100.
10.
1.
.1
.01
30
60
90
120
150

Figure 4-16

data only. The consistency of the results is quite impressive. The elastic cross sections for π^- are fit well by Set D. Both inelastic cross sections rise faster than the calculations until they are a factor of 2 higher at back angles. This deviation at high momentum transfer is not well understood. The authors of [Ama 81] have proposed that coupled channels effects may be important since the inelastic cross section actually dominates for $\theta \geq 130°$. It was also proposed that phase-shift equivalent distorted waves that have very different interior forms can produce this effect [Kei 81]. One can summarize the ideas on this by saying that it could be due to the force, the reaction mechanism, the form factor or the distorting potential choice. Since this effect has appeared just as we enter a previously unstudied region, it is difficult to disentangle these possibilities at this time.

Finally, we turn to the 80 MeV results. These are for ^{12}C (4.44 MeV 2^+ state), ^{40}Ca (3.73 MeV 3^- state), ^{90}Zr (2.75 MeV 3^- state) and ^{208}Pb (2.62 MeV 3^- state). The deformation parameters are the same as quoted earlier, except we now add $\beta_3 = 0.14$ [Hin 73] for ^{90}Zr. The π^+ results are in Figure 4-17, while the π^- results are shown in Figure 4-18. The data are all from [Ble 81], and are preliminary at this time. The calculations are very interesting, which means they do not explain the data.

The π^+ elastic data show a curious trend from ^{12}C, where Set D provides a good fit, to ^{208}Pb where Set C is better. Although Set D was only fit to the first two lobes of the angular distribution, it is surprising to see it do so poorly since this same method works well at higher energy. Perhaps more surprising is that Set D reproduces the π^- data quite well despite the fact it was fit to the π^+ data alone.

Figure 4-17

Elastic and inelastic scattering of 80 MeV π^+ from ^{12}C, ^{40}Ca, ^{90}Zr and ^{208}Pb using parameters from Set C (dashed curve) and Set D (solid curve) as described in the text.

MSUX-81-115

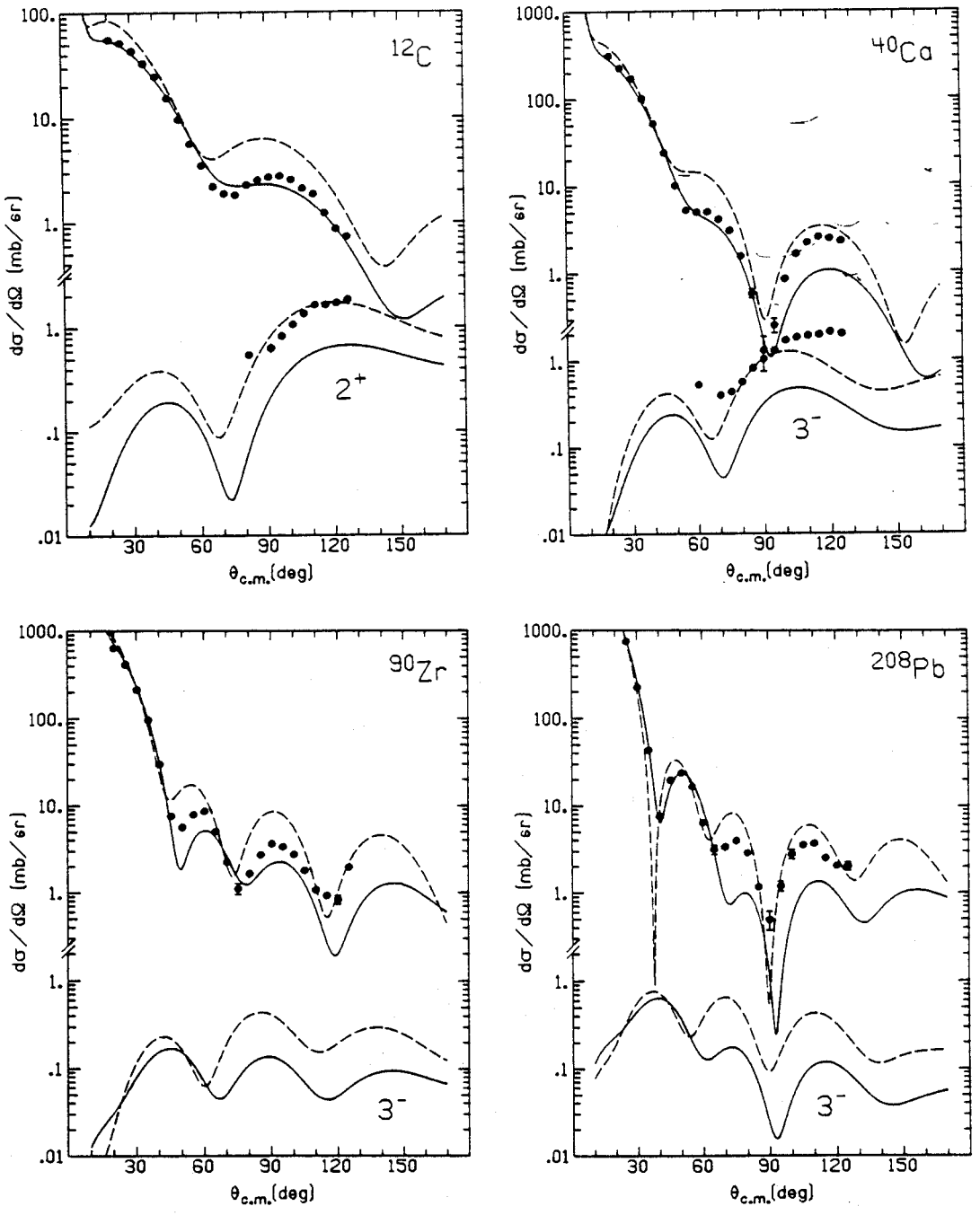

Figure 4-17

Figure 4-18

Same as Figure 4-17, except
calculated for 80 MeV π^- scattering

MSUX-81-116

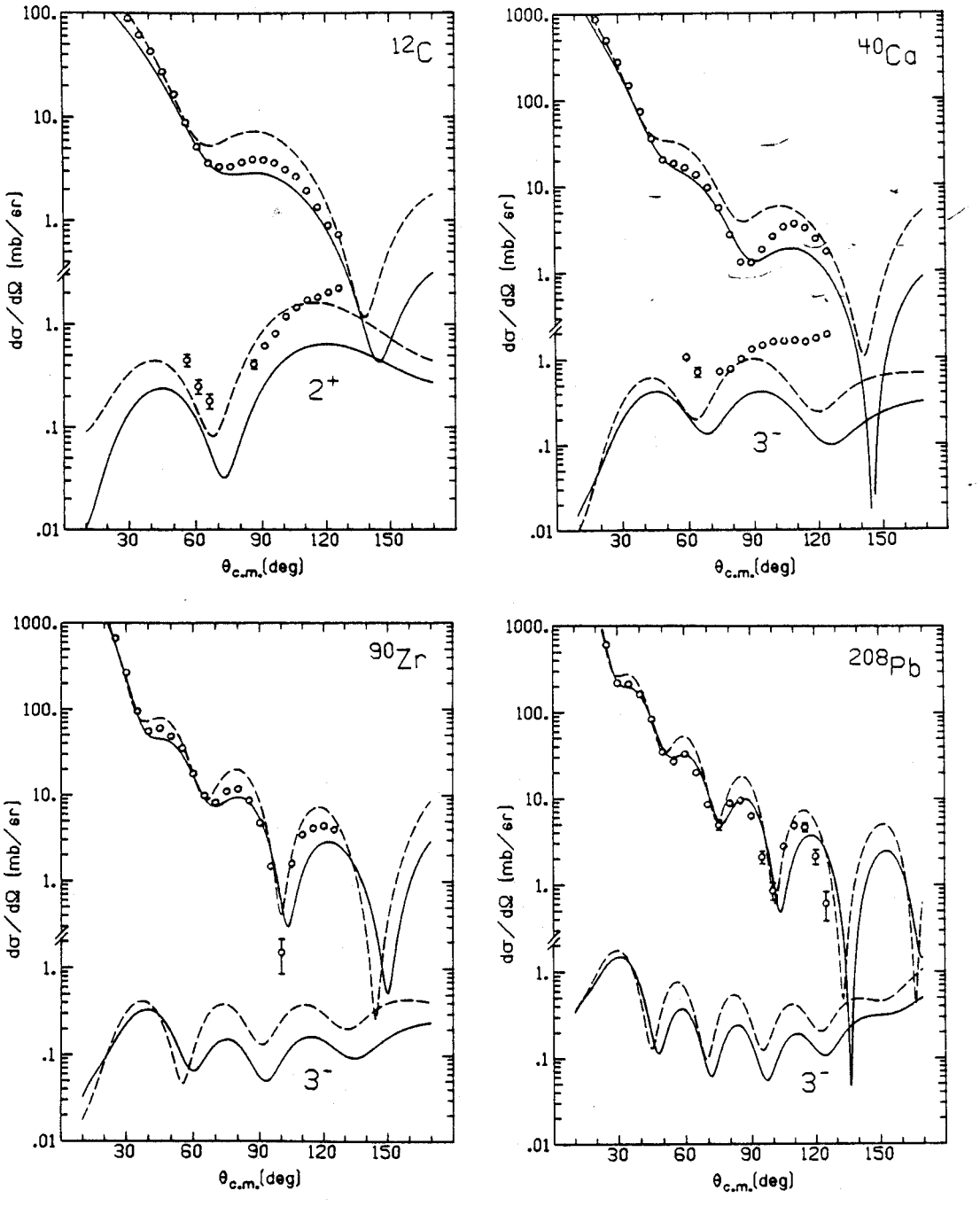

Figure 4-18

The inelastic results have many problems. First, there is an "anticoincidence" between fitting the elastic and fitting the inelastic. An investigation of this showed that 75% of the difference was due to the inelastic scattering t-matrix. These resemble higher energy data in that the large change in distortion only had a small effect. This may suggest that the inelastic data are a sensitive measure of the strength of the interaction. Second, the ^{40}Ca 3^- state is very poorly described. This ^{40}Ca case is rather unique in that we do not reproduce the shape at all. Since we normally get the oscillations right, this may indicate that other parts of the force -- perhaps the normal parity spin-orbit force that we neglected in equation (2-42) or perhaps coupled channels effects -- are contributing here. Finally, these data are preliminary and it is possible that they may be in error.

In summary, the low energy data become increasingly complex as we approach the transition to resonance region scattering. The data at 36 and 50 MeV indicate that the energy dependence of the effective interaction that was used previously [Car 81] does a good job of reproducing the data. The main property of the interaction is the decrease of absorption from the pionic atom value, increase in b_o and a relatively constant value for c_o. The few inelastic cross sections seem consistent with these calculations, but much more remains to be done. The data at 67 and 80 MeV are difficult to interpret. The 67 MeV data are fairly well described by the fitted set, but the back angle inelastic cross section is quite wrong. The 80 MeV data are preliminary, but suggest that the physics gets quite complicated as we approach a region where diffraction (for heavy nuclei) and interferences in the force (for light nuclei) coexist.

4.5 OTHER HIGH ENERGY CASES

This section will review data above 100 MeV. Although elastic scattering has been studied up to very high energies, the existing inelastic data will limit this discussion to 180 MeV at the maximum. This discussion will also use sets C (dashed) and D (solid). The parameters are given in Tables 4-3 and 4-4, respectively. It should be noted that the energy dependence of λ (the LLEE parameter) has been crudely approximated by an abrupt change from 1.6 to 1.0 This made sense when we considered the energy dependence from 50 to 163 MeV, but it does make a comparison of the 80 and 116 MeV sets meaningless and this must be kept in mind.

We begin with 116 MeV calculations for ^{40}Ca (3.72 MeV 3^- state) and ^{208}Pb (2.62 MeV 3^- state). The densities and deformation parameters are as we defined them above. The results are shown in Figure 4-19 with the ^{40}Ca data from [Mor 80] and ^{208}Pb data from [Bos 77].

The agreement between theory and experiment is very good, with the exception of some details of the π^- elastic cross section for ^{208}Pb. It appears that Set C gives the best overall fit as it reproduces the inelastic strengths. We are now in a region where diffraction dominates so that moderate changes in distortion do not affect the inelastic, and the inelastic scattering cross sections give a good indication of the content of the t-matrix.

In contrast to the 80 MeV calculations, these correctly reproduce the ^{40}Ca cross sections. However, these are typical diffractive angular distributions where the first peak is higher than successive ones. This should be contrasted with low energy cross sections which are backward

Table 4-3

Parameter Set C Theory Values
for Resonance Region Scattering

	116 MeV	130 MeV	162 MeV	180 MeV
$\bar{b}_o$	-0.068 +0.019 i	-0.073 +0.023 i	-0.083 +0.029 i	-0.089 +0.034 i
b_1	-0.128 +0.0 i	-0.127 +0.0 i	-0.125 +0.003 i	-0.125 +0.005 i
c_o	0.83 +0.032 i	0.76 +0.045 i	0.37 +0.067 i	0.09 +0.70 i
c_1	0.46 +0.16 i	0.42 +0.22 i	0.21 +0.33 i	0.07 +0.35 i
λ	1.0	1.0	1.0	1.0
B_o	-0.08 +0.22 i	-0.09 +0.23 i	-0.15 +0.28 i	-0.19 +0.30 i
C_o	0.78 +1.64 i	0.93 +1.98 i	1.29 +2.95 i	1.26 +2.88 i

Table 4-4

Parameter Set D Fitted Values
for Resonance Region Scattering

	116 MeV	130 MeV	162 MeV	180 MeV
$\bar{b}_o$	-0.068 +0.019 i	-0.073 +0.023 i	-0.083 +0.029 i	-0.089 +0.034 i
b_1	-0.128 +0.0 i	-0.127 +0.0 i	-0.125 +0.003 i	-0.125 +0.005 i
c_o	0.64 +0.32 i	0.59 +0.45 i	0.45 +0.67 i	0.17 +0.70 i
c_1	0.46 +0.16 i	0.42 +0.22 i	0.21 +0.33 i	0.07 +0.35 i
λ	1.0	1.0	1.0	1.0
B_o	-0.08 +0.22 i	-0.09 +0.23 i	-0.15 +0.28 i	-0.19 +0.30 i
C_o	0.78 +0.16 i	0.93 +0.0 i	1.29 +2.0 i	1.26 +1.6 i

Figure 4-19

Elastic and inelastic scattering of 116 MeV π^+ and π^- from ^{40}Ca (top row) and ^{208}Pb using parameters from Set C (dashed curve) and Set D (solid curve) as described in the text.

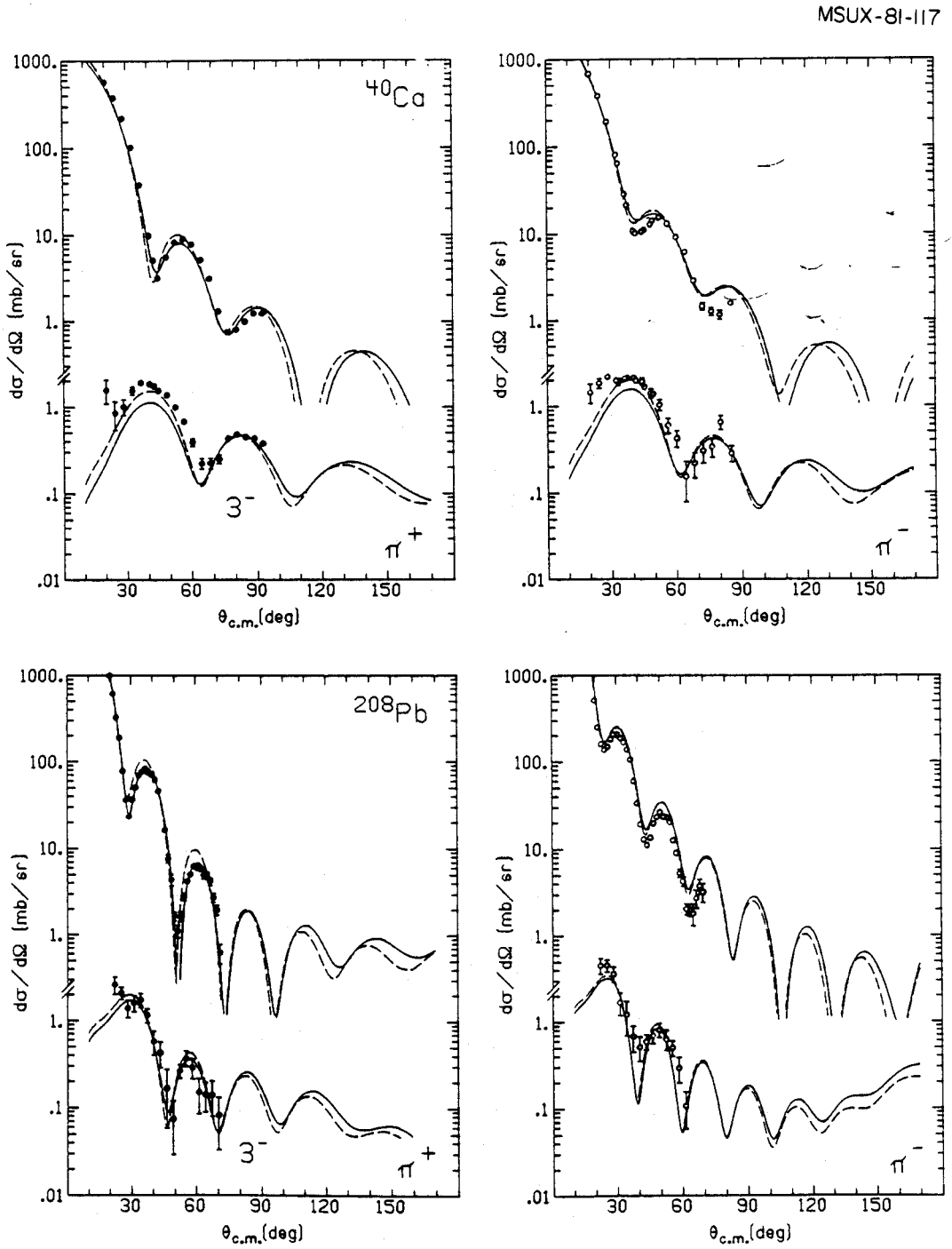
MSUX-81-117
40Ca
208Pb
3-
π+
π-
dσ/dΩ (mb/sr)
θc.m.(deg)
1000.
100.
10.
1.
.1
.01
30
60
90
120
150

Figure 4-19

peaked due to the dominance of p-wave scattering at 180°. The 80 MeV data fall exactly between these two limits, suggesting that the problem at 80 MeV may indeed be our failure to deal correctly with the coexistence of these two phenomena.

The 130 MeV data for ^{28}Si (1.77 MeV 2^+ state) are shown in Figure 4-20. The parameters have been given before, and the data are from [Pre 79]. These data were taken in a spectrometer that had 0.3 MeV resolution, rather than the 1-2 MeV resolution typical on the LEP channel, so we see the inelastic transition quite clearly. The elastic data are extremely well described, but the inelastic calculation is about a factor of 2 low as we saw at low energies.

This difficulty appeared before in an analysis of ^{24}Mg data [Wei 78], but it was resolved [Car 80] with a careful comparison of β_L's from DWBA and CCBA (coupled channels) fits, as well as attention to the βR scaling of the deformation length which is the true measure of the strength of the collective form factor. It was found that the values of β_L typically quoted were from coupled channels calculations. If the corresponding direct reaction value of β is used, the strength of the calculations agreed very well. It appears that the same situation may exist here. An early proton scattering analysis [Cra 67] found $\beta_2 = 0.57$, which would give twice the cross section here. They point out that a coupled channels analysis would give the value of $\beta_2 = 0.40$ that we used here. The analysis of [Pre 79] indicates the same effect: they determine $\beta R = 1.50$-1.55 which corresponds to a value of $\beta \sim 0.53$, producing cross sections that are 1.8 times those computed here. The pion results are consistent with DWBA proton results, which would imply that these pion data are sensitive to the same coupled channels effects,

Figure 4-20

Elastic and inelastic scattering of 130 MeV π^+ and π^- from ^{28}Si using parameters from Set C (dashed curve) and Set D (solid curve) as described in the text.

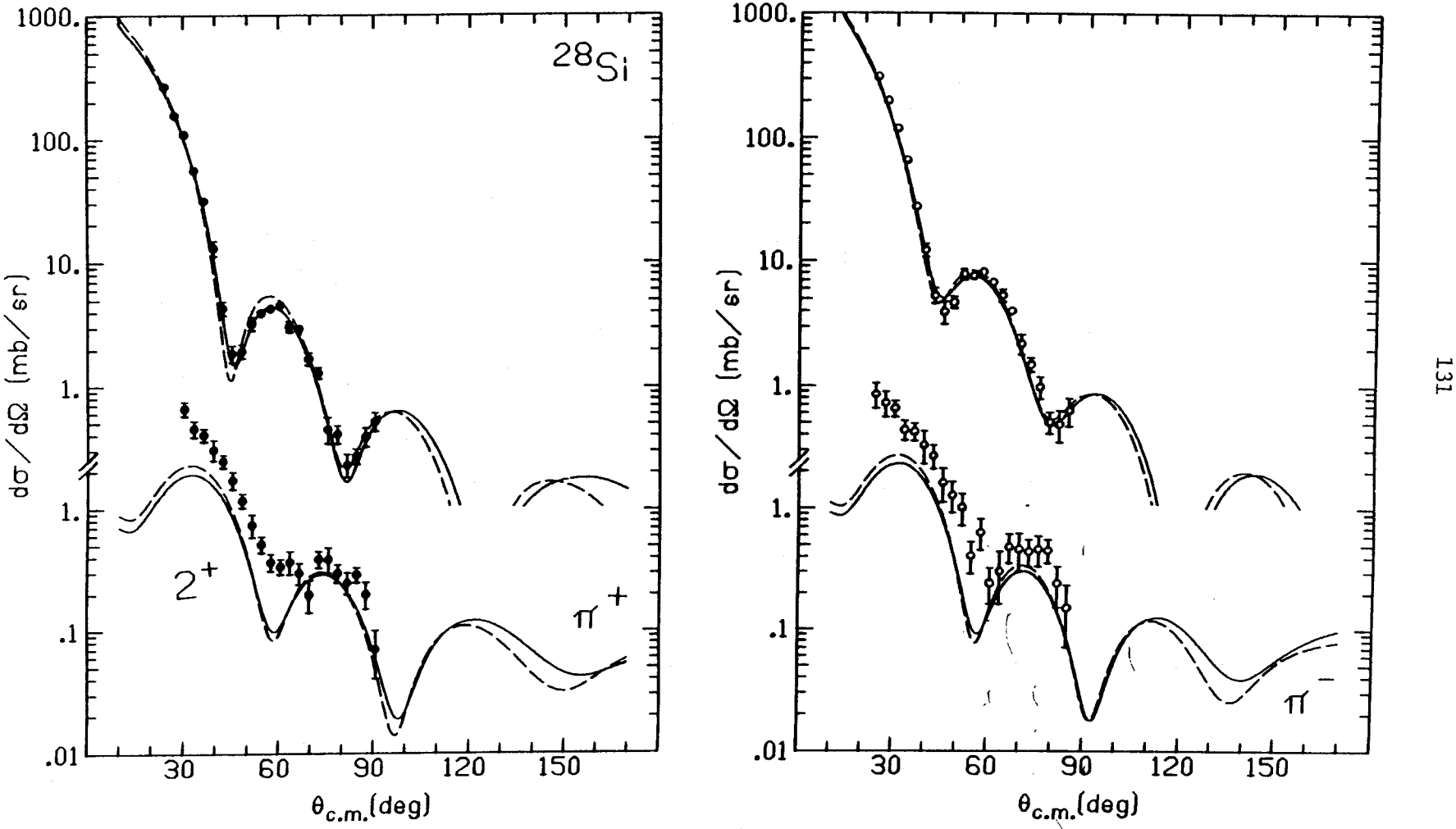

Figure 4-20

and it would be necessary to develop the appropriate codes in order to perform the proper analysis of data like this.

We now return to the 162 MeV data that was examined previously. The calculations and data [Cha 79] are shown in Figure 4-21. The π^+ results have been discussed extensively above, so this will not be repeated here. The main observation is that the π^- results look very much like the π^+; they suffer from the same phase problem relative to the data. The overall agreement is good, with a suggestion that Set C may be better at back angles. There is a possibility of learning more about the density dependence of the interaction from large angle data of this kind.

The final case is shown in Figure 4-22. These 180 MeV data are for ^{28}Si (1.77 MeV 2^+ state) [Pre 79] and ^{40}Ca (3.74 MeV 3^- state) [Mor 80]. The calculations are quite good, with the fitted set (Set D) improving the results in the minima as a result of the decrease in the absorption used. The inelastic data for ^{28}Si are a factor of 2 above the calculations, as explained earlier. The results here look exactly like those at 130 MeV, which shows that the theory has the energy dependence under control in this region. The same is true of the ^{40}Ca data, which is described as well here as it was at 116 MeV.

In summary, the results of these calculations are quite good given that the theoretical underpinnings are poor at these energies. It is particularly interesting that the trends of the data support the use of Riska's absorption values, despite the sometimes unphysical assumptions that enter the calculation. These numbers and the ρ^2 parameterization seem to provide a basic description of most of the data, elastic and

Figure 4-21

Elastic and inelastic scattering of 162 MeV π^+ and π^- from ^{12}C using parameters from Set C (dashed curve) and Set D (solid curve) as described in the text.

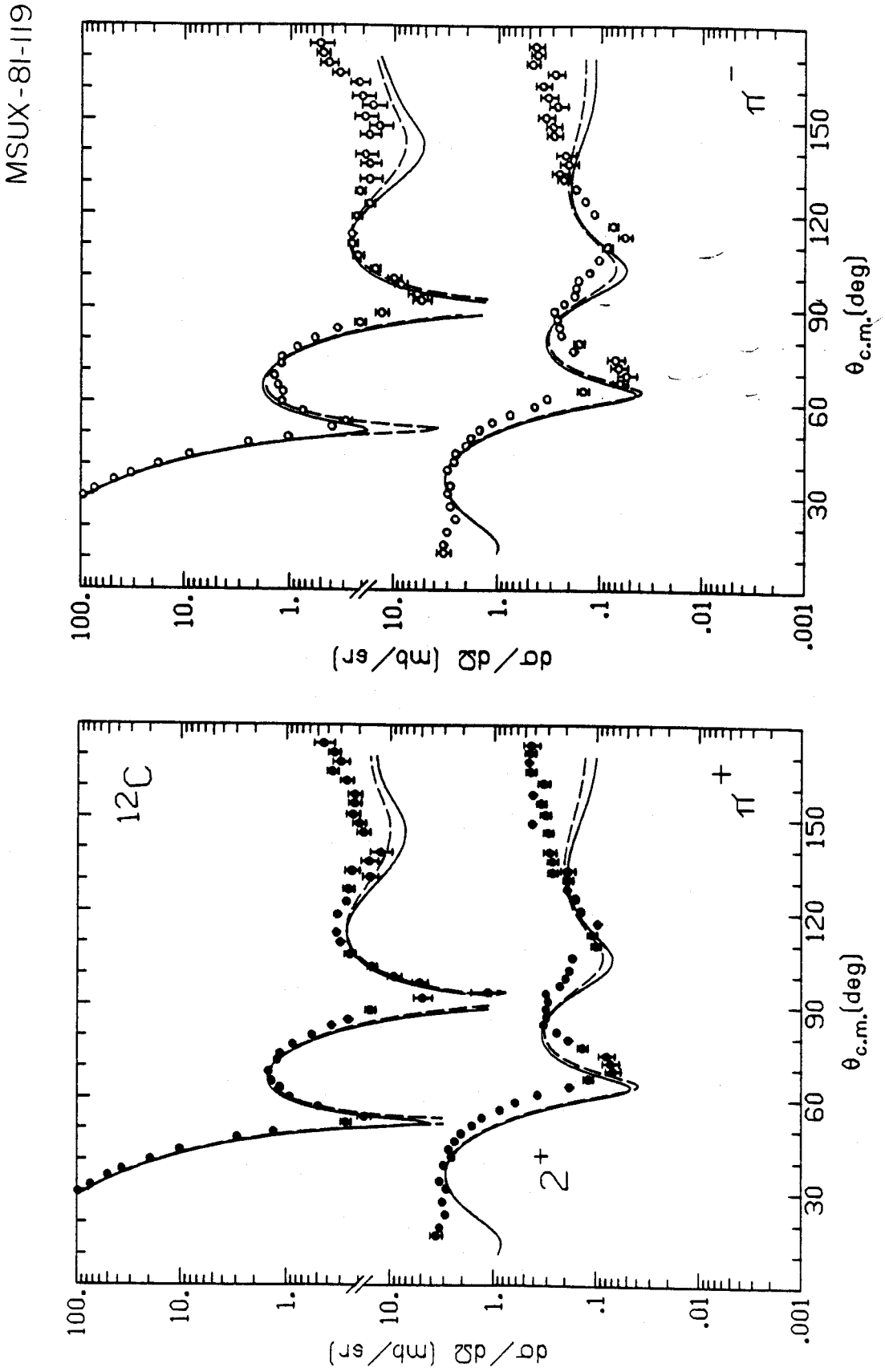
MSUX-81-119
^{12}C
2^+
π^+
π^-
$d\sigma/d\Omega$ (mb/sr)
$\theta_{c.m.}$(deg)
100.
10.
1.
.1
.01
.001
30
60
90
120
150

Figure 4-21

Figure 4-22

Elastic and inelastic scattering of 180 MeV π^+ and π^- from ^{28}Si (top row) and ^{40}Ca using Set C (dashed curve) and Set D (solid curve) as described in the text.

MSUX-81-120

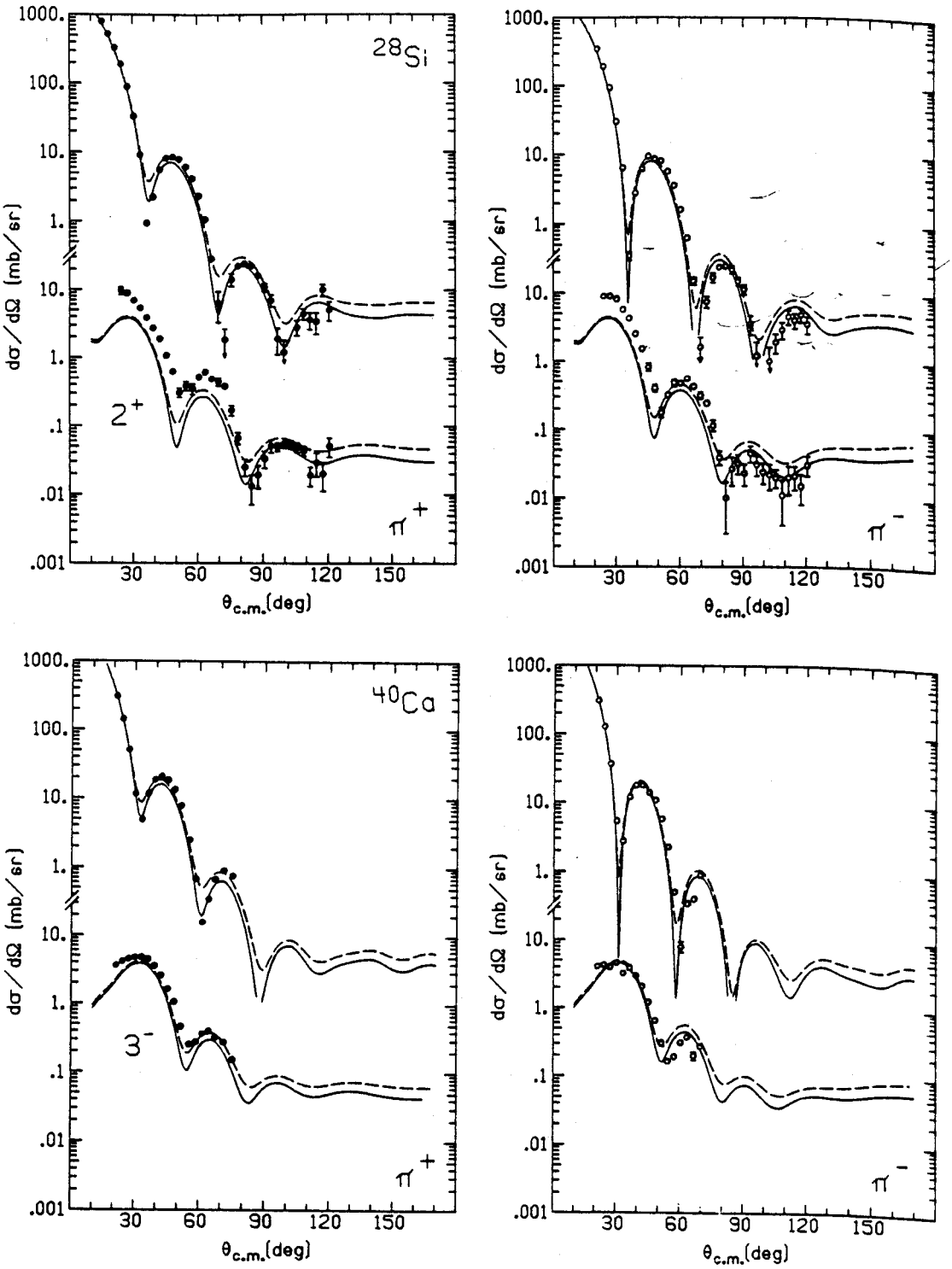

Figure 4-22

inelastic, in this region. There are two areas of difficulty. First, the phase of the angular distributions at 162 MeV are incorrect, while those for neighboring energies are fine. Second, the calculation for the ^{28}Si 2^+ is always low, but this is likely due to a problem in getting the right value of β_L for use in a direct (rather than coupled channels) calculation. Overall, it appears that the optical potentials produce distortions appropriate for these energies, and the inelastic t-matrix is suitable for the analysis of these T=0 transitions.

4.6 SUMMARY

This chapter used the collective model for low-lying T=0 states to illustrate the properties of the pion-nucleus interaction and the effects of the distorting potential on inelastic calculations. A survey of the existing data was then used to gain a perspective on the quality of the fits as a function of energy, and the changes in the importance of various effects as the beam energy nears the Δ-resonance energy.

In Section 4.1 the distorting potential was held fixed so that the properties of the low energy pion-nucleus interaction could be examined without other complications. It was found that a large range of interactions produced equivalent fits, so that it made sense to speak of an effective interaction at these energies. The interactions from elastic scattering fits and multiple scattering theory were similar because they all had enhanced s-wave repulsion and reduced p-wave attraction, as required by the data.

The interaction near resonance was examined in Section 4.2. It was found that the form of the interaction became important, since the full potential produced better results than a four-parameter model which

also fit the elastic scattering. It appears that the density dependence is a major contributor to large angle results.

The effects of distortion were examined in Section 4.3. The inelastic calculations at low energy were found to be sensitive to the choice of optical potential, so that more complete angular distributions would be needed to firmly establish the potential to be used for calculating the distorted waves. Figure 4-5 showed how the low energy potentials had varying amounts of transparency so that the results depended on what parts of the transition density were sampled by the scattered pion. At high energy the potentials all produced a "black" nucleus, and as a result the inelastic calculations were relatively insensitive to the choice of distorting potential.

The remaining sections reviewed the existing experimental situation. It was found that the low ($E_\pi \leq 50$ MeV) and high ($E_\pi \geq 115$ MeV) energy data were well described by both the multiple scattering theory potential (Set C) and the fitted potential (Set D). The exceptions are the ^{28}Si 2^+ state, where the difficulty is associated with the choice of β_L, and 162 MeV scattering, where the calculations are consistently out of phase from the data. The data in the transition region (50 MeV $\leq E_\pi \leq$ 100 MeV) were not as well described by these calculations. There was a problem at backward angles for the excitation of the ^{12}C 2^+ state with 67 MeV pions, but this may be specific to this state. The problems at 80 MeV were more general, since no interaction could fit all of the data. At this point the situation is not very conducive to extracting information about nuclear structure, but should be very useful in understanding the interaction in this region.

CHAPTER 5

MICROSCOPIC MODELS FOR INELASTIC TRANSITIONS

The previous chapter was limited to the consideration of the collective model for the transition density in order to focus attention on the effects associated with various forms of the pion-nucleus interaction. The collective model is also widely used in the literature because the most commonly observed states are easily described in this way. However, states which can be described by a simple shell-model wave function are best studied with microscopic densities. It is this wider class of problems that motivates the examination of these densities.

The first half of this chapter will continue the study of natural parity transitions. Section 5.1 will demonstrate a reasonable ansatz for including density dependent terms when using a microscopic density. It will also examine the effect of changes in the form factor on the calculations, which was omitted from Chapter 4. Section 5.2 will then examine some additional cases of interest. The second half of this chapter will examine unnatural parity transitions. Section 5.3 will outline the way these calculations are done, using the 6^- T=1 state of ^{28}Si as an example. Section 5.4 will examine two other cases of interest at tests of the model.

5.1 COMPARISON OF COLLECTIVE AND MICROSCOPIC MODELS

Before studying particular states, we will first check that we understand how to use a microscopic model with the density dependent interaction used here. The Kuo RPA vector [Kuo] for the ^{40}Ca (3.74 MeV) 3^- state is used in this comparison because it is nearly identical to the collective density we have been using for this state. We will also

examine the effect of using a density which is not the same. For this we will use the Gillet RPA vector [Gil 64] for the ^{12}C (4.44 MeV) 2^+ state, which has a different radial dependence than the collective model density. These configurations and the corresponding parameters of the transition density are given in Table 5-1.

The densities for ^{40}Ca that will be compared are shown in the top half of Figure 5-1. F(r), the radial density defined in equation (3-50), is shown on the left. The solid line is the collective density and the dashed line in the microscopic model given in Table 5-1. On the right side the same conventions are used to show the corresponding electron scattering longitudinal form factor, as defined by equation (E-16) in Appendix E. It can be seen that the densities are very similar in the surface region, and the corresponding charge form factors are nearly identical over the range of momentum transfer that will be important.

The bottom half of Figure 5-1 shows the comparison of the predictions of 50 MeV π^+ inelastic scattering using these densities. In both cases the solid line shows the collective model calculated using Set D. The left side, labeled (a), shows results that use the four-parameter model with Parameter Set A (dash) and B' (dash-dot) so that the microscopic density is included in a natural way. Set A demonstrates the common deficiency of the IA at this energy (an oddly placed minimum) while Set B' produces results that are in good agreement with the standard calculation (Set D had a collective form factor) shown with a solid line. That the small differences are due to the use of a different interaction can be seen in part (b). Here Set C (dash) and Set D (dash-dot) are used with the microscopic density and the ansatz

Table 5-1

Transition Density for ^{40}Ca and ^{12}C

^{40}Ca RPA Vector and Transition Density

Configuration		X	Y
$1f_{7/2}$	$1d_{5/2}^{-1}$	-0.378	-0.201
$1f_{7/2}$	$2S_{1/2}^{-1}$	-0.538	-0.236
$1f_{7/2}$	$1d_{3/2}^{-1}$	-0.736	-0.222
$2P_{3/2}$	$1d_{5/2}^{-1}$	-0.126	-0.085
$2P_{3/2}$	$1d_{3/2}^{-1}$	-0.215	-0.130
$1f_{5/2}$	$1d_{5/2}^{-1}$	0.199	0.107
$1f_{5/2}$	$2S_{1/2}^{-1}$	0.233	0.129
$1f_{5/2}$	$1d_{3/2}^{-1}$	-0.285	-0.163
$2P_{1/2}$	$1d_{5/2}^{-1}$	0.146	0.087

$$(0.707)\ \alpha^3 \left[-1.128(\alpha r)^3 + 0.909(\alpha r)^5\right] e^{-\alpha^2 r^2}$$

$$\alpha = 0.498\ fm^{-1}$$

^{12}C RPA Vector and Transition Density

Configuration		X	Y
$1P_{1/2}$	$1P_{3/2}^{-1}$	0.91	0.05
$1f_{5/2}$	$1P_{3/2}^{-1}$	-0.08	0.06
$1f_{7/2}$	$1P_{3/2}^{-1}$	0.30	0.02
$2P_{1/2}$	$1P_{3/2}^{-1}$	0.11	0.08
$2P_{3/2}$	$1P_{3/2}^{-1}$	-0.12	-0.09
$1d_{3/2}$	$1S_{1/2}^{-1}$	-0.20	-0.14
$1s_{5/2}$	$1A_{1/2}^{-1}$	0.29	0.20

$$(0.707)\ \alpha^3 \left[1.76\ (\alpha r)^2 - 0.057(\alpha r)^4\right] e^{-\alpha^2 r^2}$$

$$\alpha = 0.610\ fm^{-1}$$

Figure 5-1

Radial transition density (top left) and longitudinal form factor (top right) for collective (solid curve) and microscopic (dashed curve) models of the ^{40}Ca (3.74 MeV) 3^- state, the 50 MeV π^+ inelastic scattering calculations at the bottom are described in the text.

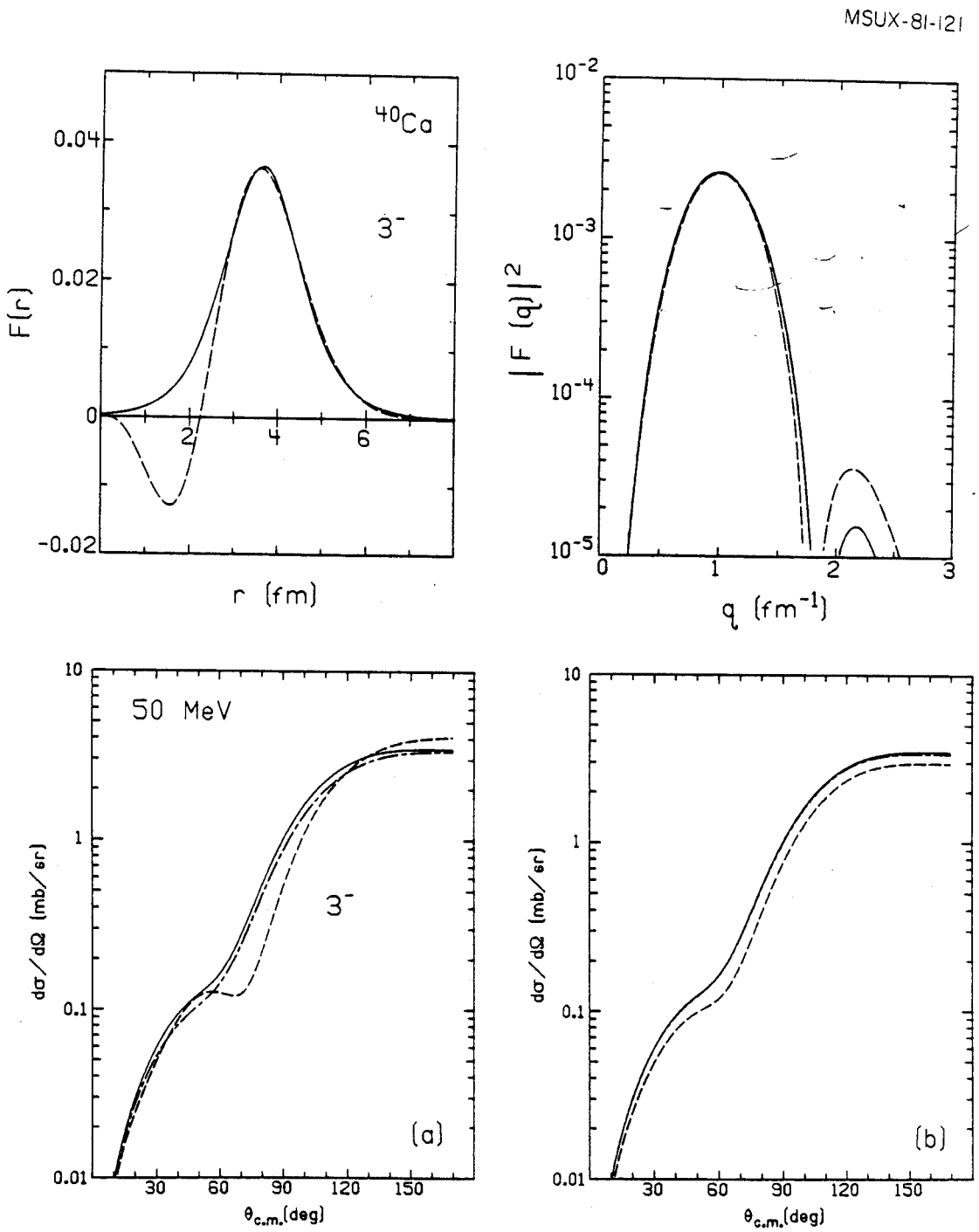

Figure 5-1

of equation (3-61). The results of the calculations with the same force (Set D) and different densities (collective is the solid curve, microscopic is the dash-dot curve) are identical. The result that the effective interaction (B') and the full interaction (D) with this ansatz give comparable results for a microscopic density should be expected, and confirms that this method for including second-order effects in microscopic calculations is a reasonable one.

Additional examples are given in Figure 5-2. The convention at these energies is to use the full potential with theoretical parameters (Set C) for the collective (solid) and microscopic (dash-dot) models to indicate the degree of agreement, and the IA (Set A) with the microscopic density (dash) to show the result with the first-order potential. The data at 116 MeV and 180 MeV [Mor 80] used in Figures 4-20 and 4-22 are used here. The reader may wish to refer back to these to see the effect of using other forces with the collective model. It is observed that the results of the two calculations differ only at large momentum transfer where the two form factors are different. The IA calculation illustrates the sensitivity to the force. Its predictions are reasonable on resonance, as expected, but less adequate at lower energies and/or large momentum transfer. Overall, we see that the microscopic model gives consistent results if it has the same form as the collective density and if we use the same force in the calculation.

The ^{12}C case will show the effects that occur when the form factor has a different shape. The top of Figure 5-3 shows the collective (solid) and microscopic (dashed) form factors as described in Table 5-1. The microscopic density peaks at a smaller radius, and as a consequence

Figure 5-2

Inelastic scattering of π^+ and π^- from the ^{40}Ca 3^- state at 116 MeV (top row) and 180 MeV, using the microscopic density with sets A and C (dashed and dash-dot curves, respectively) and the collective model with Set C (solid curve).

MSUX-81-122

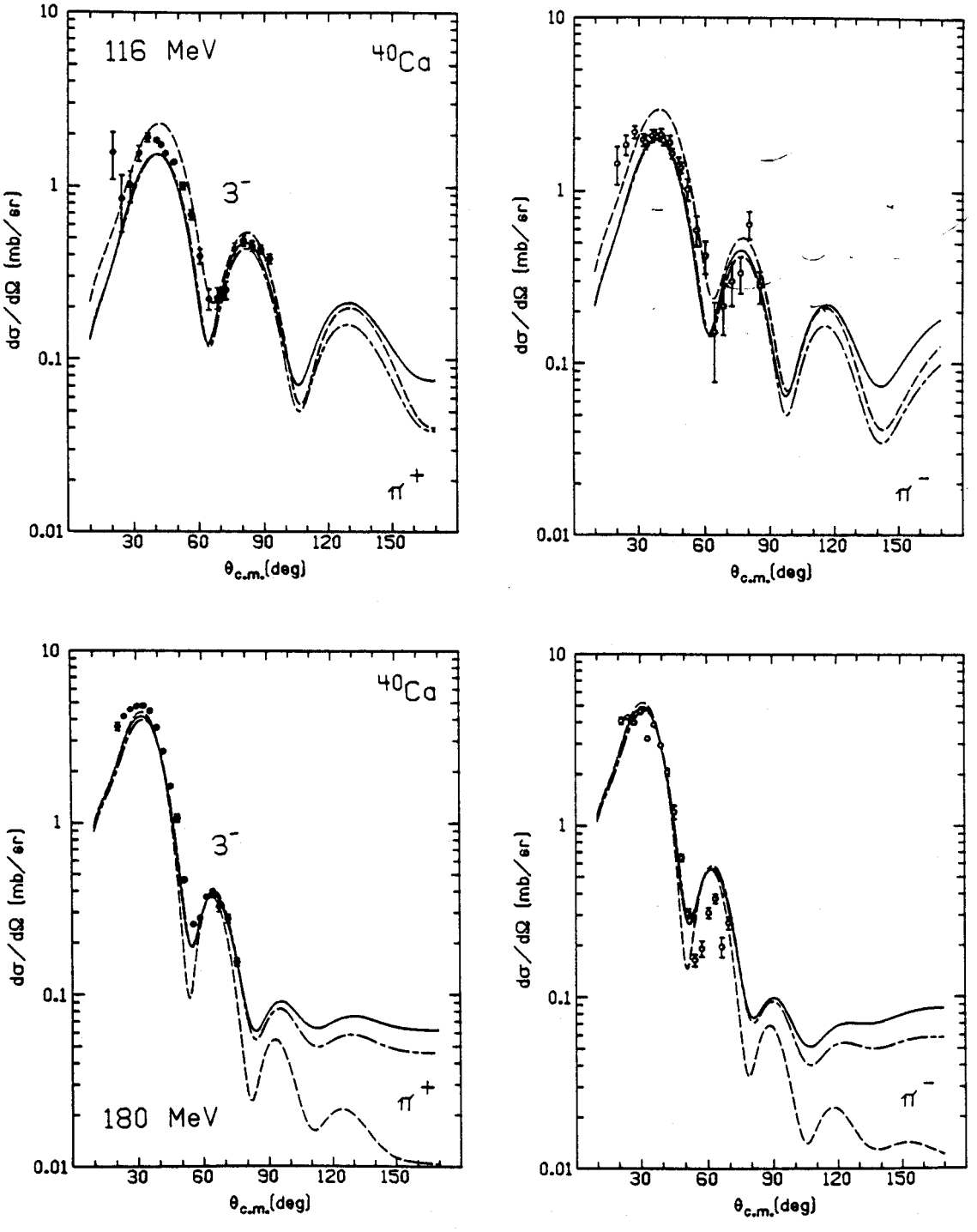

Figure 5-2

Figure 5-3

Radial transition density (top left) and longitudinal form factor (top right) for collective (solid curve) and microscopic (dashed curve) models of the ^{12}C (4.44 MeV) 2^+ state, the 50 Mev π^+ inelastic scattering calculations at the bottom are described in the text.

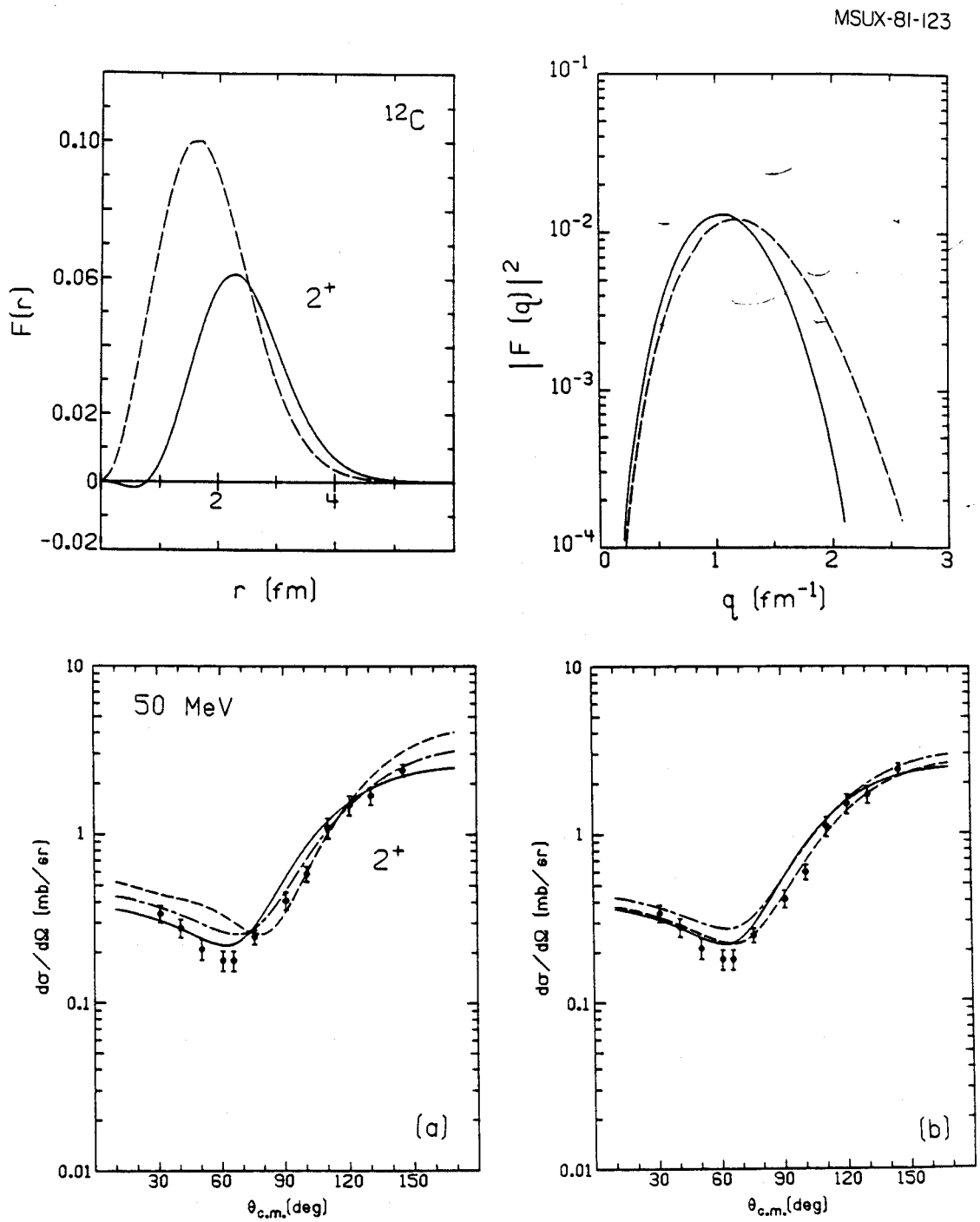
MSUX-81-123
^{12}C
2^+
F(r)
r (fm)
$|F(q)|^2$
q (fm^{-1})
50 MeV
2^+
(a)
(b)
$d\sigma/d\Omega$ (mb/sr)
$\theta_{c.m.}$(deg)

Figure 5-3

the fourier transform peaks at larger momentum transfer. Some of the consequences of this can be seen at the bottom of Figure 5-3, which use the same conventions as in Figure 5-1. Comparing the collective with Set D [solid curve in both parts (a) and (b)] to the microscopic with the effective interaction Set B' [dash-dot curve in part (a)] or the full potential Set D [dash-dot curve in part (b)], we see that the shift in the form factor produces an upward shift in the angular distributions. As before, sets B' and D are roughly equivalent.

Two other cases are shown in Figure 5-4. The 68 MeV calculations use Set D for the collective (solid) and microscopic (dash-dot) runs, with the IA (Set A, dashed) also shown for the microscopic form factor. It is extremely interesting that use of this form factor improves the agreement at large angles. The minimum is not well reproduced, but it would appear that these low energy data are sensitive to high momentum components in the wave function. This is due to the p-wave dominance that causes the scattering to be peaked toward 180°. The data at 162 MeV show that this is not the case at higher energies. Here the strong absorption keeps the distorted waves from seeing most of the transition density (which is deeper inside the nuclear surface than for the collective case) and the cross sections are 30-50% lower for the microscopic case. The calculations here used sets D (solid and dash-dot) and A (dash) in the same conventions as before. Thus this density is clearly not a correct description of this state, but it may indicate that the real form factor has high momentum components that are being seen at low energy.

Figure 5-4

Inelastic scattering of π^+ and π^- from the ^{12}C 2^+ state at 68 MeV (top row) and 162 MeV, using the microscopic density with sets A and C (dashed and dash-dot curves, respectively) and the collective model with Set C (solid curve).

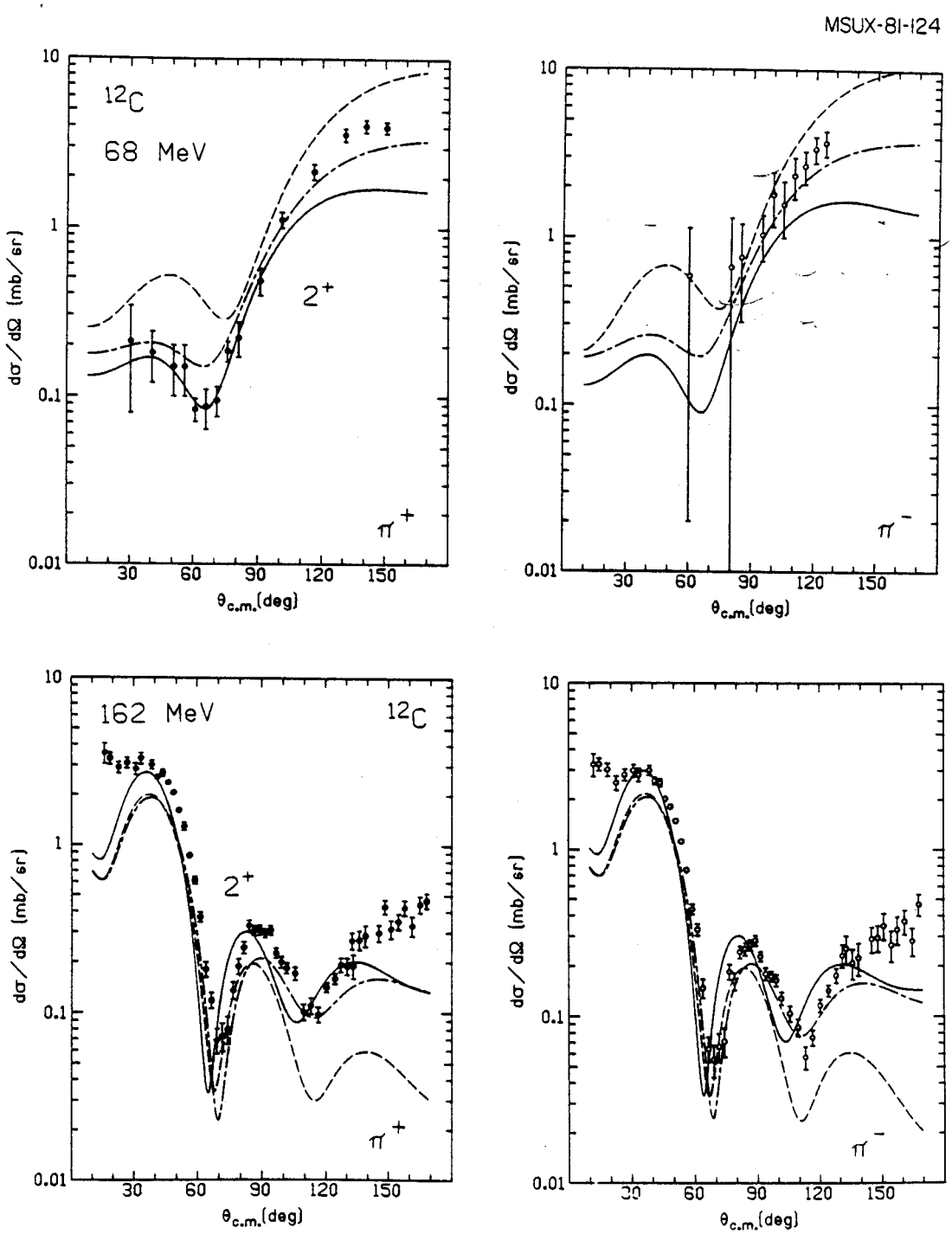
MSUX-81-124
^{12}C
68 MeV
2^+
π^+
π^-
162 MeV
^{12}C
2^+
π^+
π^-
dσ/dΩ (mb/sr)
$\theta_{c.m.}$(deg)
10
1
0.1
0.01
30
60
90
120
150

Figure 5-4

In summary, it is seen that the ansatz we used for including second order effects in the collective model is also appropriate when microscopic models are used. When the densities are the same, the electron scattering and pion scattering predictions are also the same. Differences in the form factor are reflected in the scattering. The low energy potential is transparent, so the distorted waves can probe the higher momentum components of the nuclear wave function. Combined with the dominance of back angle scattering, this makes the cross sections quite sensitive to these changes. The distorting potential is very absorptive at high energies, effectively cutting off any contributions from the parts of the wave function that are inside the strong absorption radius.

5.2 OTHER NATURAL PARITY CASES

There will only be a few cases examined here, but they will serve to illustrate some of the interesting problems currently under study. The first cases are states which should be relatively pure shell-model configurations. The ^{28}Si (9.70 MeV) 5^- T=0 state is predominantly the $1f_{7/2}\, d_{5/2}^{-1}$ [Olm 79] particle-hole state in a "closed" ^{28}Si core. The ^{208}Pb (6.10 MeV) 12^+ neutron state is believed to be a pure excitation of a neutron from the $1i_{13/2}$ to the $1i_{11/2}$ shell-model state [Lic 80]. The final case will use the collective model again to examine the effect of the neutron excess of ^{48}Ca on calculations of scattering to the low-lying collective state.

The results for the ^{28}Si 5^- state are shown in Figure 5-5. At the top is the electron scattering data from [Yen] compared with the

Figure 5-5

Longitudinal form factor (top) and 162 MeV π^+ and π^- inelastic scattering from the ^{28}Si (9.70 MeV) 5^- state with the two form factors described in the text.

MSUX-81-125

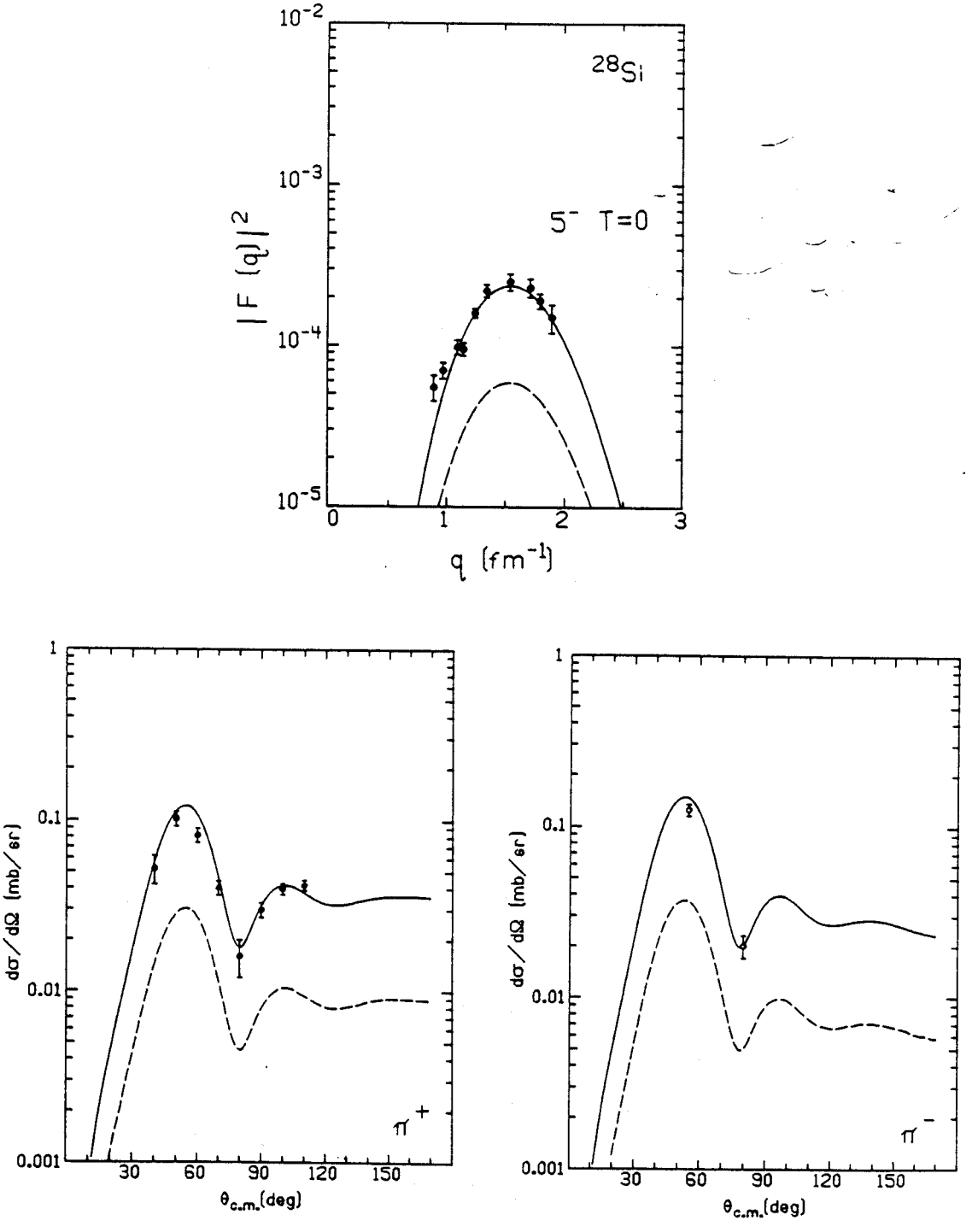

Figure 5-5

longitudinal form factor calculated with a 0.7 $(f_{7/2}\ d_{5/2}^{-1})$ wave function (dashed curve). The solid curve is the result for a 1.4 $(f_{7/2}\ d_{5/2}^{-1})$ wave function. This latter case is not unreasonable because a small admixture of the $f_{5/2}\ d_{5/2}^{-1}$ configuration would produce the same enhancement. Such a mixture can result from a TDA calculation where the Hamiltonian resulting from the use of the KK [Kal 64] or Elliott [Ell 68] force is diagonalized. The densities that result are given in Table 5-2, for comparison with the ones used in these calculations.

The pion scattering results at 162 MeV are shown in the bottom half of Figure 5-5 compared to the data of [Olm 79]. Both calculations use Set D, the curves correspond to the two form factors shown above. The agreement is quite good -- the strengths of the electron and pion scattering seem to be described in a consistent fashion. The dearth of negative pion data is due to the low beam flux and correspondingly long runs necessary to accumulate good data.

The results for the ^{208}Pb 12^+ state are shown in Figure 5-6. The electron scattering results indicate that this transition is a pure neutron state [Lic 80] with about 40% of the strength seen. However, since there are no pion data yet available, the form factors here assume 100% of the strength to facilitate scaling the results when the data are analyzed. Since this is a pure neutron state the charge form factor vanishes; the transverse electric form factor is plotted at the top in the convention given in Appendix E. The pion scattering results use Set D (solid) and Set A (dashed). The two results are quite different because scattering from a neutron is governed by a combination of the T=0 and T=1 interactions, and only the T=0 interaction includes the

Table 5-2

Transition Densities for ^{28}Si 5^- State

	$f_{7/2}\ d_{5/2}^{-1}$	$f_{5/2}\ d_{5/2}^{-1}$	Transition Density (α = 0.524)
Dashed curve	0.7	0.0	$(0.707)\ \alpha^3\ \ 0.0925\ (\alpha r)^5\ \ e^{-\alpha^2 r^2}$
Solid curve	1.4	0.0	$(0.707)\ \alpha^3\ \ 0.185\ (\alpha r)^5\ \ e^{-\alpha^2 r^2}$
TDA calculation (KK force)	0.981	-0.193	$(0.707)\ \alpha^3\ \ 0.168\ (\alpha r)^5\ \ e^{-\alpha^2 r^2}$
TDA calculation (Elliot force)	0.964	-0.265	$(0.707)\ \alpha^3\ \ 0.181\ (\alpha r)^5\ \ e^{-\alpha^2 r^2}$

Figure 5-6

Transverse electric form factor (top) and 162 MeV π^+ and π^- inelastic scattering from the ^{208}Pb (6.10 MeV) 12^+ pure neutron state using Set A (dashed) and Set D (solid curve) parameters.

MSUX-81-126

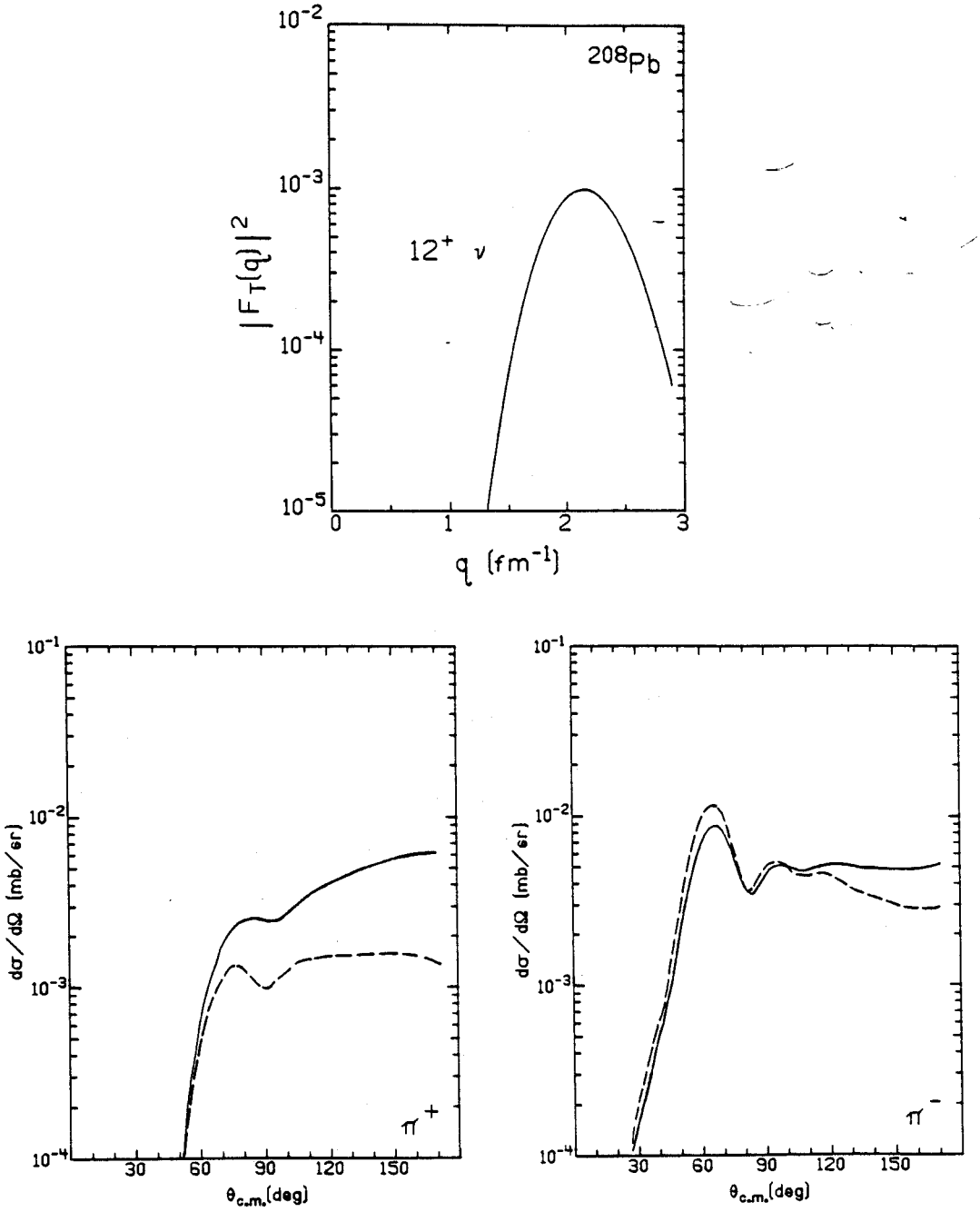

Figure 5-6

second order absorption corrections. The IA calculations give a ratio of 9.2 to 1 (π^-/π^+) at the first peak, in accord with the expected ratio of 9:1 that would result from the P_{33} channel alone. The results with Set D only give 3.6 to 1, showing that the results are very sensitive to the density dependent corrections to the isoscalar interaction. Study of reactions involving neutron or T=1 states with normal parity will contribute a great deal to knowledge of the isovector interaction.

A related problem is the description of the systematic changes that result as neutrons are added to a T=0 nucleus like ^{40}Ca. We have already seen the prediction for 180 MeV scattering from ^{40}Ca (3^-) in Figure 4-22. The top half of Figure 5-7 shows the corresponding predictions for the ^{48}Ca (3.83) 2^+ state along with the elastic scattering results. The curves use Set D (solid) and Set C (dashed) as in Figure 4-22. The agreement is remarkably good; the shift of the ^{48}Ca π^- data towards forward angles is correctly reproduced. The lack of a minimum in the inelastic data is the major defect. Reference to Figure 4-22 shows that the ^{48}Ca data is better explained than the ^{40}Ca data, since there is too much of a shift of the π^- calculation, especially in the inelastic case. This difficulty is clear in the direct comparison of π^+ (solid) and π^- (dashed) calculations in the bottom half of Figure 5-7, where the excessive shift for ^{40}Ca is easily seen. This problem may originate in the interplay between the coulomb potential and the velocity dependent p-wave interaction (noted earlier for 50 MeV π^- scattering), but it must be understood before conclusions can be reached about the neutron components in these wave functions.

Figure 5-7

The top row shows elastic and inelastic scattering of 180 MeV π^+ and π^- from ^{48}Ca and its 3.83 MeV (2^+) state with Set C (dashed) and Set D (solid curve), the bottom row compares 180 MeV π^+ (solid curve) and π^- (dashed curve) scattering from ^{40}Ca (3^-) and ^{48}Ca (2^+) with Set D.

MSUX-81-127

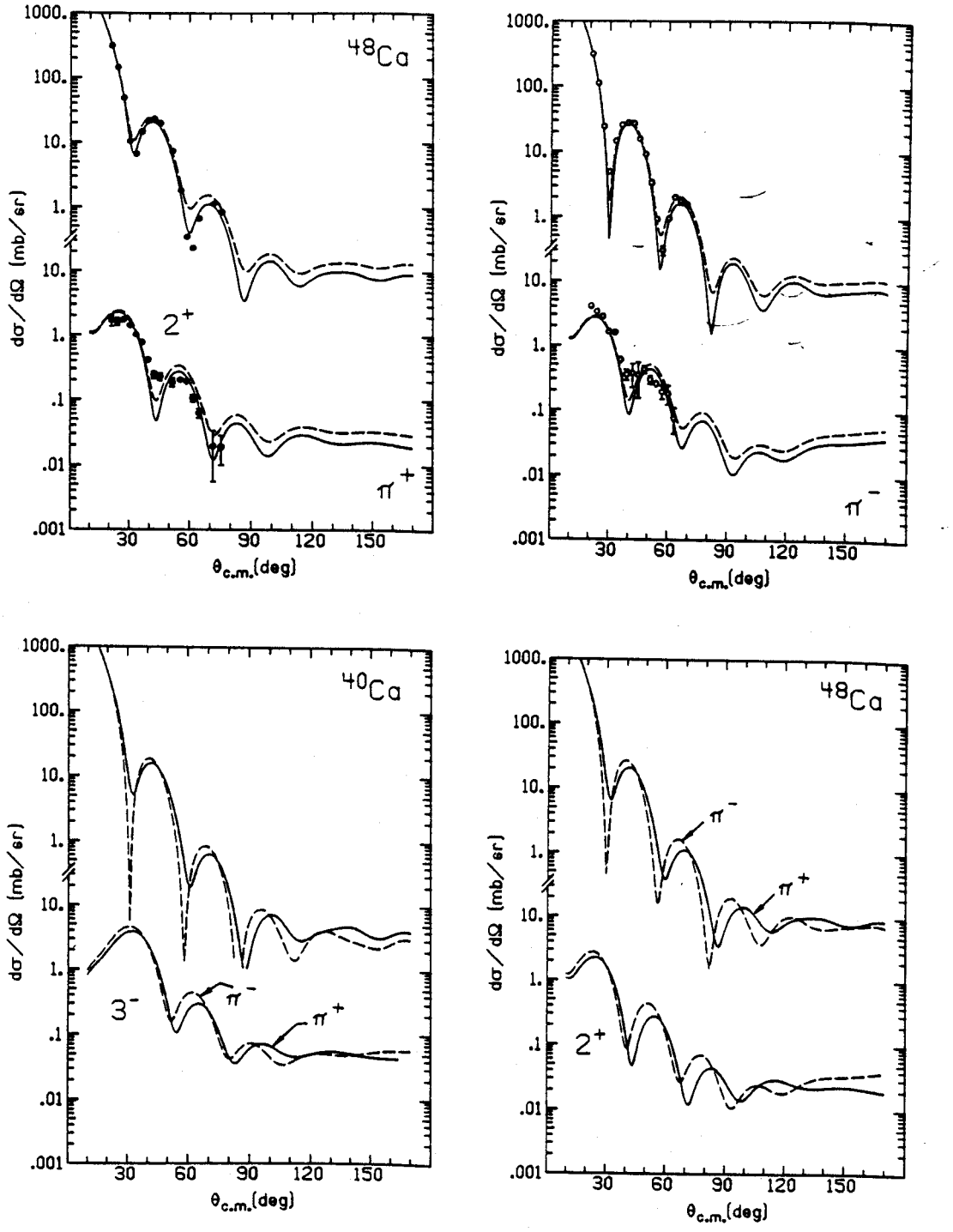

Figure 5-7

In summary, a few applications of microscopic densities to natural parity transitions have been shown. The 5^- case illustrates how this method can be applied, while the ^{208}Pb 12^+ shows how one may learn more about the interaction from an investigation of transitions of this type. Results comparing ^{40}Ca and ^{48}Ca states showed the difficulty in interpreting the origins of differences in the cross sections.

5.3 UNNATURAL PARITY TRANSITIONS

States which have a "stretched" configuration have come under a great deal of study lately. These are states for which the particle and hole come from different major shells but have $j = \ell + 1/2$, so when coupled to the maximum total J they have J = L+1. These S=1 transitions can only be produced by the spin-orbit part of the pion-nucleus interaction, and thus test this part of the potential. The 6^- T=1 state in ^{28}Si at 14.36 MeV excitation has been very heavily studied with a number of different reactions and thus provides a good testing ground where uncertainties in the wave function can be minimized.

First, however, we will give a short review of the method and force used for this calculation. Appendix E outlines the folding model for both central and spin-orbit forces. The essential results for the spin-orbit force are given in equations (3-64), (3-72) and (3-73). The former leads to a recoupling in the distorted waves to reflect the S=1 nature of the transition, while the latter two show how the force parameters found in Chapter 2 are used in obtaining the form factor. Table 5-3 summarizes representative values of the spin-orbit parameters, which were previously plotted in Figure 2-1.

Table 5-3

Spin-Orbit Parameters from
Rowe, Salomon and Landau

	50 MeV	100 MeV	162 MeV	180 MeV
s_o	0.49 +0.044 i	0.51 +0.19 i	0.24 +0.48 i	0.098 +0.47 i
s_1	0.22 +0.22 i	0.25 +0.094 i	0.14 +0.24 i	0.69 +0.23 i

The 6^- T=1 state in ^{28}Si was first observed with electron scattering [Don 70]. Analysis of these data would indicate that 59% of the $f_{7/2}\, d_{5/2}^{-1}$ configuration was seen. Since this is the only particle-hole combination that can produce J=6 unless one goes up to 3 $\hbar\omega$ excitations, it was assumed to be a pure configuration. More recently, it has been seen with inelastic proton scattering [Ada 77] with an angular distribution which supported this spin assignment. New electron scattering data, taken with high resolution, indicate that only 33% of the particle-hole strength is seen [Yen 80]. This will be the figure adopted for this state. The proton scattering data, analyzed in a consistent fashion, suggest only 29% [Pet 80], but there are uncertainties in the choice of the nucleon-nucleon interaction force. Resonant proton scattering from ^{27}Al give a width for this state which is consistent with a number between these two [Hal 81].

The electron scattering data are shown at the top of Figure 5-8, along with the transverse magnetic form factor calculated from the $\sqrt{0.33}\ (f_{7/2}\, d_{5/2}^{-1})$ wave function and $\alpha = 0.524$. The agreement is

Figure 5-8

Transverse magnetic form factor (top) and 162 MeV π^+ and π^- inelastic scattering from the ^{28}Si (14.36 MeV) 6^- state with the force and microscopic form factor described in the text.

MSUX-81-128

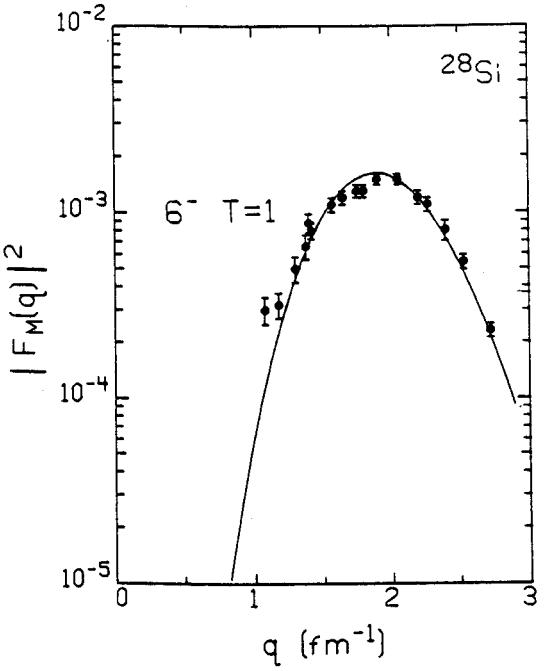

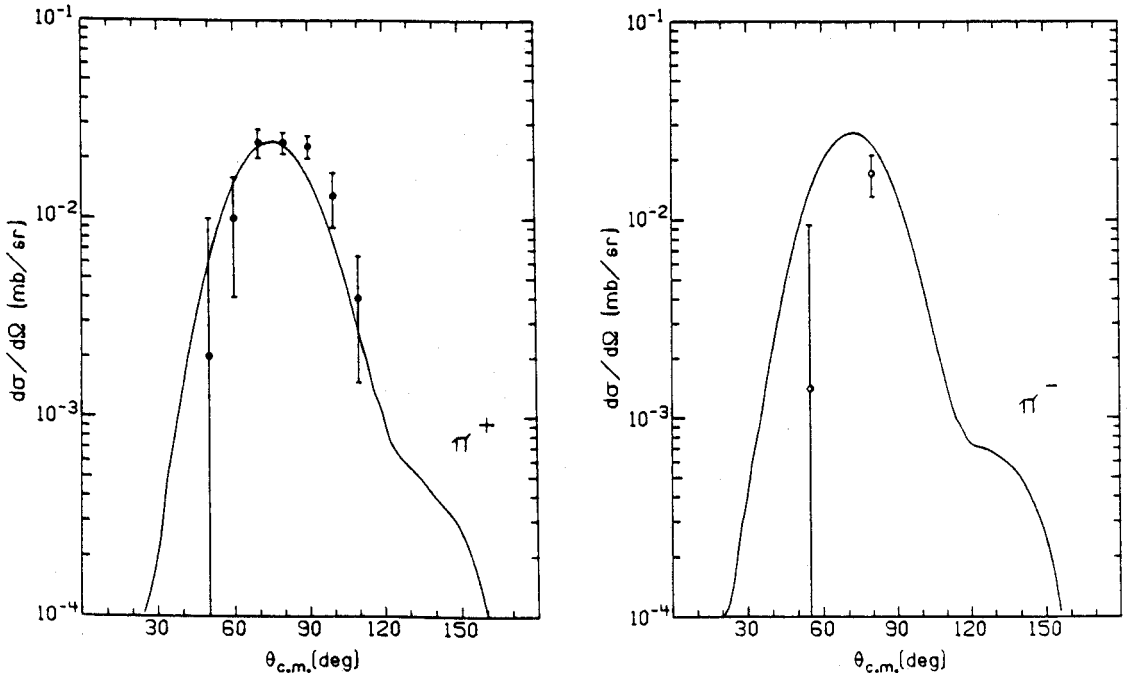

Figure 5-8

quite good. The bottom half of this figure shows the 162 MeV pion scattering data [Olm 79] compared to a calculation assuming the same wave function and the force tabulated above. This calculation agrees well with the π^+ data, but seems systematically higher than the sparse π^- data. The π^+ would also seem to prefer a form factor that peaked at higher momentum transfer, but the overall agreement supports the use of this parametrization of the force.

In summary, the calculations of pion scattering to an unnatural parity state using the IA value of the parameters, the lab to center-of-mass transformation and the folding model are in agreement with that data when the wave function determined by electron scattering is used. A number of experiments suggest that the wave function is well known, but the absolute uncertainty of 20% in the pion experiments makes a firm conclusion about the spin-orbit interaction impossible. Only the accumulation of more data, some of which is in the next section, will allow a better understanding of what the effective strength of this interaction must be.

5.4 OTHER UNNATURAL PARITY CASES

There are a large number of experiments currently being performed to study other unnatural parity transitions, as well as to study the ones described here at other energies. However, the available data is still quite limited and so only two other cases will be examined here. We will first look at the ^{12}C 1^+ T=1 state (at 15.11 MeV), and then at the isospin mixed 4^- states in ^{16}O.

The ^{12}C 1^+ T=1 state has been heavily studied because of its importance in predictions of pion condensates and pre-critical opalescence

phenomena. Thus there is a large amount of new, accurate data from electron scattering. These data [Che 73, Fla 79, Neuh] are shown in the top half of Figure 5-9. The curve drawn there is a calculation of the transverse magnetic form factor calculated from the RPA form factor of Gillet [Gil 64] scaled by $S^2 = 0.27$. These parameters are given in Table 5-4. The differences at large momentum transfer are common to all shell model descriptions, and are the focus of the discussions concerning pion condensation [Tok 80, Del 81]. Since the pion scattering data do not yet reach large momentum transfer, such results do not influence the results we will examine.

The results of a calculation of the pion cross section is shown in the bottom half of Figure 5-9. The density used was the same as for the electron scattering calculation, and the pion interaction used was the same as before except that this calculation was for 180 MeV. The parameters were given in Table 5-3. Agreement is fair, but the data [Mor 80] have large uncertainties. The calculation could be low by as

Table 5-4

Transition Density for ^{12}C 1^+ State

Configuration		X	Y
$1P_{1/2}$	$1P_{3/2}^{-1}$	1.00	-0.06
$1f_{5/2}$	$1P_{3/2}^{-1}$	0.02	0.01
$2P_{1/2}$	$1P_{3/2}^{-1}$	-0.06	-0.01
$2P_{3/2}$	$1P_{3/2}^{-1}$	-0.06	-0.01
$2S_{1/2}$	$1S_{1/2}^{-1}$	0.01	0.01
$1d_{3/2}$	$1S_{1/2}^{-1}$	-0.02	-0.01

Scaled by $S = 0.522$ $(S^2 = 0.27)$

Figure 5-9

Transverse magnetic form factor (top) and
180 MeV π^+ and π^- inelastic scattering from the
^{12}C (15.11 MeV) 1^+ state, as described in the text.

MSUX-81-129

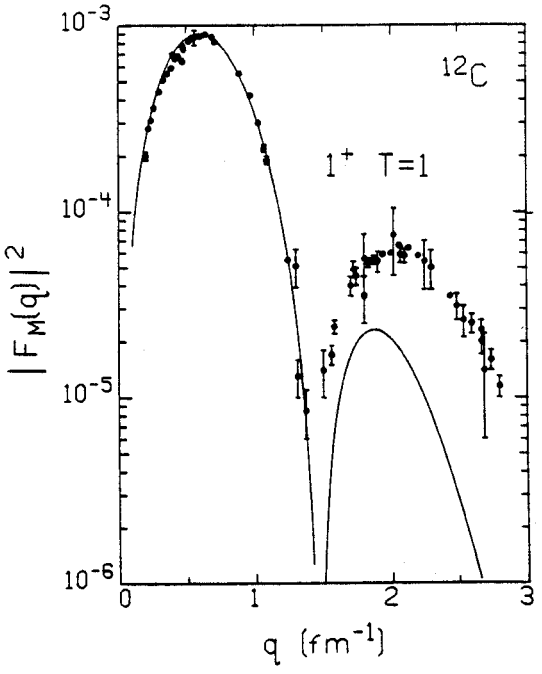

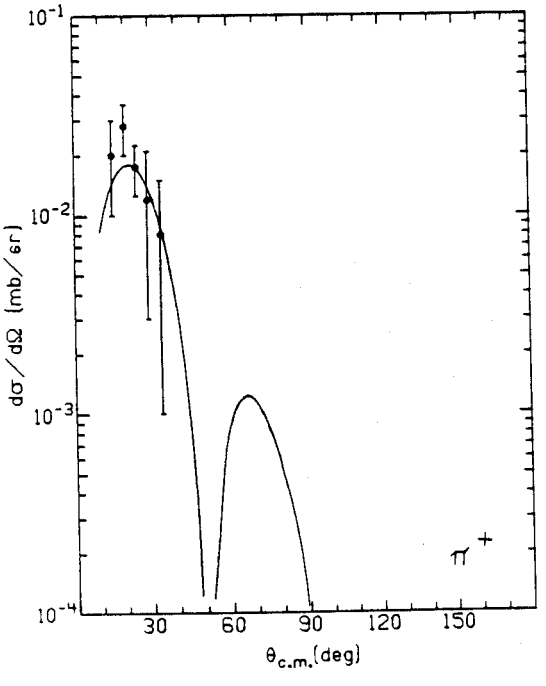

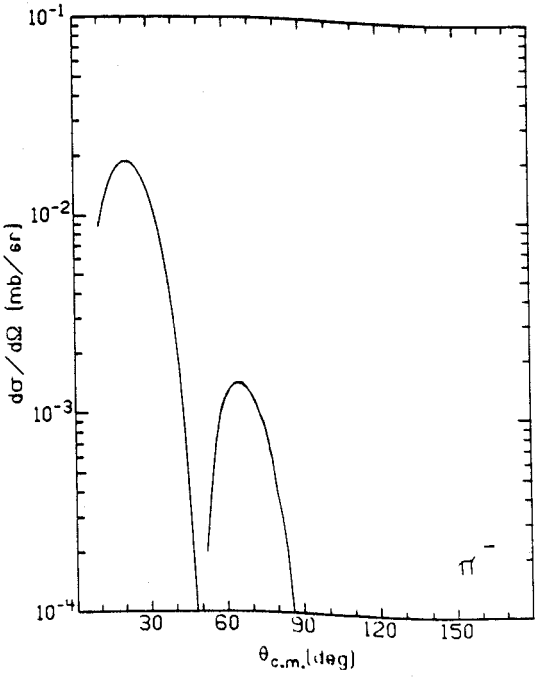

Figure 5-9

much as 50%, but better understanding will have to await new data being acquired at Los Alamos. It will be most important to examine these results for systematic deviations which might reflect effects similar to those being studied in proton and electron scattering [Tok 80]. The strong absorption of pions near resonance makes study of high momentum transfer difficult; it may be necessary to do these experiments at lower energy.

The observation of isospin mixing in pion scattering from ^{16}O [Hol 80] was an indication of the value of the strong isospin dependence of the Δ_{33} dominated interaction near resonance. The conclusions of [Hol 80] were based on a simple model and did not predict the absolute magnitude of the cross sections. Since then, electron scattering data has been taken at MIT [Hyd 81] which allow the normalization of the amplitudes in [Hol 80] to the T=1 state (which had been a free parameter). The results are given in Table 5-5, and are plotted on the left side of Figure 5-10. The value of α was also chosen as 0.638 to fit this data set. It should be noted that these are "stretched" states like those studied in ^{28}Si, so only one configuration is expected to produce a significant contribution.

Table 5-5

Spectroscopic Z Coefficients
for the ^{16}O 4^- States

Energy	T=0	T=1
17.79	0.3447	-0.08601
18.98	0.00089	-0.6826
19.80	0.3638	0.08465

Figure 5-10

Transverse magnetic form factor (left) and 162 MeV π^+ and π^- inelastic scattering from the ^{16}O (18.98, 17.79 and 19.80 MeV) 4^- states, as described in the text.

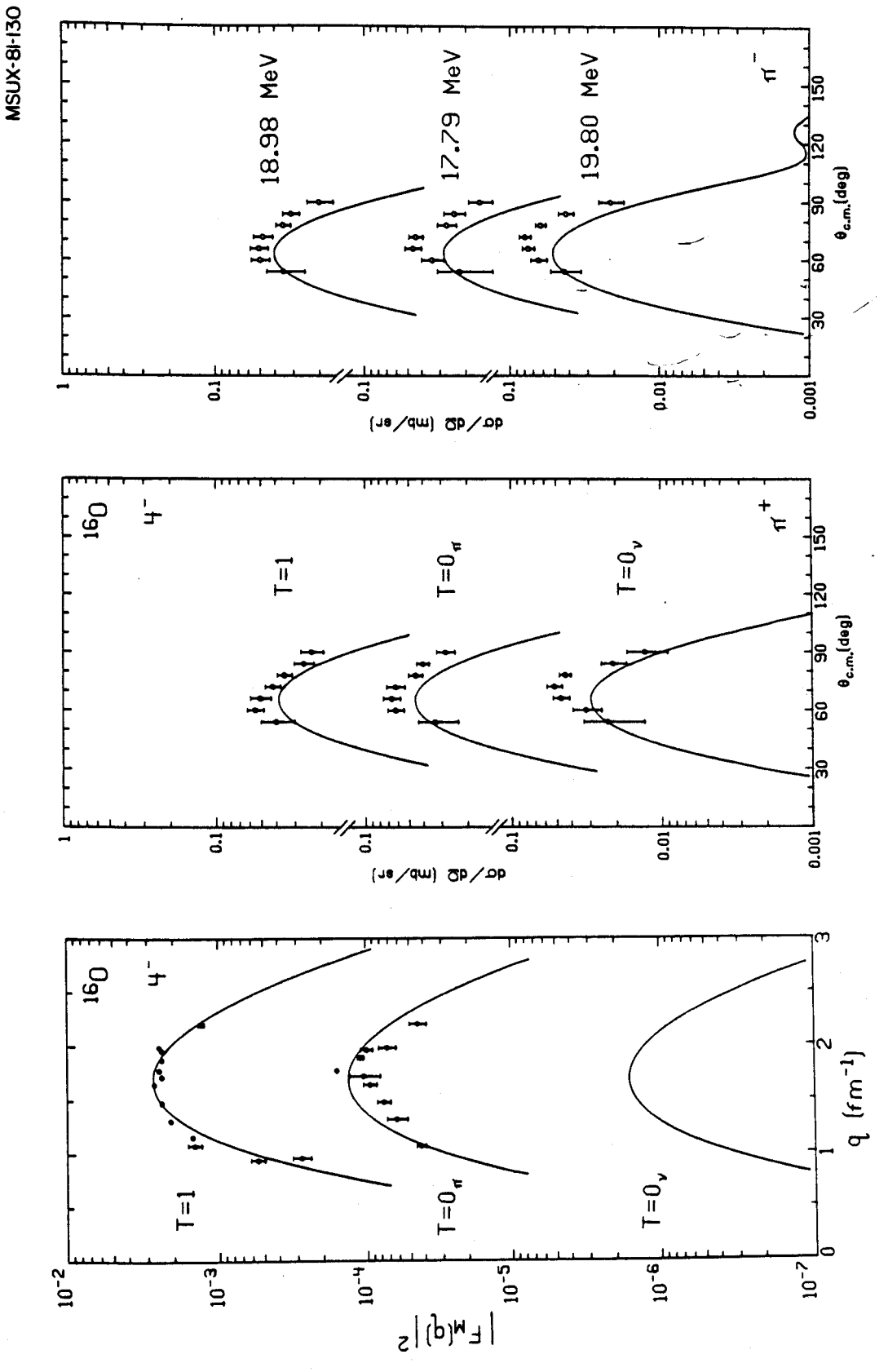
MSUX-81-130
16O
4-
T=1
T=0π
T=0ν
|FM(q)|2
q (fm-1)
18.98 MeV
17.79 MeV
19.80 MeV
π-
π+
dσ/dΩ (mb/sr)
θc.m.(deg)

Figure 5-10

The predictions for the 162 MeV pion data are shown on the right side. The results are consistently 30% low, but the ratios of π^+/π^- are in good agreement with the data as shown in Table 5-6. Equally interesting is the prediction of the $T=0_\pi$ electron scattering strength, which is quite accurate. The fact that the T=0 data from the pion experiment tend to peak at higher momentum transfer may be hinted at in the electron data as well. This may indicate differences in the radial distributions of the neutron and proton components of these wave functions (assumed the same here), which could also provide insight into these states.

In summary, it is seen that the pion predictions based on existing electron scattering data are in reasonable agreement with the data. These cases suggest that the calculations are 30-50% low, in contrast to the results with the 6^- state in Section 5.3, but the 20% systematic errors quoted for all of these experiments make conclusions difficult. The shape of the angular distributions are usually correctly reproduced.

Table 5-6

Cross-Section Ratios
(π^+/π^-) for ^{16}O 4^- States

Energy	$\frac{\pi^+}{\pi^-}$ (Expt)	$\frac{\pi^+}{\pi^-}$ (Theory)
17.79	1.59 ± 0.12	1.68
18.98	0.96 ± 0.08	1.00
19.80	0.60 ± 0.05	0.61

5.5 SUMMARY

The means to use a microscopic description of the inelastic scattering form factor was introduced. This description was seen to be quite useful when the state being considered could be expressed as a simple shell model state with a spectroscopic factor determined by other probes. A convenient ansatz, which replaces the collective density with the microscopic one, allowed the use of the full second order interaction for natural parity transitions. The results were consistent with those of the "equivalent" four-parameter potential, suggesting that this is a reasonable solution to the problem of including density dependence in the inelastic scattering calculation. It was also found that low energy pions are very sensitive to high-momentum components of the density. Thus it may be important to use microscopic densities, since this allows control of the geometry of the inelastic density independent of the ground state density used for the elastic scattering.

Results for transitions with unnatural parity were also presented. The simple IA force described does an adequate job of fitting the well known 6^- T=1 state in ^{28}Si. However, it was low for calculations of other states, both of which are also well known from electron scattering. The large systematic errors of these experiments limit our conclusions, since it is impossible to distinguish between these calculations and those using the energy shift [Cot 80] which would be 15% higher. Predictions of cross section ratios, which are crucial to the extraction of the isospin mixing coefficients, are not affected by this normalization problem. These results are within experimental errors, but different from what was assumed in the calculation of the wave functions

[Hol 80], where Δ_{33} dominance was assumed. The isospin mixing may need to be reevaluated in this context as better data (especially for the T=0 electron scattering) is obtained. Most of the uncertainties described here must await more data before they can be resolved.

A similar situation exists for the T=1 part of the interaction for natural parity transitions. The calculation for the neutron state in ^{208}Pb showed great sensitivity to the corrections in the T=0 part of the force. Similar corrections in the isovector part should also be easily identified by studying states of this type. The isovector interaction also contributes to differences in scattering from ^{40}Ca and ^{48}Ca. This is difficult to disentangle from the effect of the coulomb force via the velocity dependence, so it's not as useful in determining the force. Pure isovector transitions, and charge exchange, are the best means to identify the properties of the effective isovector strength.

CHAPTER 6

CHARGE EXCHANGE SCATTERING

The charge exchange reaction provides information complimentary to that described so far. This reaction is only sensitive to the isovector part of the force, which has not been studied very extensively. It also provides a consistency check on optical model predictions of quasi-elastic cross sections. The recent construction of a π° spectrometer at LAMPF has made practical study of these reactions possible.

This short chapter will set up the basic foundation for these calculations, and then investigate the properties of the reaction for a few cases. Section 6.1 will outline the additional theory necessary for the discussion of single charge exchange (SCE) reactions. Section 6.2 will then examine some representative calculations as a test of the simple model.

6.1 MODEL FOR CHARGE EXCHANGE CALCULATIONS

This section outlines the basic formulae that are needed in addition to the standard ones in Chapter 3. We first work out the operators involved to see how they change for SCE reactions. The form factors are expressed both in terms of the Lane model and a microscopic density, to allow some of the comparisons we made in Chapter 5.

Charge exchange is produced by the isovector part of the potential, which is

$$\underset{\sim}{t}\cdot\underset{\sim}{\tau}\left\{ p_1 b_1\ \delta\rho(r) - \frac{c_1}{p_1}\ \vec{\nabla}\cdot\ \delta\rho(r)\ \vec{\nabla} + \frac{1}{2}\left(1 - p_1^{-1}\right) c_1\ \nabla^2\ \delta\rho(r)\right\} \tag{6-1}$$

to first order, neglecting the spin-orbit contribution, as defined in equation (2-43). The operator $\underset{\sim}{t}\cdot\underset{\sim}{\tau}$ is of interest because (in the Lane [Lan 62] model) it produces the factors that are different between elastic and SCE reactions. This is

$$\underset{\sim}{t}\cdot\underset{\sim}{\tau} = t_x\tau_x + t_y\tau_y + t_z\tau_z \tag{6-2}$$

which can be rewritten more transparently using raising and lowering operators to give

$$\underset{\sim}{t}\cdot\underset{\sim}{\tau} = t_o\tau_o - t_+\tau_- - t_-\tau_+ \tag{6-3}$$

where

$$t_{\pm} = \mp (t_x \pm i\, t_y)/\sqrt{2}$$

$$t_o = t_z$$

and similarly for τ. These operators have the property that

$$\begin{aligned} t_+|\pi^+\rangle &= 0 & \tau_+|p\rangle &= 0 \\ t_o|\pi^+\rangle &= |\pi^+\rangle & \tau_o|p\rangle &= |p\rangle \\ t_-|\pi^+\rangle &= |\pi^\circ\rangle & \tau_-|p\rangle &= \sqrt{2}\,|n\rangle \end{aligned} \tag{6-4}$$

since $\tau_o = 2\, t_o^N$ and $\tau_{\pm} = \sqrt{2}\, t^N$. From these definitions it is readily seen that the form of equation (6-3) is consistent with conservation of charge during the reaction.

For the purposes of illustration, this operation will be evaluated for the case of π^+ scattering from a target with total isospin T and projection $T_Z = (Z-N)/2$. Recalling that the total isospin operator is

just $\underset{\sim}{T} = \sum_i \underset{\sim}{t}_i^N$ summed over the nucleons in the target, the formula reduces to

$$\underset{\sim}{t}\cdot\underset{\sim}{\tau} = 2t_o\, T_o - \sqrt{2}\left(t_+T_- + t_-T_+\right) \quad . \tag{6-5}$$

For the case mentioned we get

$$\begin{aligned}\underset{\sim}{t}\cdot\underset{\sim}{\tau}\left|\pi^+\right\rangle \left|T,T_Z\right\rangle &= 2t_o\left|\pi^+\right\rangle T_o\left|TT_Z\right\rangle \\ &\quad - 2t_+\left|\pi^+\right\rangle T_-\left|TT_Z\right\rangle \\ &\quad - \sqrt{2}t_-\left|\pi^+\right\rangle T_+\left|TT_Z\right\rangle \qquad (6\text{-}6)\\ &= 2\left|\pi^+\right\rangle T_Z\left|TT_Z\right\rangle - 0 \\ &\quad - \sqrt{2}\left|\pi^+\right\rangle\sqrt{T(T+1) - T_Z(T_Z+1)}\ \left|TT_Z+1\right\rangle\end{aligned}$$

which becomes

$$(Z-N)\left|\pi^+\right\rangle \left|TT_Z\right\rangle - \sqrt{2}\,\sqrt{N-Z}\left|\pi^o\right\rangle \left|TT_Z+1\right\rangle \tag{6-7}$$

for the case where $T = -T_Z$, as will be the situation for the targets studied here. The first term is the contribution to elastic scattering, which enters as

$$\varepsilon_\pi \frac{(Z-N)}{A}\rho(r) \tag{6-8}$$

in equation (2-44). The factor of A is required to convert $\rho(r)$ to a single nucleon density. The second term is the contribution to SCE, and can be parametrized in two ways.

The Lane model [Lan 62] is a straightforward extension of equation (6-7) to give

$$\frac{\sqrt{2}\sqrt{N-Z}}{A}\ \rho(r) \tag{6-9}$$

for the transition density in SCE. By using $\rho(r)/A$, this essentially assumes that all the nucleons participate equally, ignoring any specifics of nuclear structure. This is the same assumption made in writing equation (6-8), but it is far more important in equation (6-9) than in a small correction term like equation (6-8). The equivalent microscopic density is found by replacing equation (6-9) by the overlap of a specific final state with $\sqrt{2}\ T_-$ operating on the ground state. For an analog transition like $^{13}C \rightarrow {}^{13}N$, this becomes just

$$\sqrt{2}\ \rho_{IAS}(r)\ Y_{00}(r) \tag{6-10}$$

where ρ_{IAS} is the density of the specific orbital involved (the $p_{1/2}$ in the case cited). As a practical note, the algebra in DWPI assumes that a Y_{LM} explicitly multiplies the form factor so that a correct normalization of equation (6-9) requires the addition of $\sqrt{4\pi}\ Y_{00}$, while this operator automatically appears from the formulae used to obtain equation (6-10).

6.2 SAMPLE CALCULATIONS

The calculations shown here will all employ the IA form of the potential in equation (6-1), primarily because the information about the isovector part of the interaction is limited. In this way the results will be amenable to scaling and the determination of the effective strength of the isovector potential. The parameters used will be those already defined for Set A in other parts of this thesis.

The first case to be studied is the reaction $^{13}C\ (\pi^+,\pi^\circ)\ ^{13}N$. This has a long history, with total cross sections first measured using nuclear chemistry [Chi 69, Zai 73, Sha 76]. These data have proven very difficult to explain, typical results can be found in [Gib 76, Spa 79]. More recent results with the π° spectrometer at LAMPF have provided angular distributions and a confirmation of the older total cross section measurements [Dor 79]. The results of the Lane model calculations are shown with a dashed line in Figures 6-1 and 6-2. The 162 MeV calculation is similar in shape but much lower than the 150 MeV (solid points) and 180 MeV (open points) data, as seen on the right side of Figure 6-1. Figure 6-2 shows that these calculations have the same steep falloff in the resonance region as is seen in other calculations. The data shown are [Zai 73] and [Sha 76].

The solid line in these figures shows the result with the microscopic description in terms of a pure $p_{1/2}$ particle involved in the analog transition. The results are quite different, particularly the low energy angular distribution, and the cause is not immediately evident. What is interesting is that the cross sections do not fall off rapidly with the increase in bombarding energy. Some of this (about 20% at high energy) is attributable to the inclusion of spin-flip in these calculations, but most of the difference must be due to the onset of strong absorption near 100 MeV. We have already seen that the distortion in this region keeps the pion from seeing the interior wave function. The Lane density is mostly inside the strong absorption radius, so these cross sections are reduced by a large factor.

Figure 6-1

Angular distribution of single charge exchange with 50 MeV and 162 MeV π^+ on ^{13}C, using the Lane model (dashed curve) and single particle model (solid curve).

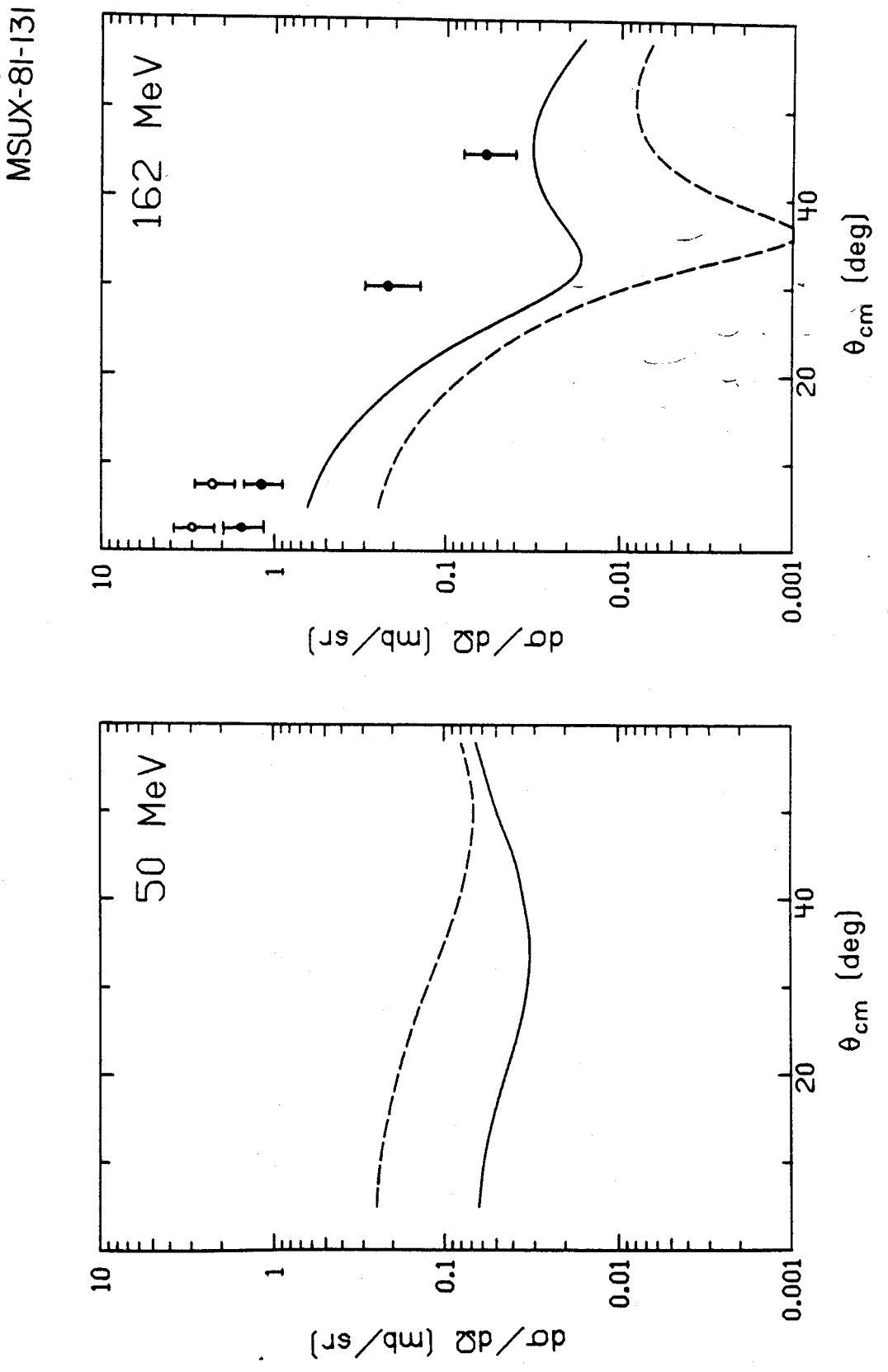
MSUX-81-131
162 MeV
50 MeV
dσ/dΩ (mb/sr)
θcm (deg)
10
1
0.1
0.01
0.001
20
40

Figure 6-1

Figure 6-2

Excitation function for π^+ single charge exchange on ^{13}C, using Lane (dashed) and single particle (solid curve) models.

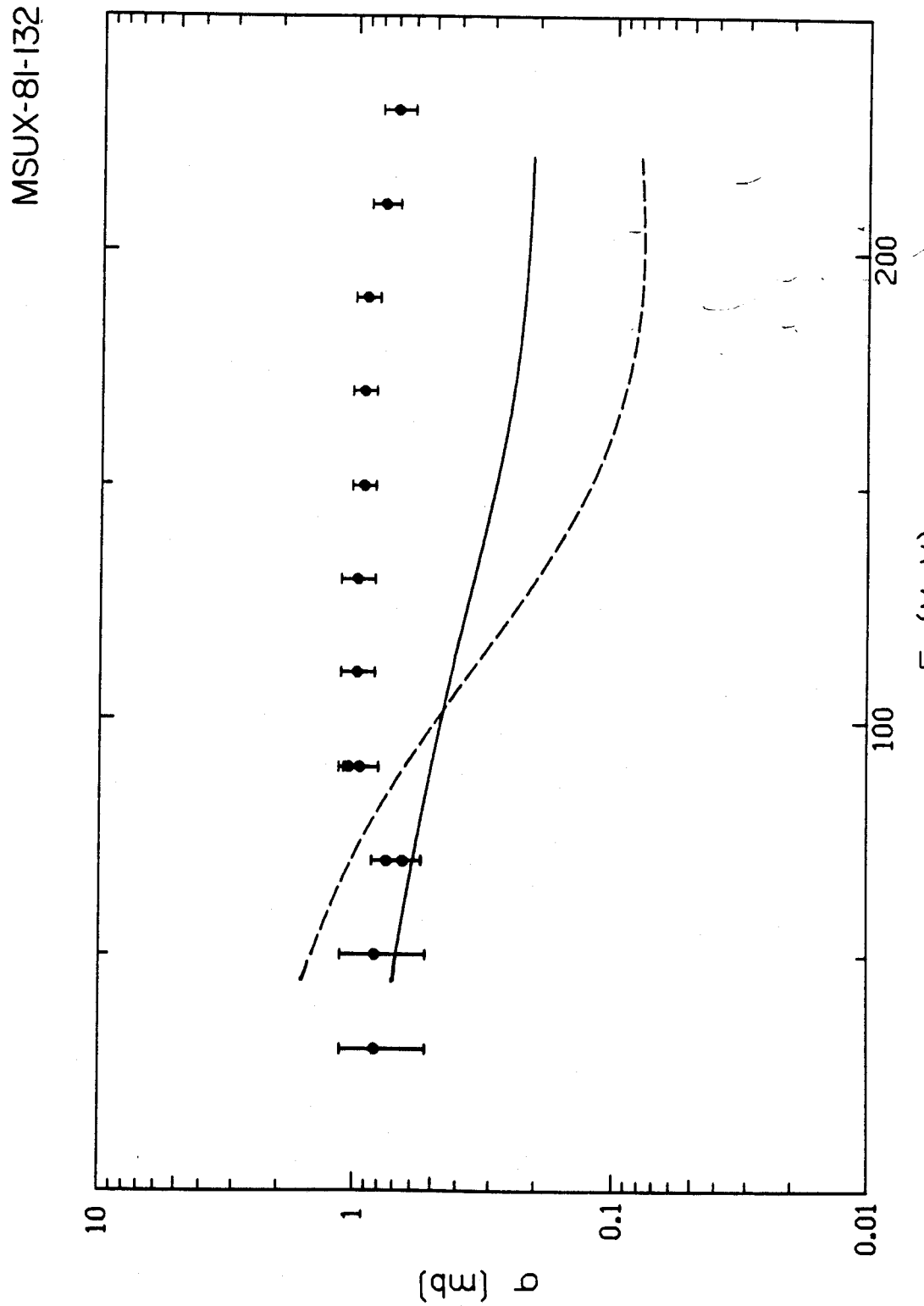

Figure 6-2

Of similar interest is the mass dependence of the cross sections at a fixed energy. These were all calculated in the Lane model to test the consistency of this with another simple model of SCE reactions [Joh 79]. The results are shown in Figure 6-3, scaled to the ^{208}Pb point. These values were all given in relative cross section, the calculated values for the ^{13}C and ^{208}Pb cross sections at 5° were 0.22 mb and 0.18 mb, respectively. At this energy the angular distributions of different models are similar, so this should be a reasonable prediction apart from the overall scale. These agree fairly well with the data, and are quite similar to the calculations of Mikkel Johnson's [Joh 79] semi-classical model.

Finally, the Lane (dashed) and microscopic (solid) results are plotted for the ^{15}N (π^+,π°) ^{15}O case at 50 MeV as shown in Figure 6-4. The predicted angular distributions here are very different. The Lane results are consistent with those for ^{13}C, but the other calculation has dropped significantly. The situation here is confusing, and may reflect some of the sensitivity to the distorted waves and choice of transition density that we saw in other low energy data.

6.3 SUMMARY

The method for doing a simple calculation of pion single charge exchange was outlined. The results are in rough agreement with low energy cross sections, but are systematically low at higher energies. Whether this is due to the need to use a stronger interaction or a more realistic form factor needs to be studied in parallel with other isovector transitions.

Figure 6-3

Dependence of 100 MeV π^+ single charge exchange on target mass using the Lane model.

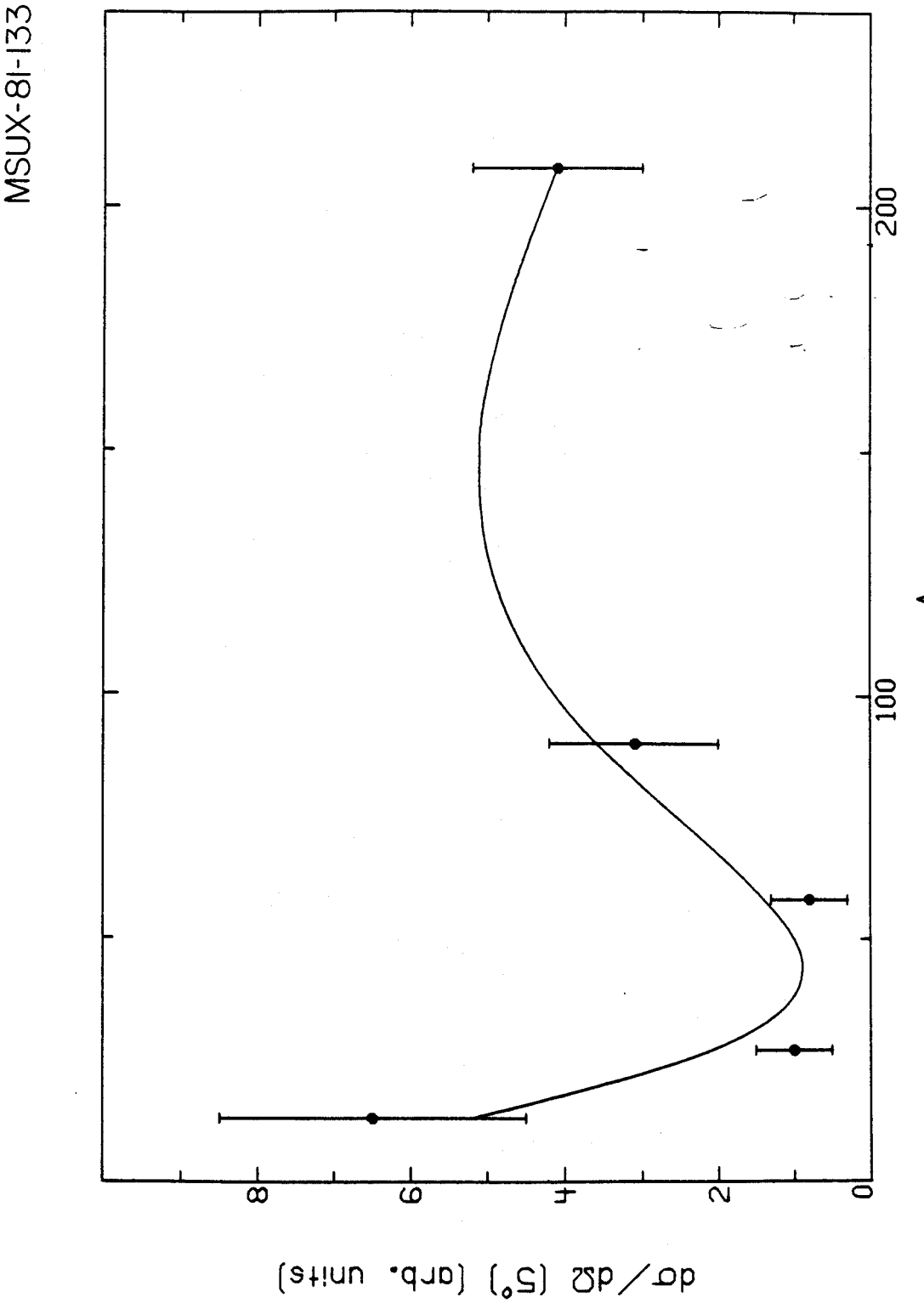

Figure 6-3

Figure 6-4

Single charge exchange with 50 MeV π^+ on ^{15}N, calculated with the Lane (dashed) and single particle (solid curve) model.

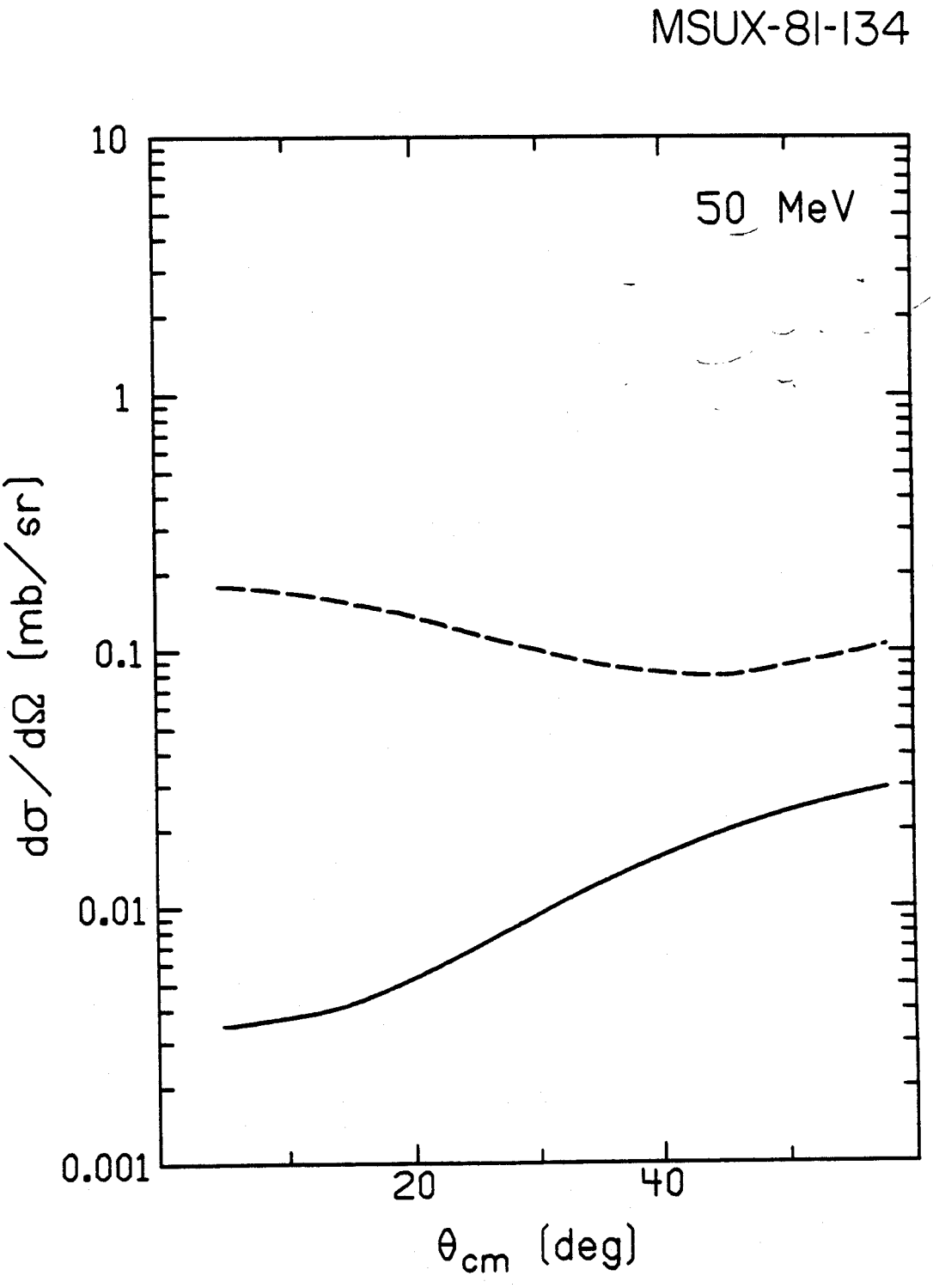

Figure 6-4

CHAPTER 7

CONCLUSIONS

In the first half of this work we saw that the impulse approximation and multiple scattering theory could be used to construct a pion-nucleus interaction that, with some minor adjustments in a few parameters, accurately describes elastic scattering from very low energies up to 200 MeV. This complicated density dependent interaction was found to be roughly equivalent to a simple four parameter effective interaction, which simplified the discussion of the essential physics introduced by the corrections to the impulse approximation. The theoretical pion-nucleus isoscalar central interaction, calibrated by the large amount of elastic scattering data, was then tested against isoscalar natural parity inelastic transitions.

The low energy elastic scattering data clearly prefer an effective interaction with increased s-wave repulsion and weakened p-wave attraction. When this interaction is used for inelastic scattering calculations, the collective states are correctly described. The inelastic scattering results are found to be very sensitive to the choice of optical potential, primarily because the potential is relatively transparent at these energies. The absorption required at 50 MeV is less than the value determined by pionic atoms, requiring some further theoretical study.

The resonance region data are reasonably described by the theoretical parameters. The elastic cross sections are not affected much by changes in the interaction, except at back angles where there is little data. Again it is found that the isoscalar interaction preferred by

the elastic data is also preferred by the inelastic scattering data. Here, however, the inelastic calculations are quite insensitive to the choice of distorting potential (mainly because the potential is strongly absorbing in each case), so it is more productive to investigate properties of the force by looking at inelastic scattering reactions.

Reactions that investigate the transition region (60-100 MeV) seem complicated and are difficult to interpret. Part of this is due to the fact that diffraction effects coexist with effects associated with properties of the interaction, making it hard to disentangle the cause responsible for the observed angular distributions. There are some interesting cases that seem to suggest that the pion may be a good probe of the high momentum components of the wave function at these beam energies.

In summary, we saw in Chapter 4 that the isoscalar central interation, obtained from theory and calibrated with elastic scattering data, gave a good description of collective inelastic transitions. Further study of the optical potential and inelastic scattering to various natural parity states should help clarify the details that are still missing. Clearly the ultimate test of the theory is to produce a description of the data at 80 MeV that is consistent with the high and low energy results.

There is not very much information with which to test the isovector central interaction. The evidence from neutron states is that the isovector part of the force is reasonable, although it is difficult to separate it from the effects of the coulomb force on the velocity

dependent p-wave interaction. Charge exchange reactions provide complimentary information on the isovector interaction, but seem to imply that the defect is mainly in our understanding of the reaction rather than in any particular part of the force. Further work is needed, particularly in obtaining a better understanding of the medium corrections to the isoscalar central interaction.

Information about the spin-orbit interaction can be obtained only from inelastic transitions to unnatural parity states. The evidence from such spin-flip transitions is that the spin-orbit interaction is reasonably described by the impulse approximation, but may need to be increased by 15-20% at 165 MeV. No information exists for these reactions at other energies. The simple structure of the stretched states has made them ideal places to test the interaction, and a systematic collection of data should contribute a great deal to our understanding of this part of the pion-nucleon interaction.

In summary, much is understood but much more remains to be studied. In particular, the steady improvements in beam quality and detector resolution will increase the amount of data in areas that have currently only been lightly surveyed due to limitations of the experimental equipment. One purpose of this work has been to identify consistencies, as in the isoscalar interaction, and point towards areas of interest, such as the spin-flip transitions and studies of the proton and neutron components of a wave function, in order to contribute to this process of choosing good places to test the theory and study nuclear physics. Identification of the properties of the effective interaction and its application to the consistent interpretation of a large set of data is one means to this end.

APPENDICES

APPENDIX A

PION SCATTERING AMPLITUDE

This appendix gives the formal conventions used in the definition of the pion scattering parameters in terms of the pion-nucleon phase shifts. The derivation essentially follows that of [Str 79a, Eis 80].

The scattering amplitude is expanded in terms of projection operators for the total isospin T, and the angular momentum L and total angular momentum $J = L \pm 1/2$. The result is

$$f = \sum_{\substack{T \\ L,J}} P_T \, P_{LJ} \, \alpha^L_{2T,2J} \, (2L+1) \, P_L \, (\cos\,\theta) \tag{A-1}$$

where $$\alpha^L_{2T,2J} = \left(e^{2i\delta^L_{2T,2J}} - 1 \right) \Big/ 2ik$$

is defined by the phase shifts and the projection operators are

$$\begin{aligned} P_{1/2} &= \frac{1}{3}\,(1 - \underset{\sim}{t}\cdot\underset{\sim}{\tau}) & P_{3/2} &= \frac{1}{3}\,(2 + \underset{\sim}{t}\cdot\underset{\sim}{\tau}) \\ P_{LJ_<} &= (L - \vec{\sigma}\cdot\vec{\ell})/(2L+1) & P_{LJ_>} &= (L+1 + \vec{\sigma}\cdot\vec{\ell})/(2L+1) \quad . \end{aligned} \tag{A-2}$$

We are limiting the discussion to s- and p-wave cases, so the sum on L,J gives

$$f = \sum_T P_T \left\{ \left[\alpha^0_{2T,1} \right] + \left[\alpha^1_{2T,1}(1 - \vec{\sigma}\cdot\vec{\ell}) + \alpha^1_{2T,3}(2 + \vec{\sigma}\cdot\vec{\ell}) \right] \cos\,\theta \right\} \tag{A-3}$$

since $\vec{\ell} P_0(\cos\,\theta)$ vanishes. We can rewrite this as

$$\begin{aligned} f = \sum_T P_T \Bigg\{ & \left[\alpha^0_{2T,1} \right] + \left[\alpha^1_{2T,1} + 2\alpha^1_{2T,3} \right] \cos\,\theta \\ & + \left[-\alpha^1_{2T,1} + \alpha^1_{2T,3} \right] \vec{\sigma}\cdot\vec{\ell} \cos\,\theta \Bigg\} \end{aligned} \tag{A-4}$$

and then do the sum on T. This gives

$$\alpha^0_{1,1}\,(1 - \underset{\sim}{t}\cdot\underset{\sim}{\tau})/3 + \alpha^0_{3,1}\,(2 + \underset{\sim}{t}\cdot\underset{\sim}{\tau})/3$$

$$= \frac{1}{3}\left[\left(\alpha^0_{1,1} + 2\alpha^0_{3,1}\right) + \left(-\alpha^0_{1,1} + \alpha^0_{3,1}\right)\underset{\sim}{t}\cdot\underset{\sim}{\tau}\right] \tag{A-5}$$

for the s-wave part, and similar results for the others. Combined, these give

$$\begin{aligned} f = {} & \frac{1}{3}\left[\left(\alpha^0_{1,1} + 2\alpha^0_{3,1}\right) + \left(-\alpha^0_{1,1} + \alpha^0_{3,1}\right)\underset{\sim}{t}\cdot\underset{\sim}{\tau}\right] \\ & + \frac{1}{3k^2}\left[\left(\alpha^1_{1,1} + 2\alpha^1_{3,1} + 2\alpha^1_{1,3} + 4\alpha^1_{3,3}\right)\right. \\ & \left. + \left(-\alpha^1_{1,1} + \alpha^1_{3,1} - 2\alpha^1_{1,3} + 2\alpha^1_{3,3}\right)\underset{\sim}{t}\cdot\underset{\sim}{\tau}\right]k^2\cos\theta \\ & + \frac{1}{3k^2}\left[\left(-\alpha^1_{1,1} - 2\alpha^1_{3,1} + \alpha^1_{1,3} + 2\alpha^1_{3,3}\right)\right. \\ & \left. + \left(\alpha^1_{1,1} - \alpha^1_{3,1} - \alpha^1_{1,3} + \alpha^1_{3,3}\right)\underset{\sim}{t}\cdot\underset{\sim}{\tau}\right]k^2\,\vec{\sigma}\cdot\vec{\ell}\cos\theta \quad . \end{aligned} \tag{A-6}$$

Since $k^2\cos\theta = \vec{k}\cdot\vec{k}'$, and

$$\begin{aligned} \vec{\ell}\cos\theta &= -i\,\vec{r}\times\left(\hat{\theta}\,\frac{\partial}{\partial\theta}\right)\cos\theta \\ &= i\,\frac{\vec{k}\times\vec{k}'}{k^2\sin\theta}\,\sin\theta \end{aligned} \tag{A-7}$$

gives $k^2\,\vec{\sigma}\cdot\vec{\ell}\cos\theta = i\vec{\sigma}\cdot(\vec{k}\times\vec{k}')$, equation (A-6) defines b_o, b_1, c_o, c_1, s_o, s_1 in equation (2-26).

Finally, we note that the values of the $\alpha^L_{2T,2J}$ are obtained from the phase shifts $\delta^L_{2T,2J}$ as parametrized by Rowe, Salomon and Landau [Row 78].

APPENDIX B

EQUIVALENT FORMS OF PION OPTICAL POTENTIAL

There are two points to be made here. One is to convert the standard Kisslinger potential into a local (Laplacian) form that is suitable for plotting in momentum space. The other is to sketch the conversion of the potential into coordinate space.

The local form is obtained by using that

$$\begin{aligned} q^2 &= (\vec{k}-\vec{k}') \cdot (\vec{k}-\vec{k}') \\ &= k^2 + k'^2 - 2\vec{k}\cdot\vec{k}' \\ &= 2k^2 - 2\vec{k}\cdot\vec{k}' \ , \end{aligned} \tag{B-1}$$

so we use the conversion

$$\vec{k}\cdot\vec{k}' = k^2 - \frac{1}{2} q^2 \tag{B-2}$$

to eliminate $\vec{k}\cdot\vec{k}'$ from the expressions for the potential. In order to plot the full potential in equation (2-55) it is necessary to evaluate the additional density-dependent parts of the interaction. This is done following the idea in Section 2.6, where a constant value of $\rho = 0.12$ fm^{-3} is used. Writing this as ρ_{eff} we then have

$$\begin{aligned} -4\pi \frac{\hbar^2}{2\omega} \Bigg\{ & \left(p_1 \, b_o + p_2 \, B_o \, \rho_{eff} \right) \\ & + \frac{p_1^{-1} \, c_o + p_2^{-1} \, C_o \, \rho_{eff}}{1 + \frac{4\pi}{3} \lambda \left[p_1^{-1} \, c_o + p_2^{-1} \, C_o \, \rho_{eff} \right] \rho_{eff}} \left(k^2 - \frac{1}{2} q^2 \right) \\ & - \left[\left(1 - p_1^{-1} \right) c_o + \left(1 - p_2^{-1} \right) C_o \, \rho_{eff} \right] \frac{q^2}{2} \Bigg\} \end{aligned} \tag{B-3}$$

for the t-matrix plotted in Chapter 4.

The coordinate space versions of $\vec{k}\cdot\vec{k}'$ and q^2 come from their fourier transforms. The first is

$$\frac{1}{(2\pi)^6}\int e^{-i\vec{k}'\cdot\vec{r}'}\ \vec{k}\cdot\vec{k}'\ \rho(q)\ e^{i\vec{k}\cdot\vec{r}}\ d^3k\ d^3k' \tag{B-4}$$

$$= \frac{1}{(2\pi)^6}\int e^{-i\vec{k}'\cdot\vec{r}'}\ \vec{\nabla}'\cdot\vec{\nabla}\ \rho(q)\ e^{i\vec{k}\cdot\vec{r}}\ d^3k\ d^3k'$$

which simplifies if it is rewritten in terms of

$$q = k-k' , \qquad Q = \frac{k+k'}{2} ,$$

$$x = r-r' , \qquad X = \frac{r+r'}{2}$$

to give

$$\frac{1}{(2\pi)^6}\int \overleftarrow{\nabla}'\cdot\vec{\nabla}\ \rho(q)\ e^{iq\cdot X}\ e^{iQ\cdot x}\ d^3q\ d^3Q \tag{B-5}$$

$$= \overleftarrow{\nabla}'\cdot\ [\delta(x)\ \rho(X)\ \vec{\nabla}]$$

where we have been careful to keep the $\vec{\nabla}$ operators acting on the wave functions as defined in equation (B-4). Using the delta function reduces this to a function of r, and the $\vec{\nabla}$ can be reversed to give

$$-\vec{\nabla}\cdot\ [\rho(r)\ \vec{\nabla}] \tag{B-6}$$

which is the form used here.

The q^2 term is done in a similar fashion, where it is convenient to start with the variables of equation (B-5) giving

$$\frac{1}{(2\pi)^6}\int q^2\ \rho(q)\ e^{iq\cdot X}\ e^{iQ\cdot x}\ d^3q\ d^3Q$$

$$= \frac{1}{(2\pi)^6}\left(-\nabla_X^2\right)\int \rho(q)\ e^{iq\cdot X}\ e^{iQ\cdot x}\ d^3q\ d^3Q \qquad \text{(B-7)}$$

$$= -\nabla_X^2\ \rho(X)\ \delta(x)\ ,$$

which can be reduced to

$$-\nabla^2\ \rho(r) \qquad \text{(B-8)}$$

by using the delta function.

APPENDIX C

DENSITY PARAMETERS

The radial densities used for the nuclear ground states in the optical potential are in one of two forms. One is the gaussian form

$$\rho(r) = \rho_o \left[1 + \alpha\left(\frac{r}{W}\right)^2\right] e^{-(r/W)^2}$$

with

$$\rho_o = 2\left[(2 + 3\alpha)\ (\sqrt{\pi}\ W)^3\right]^{-1}, \qquad \text{(C-1)}$$

while the other is the three-parameter Fermi (or Woods-Saxon) form

$$\rho(r) = \rho_o \frac{1 + W\left(\frac{r}{c}\right)^2}{1 + \exp\left(\frac{r-c}{t}\right)}$$

with

$$\rho_o = \frac{3}{4\pi\ c^3}\left[1 + \left(\frac{\pi t}{c}\right)^2 + \frac{W}{5}\left(3 + 10\left[\frac{\pi t}{c}\right]^2 + 7\left[\frac{\pi t}{c}\right]^4\right)\right]^{-1} . \qquad \text{(C-2)}$$

where we use a = (4 ln3)t as our input. The parameters are taken from electron scattering results [DeJ 74] with the finite size of the proton removed using

$$R_c^2 = R_p^2 + 0.64$$

to convert the charge radii to nuclear radii. The values used are tabulated in Table C-1. For convenience, this table also lists the energy and collective model deformation parameter β_L [as defined in equation (3-44)] of the collective states studied here.

TABLE C-1

Density Parameters

Nucleus	Gaussian Density [Equation (C-1)] W_c	W	α	Excited States J^π	E	β_J
^{12}C	1.66	1.57	1.33	2^+	4.44	0.60
				3^-	9.63	0.44
^{16}O	1.83	1.75	1.54			

Nucleus	Three-Parameter Fermi [Equation (C-2)] C_c	C	a	W	Excited States J^π	E	β_J
^{28}Si	2.93	2.82	2.50	0	2^+	1.77	0.40
^{40}Ca	3.67	3.58	2.56	-0.10	3^-	3.74	0.39
^{48}Ca	3.74	3.65	2.30	-0.03	2^+	3.83	0.17
^{90}Zr	4.83	4.76	2.18	0	3^-	2.75	0.14
^{208}Pb	6.46	6.41	2.38	0	3^-	2.62	0.12

APPENDIX D

EVALUATE $\vec{\nabla}\cdot\vec{\nabla}$ IN FORM FACTOR

In equation (3-36) it was assumed that the angular integral could be done separately. Since the $\vec{k}\cdot\vec{k}'$ part of the interaction looks like

$$\vec{\nabla}\cdot\ [F(r)\ Y_{LM}]\ \vec{\nabla}\ , \tag{D-1}$$

there is an explicit angular dependence in the $\vec{\nabla}$ operators that could change the coupling to the angular parts of the wave functions. This is not the case, as was shown by [Edw 71], but the result is important enough to include here.

The integral we need to evaluate looks like

$$\int d^3r\ \frac{u^*_\ell}{r}\ Y_{\ell m}\ \vec{\nabla}\cdot\ [F_L(r)\ Y_{LM}]\ \vec{\nabla}\ \frac{u_{\ell'}}{r}\ Y_{\ell'm'} \tag{D-2}$$

which we write schematically as

$$\int d^3r\ A\ \vec{\nabla}\cdot\ [B\ \vec{\nabla}\ C] \tag{D-3}$$

for convenience. The gradient can be reversed by integrating by parts, giving

$$-\int d^3r\ (\vec{\nabla}A)\ B\ (\vec{\nabla}C) \tag{D-4}$$

which can be written as

$$\frac{1}{2}\int d^3r\ [(\nabla^2 A)BC - A(\nabla^2 B)C + AB(\nabla^2 C)]\ . \tag{D-5}$$

The proof of the identity used to construct equation (D-5) follows. It is based on combining

$$\vec{\nabla}\cdot [U\ \vec{\nabla}\ V] = U(\nabla^2 V) + (\vec{\nabla}U)\cdot(\vec{\nabla}V) \tag{D-6}$$

and

$$\int W\ \vec{\nabla}\cdot [U\ \vec{\nabla}\ V] = -\int(\vec{\nabla}W)\ U(\vec{\nabla}V) \tag{D-7}$$

to get

$$-\int(\vec{\nabla}W)\ U(\vec{\nabla}V) - \int(\nabla^2 V)\ WU = \int(\vec{\nabla}U)\ W(\vec{\nabla}V)\ . \tag{D-8}$$

Reversing the role of U and V gives

$$-\int V(\vec{\nabla}W)\ (\vec{\nabla}U) - \int VW(\nabla^2 U) = \int(\vec{\nabla}U)\ W(\vec{\nabla}V) \tag{D-9}$$

which, when combined with equation (D-8) gives

$$\int(\vec{\nabla}U)\ W(\vec{\nabla}V) = -\frac{1}{2}\left[\int(\vec{\nabla}U)\ (\vec{\nabla}W)V + \int U(\vec{\nabla}W)\ (\vec{\nabla}V) + \int(\nabla^2 U)\ WV + \int UW(\nabla^2 V)\right]\ . \tag{D-10}$$

If this is written out for each of the three possible combinations of A, B, C, then two can be substituted into the equation for the other giving

$$\int(\vec{\nabla}A)\ B(\vec{\nabla}C) = -\frac{1}{2}\left[\frac{1}{2}\int(\nabla^2 A)BC - \int A(\nabla^2 B)C + \frac{1}{2}\int AB(\nabla^2 C) - \int(\vec{\nabla}A)B\ (\vec{\nabla}C) - \frac{1}{2}\int A(\vec{\nabla}B)\ (\vec{\nabla}C) - \frac{1}{2}\int(\vec{\nabla}A)\ (\vec{\nabla}B)C\right]\ . \tag{D-11}$$

If we now use the original equation (D-10) written as

$$-\frac{1}{2}\int(\vec{\nabla}A)\ (\vec{\nabla}B)C - \frac{1}{2}\int A(\vec{\nabla}B)\ (\vec{\nabla}C)$$

$$= \int(\vec{\nabla}A)\ B(\vec{\nabla}C) + \frac{1}{2}\int(\nabla^2 A)BC + \frac{1}{2}\int AB(\nabla^2 C) \qquad \text{(D-12)}$$

we can reduce equation (D-11) to

$$\int(\vec{\nabla}A)\ B(\vec{\nabla}C) = \frac{1}{2}\int A(\nabla^2 B)C = \frac{1}{2}\int(\nabla^2 A)BC - \frac{1}{2}\int AB(\nabla^2 C) \qquad \text{(D-13)}$$

which proves the result in equation (D-5).

The final step is to separate variables, using

$$\nabla^2 = \frac{1}{r^2}\frac{d}{dr}\left(r^2\frac{d}{dr}\right) - \frac{L^2}{r^2}\ , \qquad \text{(D-14)}$$

to evaluate the integrals in equation (D-5). As a specific example, examine just one of the terms

$$\int(\nabla^2 A)BC = \int\frac{1}{r^2}\frac{d}{dr}\left(r^2\frac{dA}{dr}\right)BC\ r^2 dr\ d\Omega - \int\frac{L^2 A}{r^2}\ BC\ d^3\vec{r} \qquad \text{(D-15)}$$

where the second term gives $\ell(\ell+1)$ and the first can be integrated by parts to give

$$-\int\frac{dA}{dr}\left(\frac{dB}{dr}C + B\frac{dC}{dr}\right)d^3\vec{r} - \ell(\ell+1)\int\frac{ABC}{r^2}\,d^3\vec{r}\ . \qquad \text{(D-16)}$$

If this and the other two corresponding equations are used in equation (D-5), a large amount of cancellation occurs so that we get

$$\int A\ \vec{\nabla}\cdot\ (B\ \vec{\nabla}\ C)\ d^3\vec{r} = \frac{1}{2}\left[L(L+1) - \ell'(\ell'+1) - \ell(\ell+1)\right]\int\frac{ABC}{r^2}\,d^3\vec{r}$$

$$-\int\left(\frac{dA}{dr}\right)B\left(\frac{dC}{dr}\right)d^3\vec{r}\ . \qquad \text{(D-17)}$$

If we now return to the original definition of the terms, we see that we have

$$\frac{1}{2}\left[L(L+1) - \ell'(\ell'+1) - \ell(\ell+1)\right]\int \frac{u_\ell^*}{r} F_L \frac{u_{\ell'}}{r}\, dr \int Y_{\ell M}\, Y_{LM}\, Y_{\ell' m'}\, d\Omega$$

$$-\int\left(\frac{du_\ell^*}{dr} - \frac{u_\ell^*}{r}\right) F_L \left(\frac{du_{\ell'}}{dr} - \frac{u_{\ell'}}{r}\right) dr \int Y_{\ell m}\, Y_{LM}\, Y_{\ell' m'}\, d\Omega \qquad \text{(D-18)}$$

so that the angular matrix element comes through as assumed in equation (3-36). The object called F_L here is the part of $At_{\pi N} F_\lambda$ associated with the $\vec{\nabla}\cdot\vec{\nabla}$ term. This would be the $A_2 F(r)$ in equation (3-59) or the corresponding terms in equation (3-61). The radial part of equation (D-18) is the factor evaluated by DWPI when constructing the transition matrix element.

APPENDIX E

FOLDING MODEL FORMULAE

This appendix will outline the derivation of the folding model formulae that were given in Chapter 3. In addition, it will define the conventions for electron scattering form factors.

The discussion here is for pions only, so the interaction is limited to the spin-orbit and central terms only. It is written as

$$\mathscr{V}_{pt} = g^{C}(r) + g^{LS}(r)\ i\ \vec{\sigma}\cdot\vec{L} \quad . \qquad \text{(E-1)}$$

The central part contains the kinematic factors [see equation (2-43)] for the transformation to the pion-nucleus center of mass and will eventually be expressed as a function of q in the local Laplacian model as described in Appendix B. This Laplacian form of the central interaction is never used for calculations here, but is included to indicate the way the folding formula works. The spin-orbit part is also affected by the kinematical transform but, as shown in equation (2-42) the factor of p_1^{-1} cancels the factor of p_1 from γ [equation (2-33)]. Thus, the spin-orbit comes in without any extra factors. The second term in equation (2-43), which contributes to elastic scattering, would come in with an extra factor of ε. Although a number of terms from the spin-orbit interaction can contribute to various ractions, the discussion here will be limited to those that contribute to abnormal parity transitions.

One result will be used repeatedly in these calculations. It relates the expansion of a tensor product, which usually looks like $Y_L \cdot T_L$. The expansion of the Y_L gives

$$Y_{LM}(\hat{r}) = (4\pi)^{-1/2} \sum_{L_p L_t} i^{L_p - L_t - L} \hat{L}_p \hat{L}_t \hat{L}^{-1}$$

$$\times \langle L_p 0 \; L_t 0 | L0 \rangle \left[Y_{L_p} \otimes Y_{L_t} \right]^L_M \qquad \text{(E-2)}$$

and the rearrangement of the tensor product gives

$$Y_L \cdot T_L = (4\pi)^{-1/2} \sum_{L_p L_t} \sum_J i^{L_p - L_t - L} \hat{L}_p \hat{L}_t \hat{L}^{-1}$$

$$\times \langle L_p 0 \; L_t 0 | L0 \rangle \; (-)^{L_p + L} \; W(L_p L_t \; k_1 k_2; \; LJ)$$

$$\times \left[Y_{L_p} \otimes k_1 \right]^J \cdot \left[Y_{L_t} \otimes k_2 \right]^J \qquad \text{(E-3)}$$

where k_1 and k_2 stand for the arguments out of which the tensor T_L is composed.

The central term is straightforward, since

$$g^C_o(r) = \sqrt{4\pi} \; g^C(r) \; Y_{00}(\hat{r})$$

$$= g^C(r) \sum_{L_p L_t} \sum_J i^{L_p - L_t} \hat{L}_p \hat{L}_t$$

$$\times \langle L_p 0 \; L_t 0 | 00 \rangle \; (-)^{L_p} \; W(L_p L_t \; 00; \; 0J)$$

$$\times \left[Y_{L_p} \otimes 1 \right]^J \cdot \left[Y_{L_t} \otimes 1 \right]^J \; . \qquad \text{(E-4)}$$

Evaluating this, the clebsch gives $L_p = L_t$ and the Racah gives $L_p = L_t = J$ and this all reduces to

$$g^C(r) \sum_j \left[Y_J \circledast 1 \right]^J \cdot \left[Y_J \circledast 1 \right]^J \tag{E-5}$$

The fourier transform of this gives

$$\sum_n w_n^2 \, g^C(k) \sum_J \mathscr{T}_{J0J}(p) \cdot \mathscr{T}_{J0J}(t) \tag{E-6}$$

where

$$w_n^2 = 2k^2 \, dk/\pi \ ,$$

$$g^C(k) = 4\pi \int_0^\infty j_0(kr) \, g^C(r) \, r^2 \, dr$$

and

$$\mathscr{T}_{J0J} = j_J(kr) \, Y_J(\hat{r}) \ .$$

When the expectation value over the target and projectile wave functions is taken,

$$\left\langle \mathscr{T}_{J0J}(t) \right\rangle \longrightarrow j_J(kr) \, \rho^J(k)$$

and

$$\left\langle \mathscr{T}_{J0J}(p) \right\rangle \longrightarrow T_{J0J}(p) \tag{E-7}$$

where $\rho^J(k)$ is the fourier transform of the form factor $\rho_J(r)$ defined in Chapter 3, and T_{J0J} is the operator used in the angular momentum algebra of Chapter 3.

The spin-orbit term requires rewriting

$$\vec{L} \cdot \vec{\sigma} = (\vec{r} \times \vec{p}) \cdot \vec{\sigma} = \vec{r} \cdot (\vec{p} \times \vec{\sigma}) = -i\sqrt{\frac{8\pi}{3}}\, r\, Y_1(\hat{r}) \cdot T_1(\vec{p}, \vec{\sigma}) \qquad \text{(E-8)}$$

using results from Brink and Satcher [Bri 71]. When combined with the original formula in equation (E-1), this gives

$$\begin{aligned} & rg^{LS}(r)\sqrt{\frac{8\pi}{3}}\, Y_1(\hat{r})\, T_1(\vec{p}, \vec{\sigma}) \\ & = rg^{LS}(r)\sqrt{\frac{2}{3}} \sum_{L_p L_t} \sum_{J} i^{L_p - L_t - 1}\, \hat{L}_p\, \hat{L}_t\, \hat{1}^{-1} \\ & \times \langle L_p 0\ L_t 0 | 10 \rangle\, (-)^{L_p+1}\, W(L_p L_t\ 11,\ 1J) \\ & \times \left[Y_{L_p} \otimes \vec{P} \right]^J \cdot \left[Y_{L_t} \otimes \vec{\sigma} \right]^J \quad . \end{aligned} \qquad \text{(E-9)}$$

The fourier transform of this gives

$$\begin{aligned} & \sum_n w_n^2\, g^{LS}(k) \sum_L \sum_J \sqrt{\frac{2}{3}}\, i^{J-L-1}\, \hat{J}\, \hat{L}\, \hat{1}^{-1} \\ & \times \langle J0\ L0 | 10 \rangle\, (-)^{J+1}\, W(J\ L\ 11,\ 1J) \times \mathscr{P}_{JJ}(p) \cdot \mathscr{T}_{L1J}(t) \end{aligned} \qquad \text{(E-10)}$$

where

$$g^{LS}(k) = 4\pi \int j_1(kr)\, kr\, g^{LS}(r)\, r^2\, dr \qquad \text{(E-11)}$$

and

$$\mathscr{P}_{JJ} = \frac{1}{k} [\, \mathscr{T}_J \times \vec{p}\,]^J \qquad \text{(E-12)}$$

$$\mathscr{T}_{L1J} = [\, \mathscr{T}_L \times \vec{\sigma}\,]^J$$

and

$$\mathscr{T}_L = j_L(kr)\, Y_L(\hat{r}) \quad .$$

The other terms, principally the one involving $_{J1J}$, have been omitted since they do not contribute to an abnormal parity transition. If we now evaluate the expression, we get

$$\sum_n w_n^2 \, g^{LS}(k) \sum_J \mathscr{P}_{JJ}(p) \cdot$$

$$\left[\sqrt{\frac{J+1}{2J+1}} \, \mathscr{T}_{J-1,1J} - \sqrt{\frac{J}{2J+1}} \, \mathscr{T}_{J+1,1J} \right] \cdot \tag{E-13}$$

When the expectation value is taken this becomes

$$\sum_n w_n^2 \, g^{LS}(k) \sum_J \left\langle P_{JJ} \right\rangle \cdot \rho_J^S(k) \, j_J(kr) \tag{E-14}$$

where j_J is the spherical Bessel function,

$$\rho_J^S = \sqrt{\frac{J+1}{2J+1}} \left\langle \mathscr{T}_{J-1,1J} \right\rangle - \sqrt{\frac{J}{2J+1}} \left\langle \mathscr{T}_{J+1,1J} \right\rangle \tag{E-15}$$

and

$$\left\langle \mathscr{T}_{L1J} \right\rangle = \int j_L(kr) \left\langle T_{L1J} \right\rangle r^2 \, dr$$

and where $\left\langle P_{JJ} \right\rangle$ is worked out in Chapter 3. The form factor is the "spin density" for this transition, described in Chapter 3. Because of the form of this result, it is only necessary to calculate one term in DWPI when including the spin-orbit calculation.

Finally, it is necessary to summarize the definitions used for the electron scattering results. The charge form factor is

$$\left| F \right|^2 = \frac{4\pi}{Z^2} \frac{2I'+1}{2I+1} \left| \rho_J(k) \right|^2 \tag{E-16}$$

where ρ_J is the expectation value of $\langle \mathscr{T}_{J0J} \rangle$ as defined above. The transverse electric form factor is

$$\left|F_{TE}\right|^2 = \frac{2I'+1}{2I+1}\, q^2 \left(\frac{e\hbar}{2mc}\right)^2 \left| \frac{g_S}{2}\, \rho^S_{JJ} + 2g_L\, \rho^L_J \right|^2 \qquad \text{(E-17)}$$

where g_S and g_L are the gyromagnetic ratios for spin and orbital currents; the current densities are defined in [Pet-81]. The magnetic form factor is

$$\left|F_M\right|^2 = \frac{2I'+1}{2I+1}\, q^2 \left(\frac{e\hbar}{2mc}\right)^2 \left| \frac{g_S}{2}\, \rho^S_J - 2g_L\, \rho^L_{JJ} \right|^2 \qquad \text{(E-18)}$$

where ρ^S_J is the spin density that enters pion scattering, and the orbital current is defined in [Pet 81].

The finite size of the proton is included by multiplying these each by

$$\left(1 + 0.0533\, q^2\right)^{-4}, \qquad \text{(E-19)}$$

but the center of mass correction, normally given by

$$e^{(q^2/A\,\alpha^2)} \qquad \text{(E-20)}$$

is not since the same correction is not made in the pion calculations.

BIBLIOGRAPHY

REFERENCES

[Ada 77] G. S. Adams et al., Phys. Rev. Lett. 38, 1387 (1977).

[Ama 81] J. F. Amann et al., Phys. Rev. C23, 1635 (1981).

[Aus 70] N. Austern, Direct Nuclear Reaction Theories, John Wiley (New York), 1970.

[Bak 58] W. F. Baker and J. Rainwater, Phys. Rev. 112, 1763 (1958).

[Bak 58a] W. F. Baker, H. Byfield and J. Rainwater, Phys. Rev. 112, 1773 (1958).

[Bat 78] C. J. Batty et al., Phys. Rev. Lett. 40, 931 (1978).

[Bay 75] G. Baym and G. E. Brown, Nucl. Phys. A247, 395 (1975).

[Bin 70] F. Binon et al., Nucl. Phys. B17, 168 (1970).

[Ble 79] M. Blecher et al., Phys. Rev. C20, 1884 (1979).

[Ble 81] M. Blecher, private communication, 1981.

[Bos 77] E. Boschitz, "Proceedings of the Zurich Conference on Intermediate Energy Nuclear Physics," (unpublished) 1977; and private communication.

[Bri 75] D. M. Brink and G. R. Satcher, Angular Momentum, Clarendon Press (Oxford), 1975.

[Bro 79] G. E. Brown, B. K. Jennings and V. I. Rostokin, Phys. Rep. 50C, 227 (1979).

[Byf 52] H. Byfield, J. Kessler and L. M. Lederman, Phys. Rev. 86, 17 (1952).

[Carr] J. A. Carr, MSUDWPI, modification of program DWPI [Eis 76] at Michigan State University (unpublished).

[Car 81] J. A. Carr, H. McManus and K. Stricker, preprint, 1981.

[Car 81a] J. A. Carr and F. Petrovich, program ALLWRLD (unpublished), 1981.

[Cha 79] B. R. Chabloz et al., Phys. Lett. 81B, 143 (1979); see also [Pif 77].

[Cha 79a] J. Chai and D. O. Riska, Nucl. Phys. A329, 429 (1979); and references therein.

[Che 73] B. T. Chertok, C. Sheffield, J. W. Lightbody, S. Penner and D. Blum, Phys. Rev. C8, 23 (1973).

[Chi 69] D. T. Chivers et al., Nucl. Phys. A126, 129 (1969).

[Cot 80] W. B. Cottingame and D. B. Holtkamp, Phys. Rev. Lett. 45, 1828 (1980).

[Cra 67] G. M. Crawley and G. T. Garvey, Phys. Rev. 160, 981 (1967).

[Cue 79] F. Cuerna, "LAMPF Workshop on Pion Single Charge Exchange," LA-7892-C, 177 (1979).

[DeJ 74] DeJager, DeVries and DeVries, At. Data and Nucl. Data Tables, 14, 479 (1974).

[Del 80] J. Delorme, A. Figureau and P. Guichon, Phys. Lett. 99B, 187 (1981).

[Don 70] T. W. Donnelly, Jr., J. D. Walecka, G. E. Walker and I. Sick, Phys. Lett. 32B, 545 (1970).

[Dor 79] A. Doron et al., "LAMPF Workshop on Pion Single Charge Exchange," LA-7892-C, 167 (1979).

[Dyt 77] S. A. Dytman et al., Phys. Rev. Lett. 38, 1059 (1977).

[Dyt 79] S. A. Dytman et al., Phys. Rev. C19, 971 (1979); see also [Dyt 77].

[Ede 61] R. M. Edelstein, W. F. Baker and J. Rainwater, Phys. Rev. 122, 252 (1961).

[Edw 71] G. W. Edwards and E. Rost, Phys. Rev. Lett. 26, 785 (1971).

[Eis 73] J. M. Eisenberg, J. Hufner and E. J. Moniz, Phys. Lett. 47B, 381 (1973).

[Eis 74] R. A. Eisenstein and G. A. Miller, Comput. Phys. Commun. 8, 130 (1974).

[Eis 76] R. A. Eisenstein and G. A. Miller, Comput. Phys. Commun. 11, 95 (1976).

[Eis 80] J. M. Eisenberg and D. S. Koltun, Theory of Meson Interactions with Nuclei, John Wiley (New York) 1980.

[Ell 68] J. P. Elliott, A. D. Jackson, M. A. Mavromatis, E. A. Sanderson and B. Singh, Nucl. Phys. A121, 241 (1968).

[Eri 66] M. Ericson and T. E. O. ericson, Ann. Phys. 36, 323 (1966).

[Ern 80] D. J. Ernst and G. A. Miller, Phys. Rev. C21, 1472 (1980).

[Fla 79] J. B. Flanz et al., Phys. Rev. Lett. 43, 1922 (1979).

[Fra 53] N. C. Francis and K. M. Watson, Phys. Rev. 92, 291 (1953).

[Fri 65] M. P. Fricke and G. R. Satchler, Phys. Rev. 139, B567 (1965).

[Ful 68] S. A. Fulling and G. R. Satchler, Nucl. Phys. A111, 81 (1968).

[Gel 53] M. Gell-Mann and M. L. Goldberger, Phys. Rev. 91, 398 (1953).

[Gib 76] W. R. Gibbs, B. F. Gibson, A. T. Hess, G. J. Stephenson, Jr. and W. B. Kaufman, Phys. Rev. Lett. 36, 85 (1976).

[Gil 64] V. Gillet and N. Vinh Mau, Nucl. Phys. 54, 321 (1964).

[Gla 55] R. J. Glauber, Phys. Rev. 100, 242 (1955).

[Gol 48] M. L. Goldberger, Phys. Rev. 74, 1270 (1948).

[Gol 64] M. L. Goldberger and K. M. Watson, Collision Theory, John Wiley (New York), 1964.

[Hal 81] D. Halderson et al., to be published in Phys. Rev. C24, 1981.

[Hin 73] R. A. Hinrichs, D. Larson, B. M. Preedom, W. G. Love and F. Petrovich, Phys. Rev. C7, 1981 (1973).

[Hir 79] M. Hirata, J. H. Koch, F. Lenz and E. J. Moniz, Ann. Phys. (NY) 120, 205 (1979).

[Holt] D. Holtkamp, private communication.

[Hol 80] D. B. Holtkamp et al., Phys. Rev. Lett. 45, 420 (1980).

[Huf 75] J. Hufner, Phys. Rep. 21C, 1 (1975).

[Hyd 81] C. Hyde et al., abstract DE15, Bull. Amer. Phys. Soc. 26, 27 (1981).

[Ing 78] Q. Ingram et al., Phys. Lett. 76B, 173 (1978).

[Jac 75] D. F. Jackson, Nuclear Reactions, Chapman and Hall (London), 1975.

[Joh 78] M. B. Johnson and H. A. Bethe, Comments Nucl. Part. Phys. 8, 75 (1978).

[Joh 78a] M. B. Johnson and H. A. Bethe, Phys. Lett. 78B, 560 (1978).

[Joh 79] M. Johnson, "LAMPF Workshop on Pion Single Charge Exchange," LA-7892-C, 343 (1979).

[Kal 64] A. Kallio and K. Kolltveit, Nucl. Phys. 53, 87 (1964).

[Kei 78] B. K. Keister, Phys. Rev. C18, 1934 (1978).

[Kei 81] B. K. Keister, communication quoted in [Ama 81]; see also [Kei 78].

[Ker 59] A. K. Kerman, H. McManus and R. M. Thayler, Ann. Phys. 8, 551 (1959).

[Kis 55] L. S. Kisslinger, Phys. Rev. 98, 761 (1955).

[Kis 76] L. S. Kisslinger and W. L. Wang, Ann. Phys. (NY) 99, 374 (1976).

[Kov 56] J. S. Kovacs, Phys. Rev. 101, 397 (1956).

[Kuo] T. T. S. Kuo, unpublished results, quoted in [Pet 70].

[Lan 62] A. M. Lane, Phys. Rev. Lett. 8, 171 (1962).

[Lan 73] R. H. Landau, S. C. Phatak and F. Tabakin, Ann. Phys. 78, 299 (1973).

[Lan 73a] R. H. Landau and M. McMillan, Phys. Rev. C8, 2094 (1973).

[Lan 78] R. H. Landau and A. W. Thomas, Nucl. Phys. A302, 461 (1978).

[Lee 71] H. K. Lee and H. McManus, Nucl. Phys. A167, 257 (1971).

[Lee 74] T.-S. H. Lee and F. Tabakin, Nucl. Phys. A226, 253 (1974).

[Lee 77] T.-S. H. Lee and S. Chakravarti, Phys. Rev. C16, 273 (1977).

[Lic 80] J. Lichtenstadt, C. N. Papanicolas, C. P. Sargent, H. Heisenberg and J. S. McCarthy, Phys. Rev. Lett. 44, 858 (1980).

[Lip 50] B. A. Lippmann and J. Schwinger, Phys. Rev. 79, 469 (1950).

[Liu 77] L. C. Liu and C. M. Shakin, Phys. Rev. C16, 333 (1977).

[Lov 72] W. G. Love, Nucl. Phys. A192, 49 (1972).

[Lov 81] W. G. Love, J. A. Carr, D. Halderson, F. Petrovich and H. McManus, preprint, submitted to Phys. Rev. C, 1981.

[Mac 73] R. Mach, Nucl. Phys. A205, 56 (1973).

[Mal 78] D. J. Malbrough et al., Phys. Rev. C17, 1395 (1978).

[McM 81] H. McManus and D. O. Riska, preprint, 1981.

[Mil 74] G. A. Miller, Phys. Rev. C10, 1242 (1974).

[Mil 76] G. A. Miller and J. E. Spencer, Ann. Phys. 100, 562 (1976).

[Moi 78] M. A. Moinester et al., Phys. Rev. C18, 2678 (1978).

[Mor 80] C. L. Morris, "Workshop on Nuclear Structure with Intermediate-Energy Problems," Los Alamos Report LA-8303-C, 57 (1980) unpublished; and private communication.

[Nak 80] K. Nakai et al., Phys. Rev. Lett. 44, 1446 (1980).

[Neuh] R. Neuhausen, unpublished data, quoted in [Del 81].

[Olm 79] C. Olmer et al., Phys. Rev. Lett. 43, 612 (1979).

[Olm 80] C. Olmer et al., Phys. Rev. C21, 254 (1980); see also [Zei 78].

[Ose 79] E. Oset and W. Weise, Nucl. Phys. A319, 477 (1979).

[Ose 79a] E. Oset, W. Weise and R. Brockmann, Nucl. Phys. 82B, 34 (1979); and references therein.

[Ose 79b] E. Oset and W. Weise, Nucl. Phys. A329, 365 (1979).

[Pet 70] F. Petrovich, Ph.D. Dissertation, Michigan State University, 1970.

[Pet 75] F. Petrovich, Nucl Phys. A251, 143 (1975).

[Pet 80] F. Petrovich, W. G. Love, A. Picklesimer, G. E. Walker and E. R. Siciliano, Phys. Lett. 95B, 166 (1980).

[Pet 81] F. Petrovich and W. G. Love, Nucl. Phys. A354, 499c (1981).

[Pif 77] J. Piffaretti et al., Phys. Lett. 71B, 324 (1977).

[Pre 79] B. M. Preedom et al., Nucl. Phys. A326, 385 (1979).

[Pre 81] B. M. Preedom et al., Phys. Rev. C23, 1134 (1981); see also [Mal 78] and [Moi 79].

[Ris 80] D. O. Riska and M. Sarafian, Phys. Lett. 95B, 185 (1980).

[Row 78] G. Rowe, M. Solomon and R. H. Landau, Phys. Rev. C18, 584 (1978).

[Sap 56] G. Saphir, Phys. Rev. 104, 535 (1956); see [Tra 53] for the beautiful pictures from this apparatus.

[Sat 64] G. R. Satchler, Nucl. Phys. 55, 1 (1964).

[Sch 68] L. I. Schiff, Quantum Mechanics, McGraw-Hill (New York), 1968.

[Sek 80] R. Seki, K. Masutani, M. Oka and K. Yazaki, Phys. Lett. 97B, 200 (1980).

[Seki] R. Seki, private communication.

[Sha 76] Y. Shamai et al., Phys. Rev. Lett. 36, 82 (1976).

[Spa 79] D. A. Sparrow, "LAMPF Workshop on Pion Single Charge Exchange," LA-7892-C, 53 (1979).

[Str 79] K. E. Stricker, H. McManus and J. A. Carr, Phys. Rev. C19, 929 (1979).

[Str 79a] K. E. Stricker, Ph.D. Dissertation, Michigan State University (unpublished) 1979.

[Str 80] K. Stricker, J. A. Carr and H. McManus, Phys. Rev. C22, 2043 (1980).

[Tau 74] L. Tauscher and W. Schneider, F. Physik 271, 409 (1974).

[Thi 76] M. Thies, Phys. Lett. 63B, 39 (1976).

[Thi 76a] M. Thies, Phys. Lett. 63B, 43 (1976).

[Tho 80] A. W. Thomas and R. H. Landau, Phys. Rep. 58C, 121 (1980).

[Tok 80] H. Toki and W. Weise, Phys. Lett. 92B, 265 (1980); see also references therein.

[Tra 53] J. F. Tracy, Phys. Rev. 91, 960 (1953).

[Wag 75] W. T. Wagner, G. M. Crawley, G. R. Hammerstein and H. McManus, Phys. Rev. C12, 757 (1975).

[Wat 53] K. M. Watson, Phys. Rev. 89, 575 (1953).

[Wei 78] C. A. Weidner et al., Phys. Lett. 78B, 26 (1978).

[Yen] S. Yen, private communication.

[Yen 80] S. Yen et al., Phys. Lett. 93B, 250 (1980).

[Yoo 81] K. B. Yoo and R. H. Landau, Oregon State University (preprint) 1981.

[Yuk 35] H. Yukawa, Proc. Phys. Math. Soc. Japan 17, 48 (1935).

[Zai 73] M. Zaider et al., "Proceedings of 5th International Conference on High Energy Physics and Nuclear Structure" (Uppsala), 219 (1973).

[Zei 78] B. Zeidman et al., Phys. Rev. Lett. 40, 1539 (1978).